The University of Kent

School of Biosciences

Study of interactions between novel Supramolecular Self-associating Antimicrobials (SSAs) and phospholipid bilayer Nanodiscs.

Year of Submission

2019

By:

Georgina Townshend

Thesis for MSc by Research

Supervisors: Dr Jose Ortega-Roldan

Dr Jennifer Hiscock

Declaration

No part of this thesis has been submitted in support of an application for any degree or other qualification of the University of Kent, or any other University or Institution of learning.

Georgina Townshend

August 2019

Acknowledgements

Firstly, I would like to thank both of my supervisors, Dr Jennifer Hiscock and Dr Jose Ortega-Roldan for their advice and support and they gave this study focus and direction. I also wish to thank both of their respective research groups for advice and support throughout this project.

In particular a thank you to Lisa White for the synthesis of the compounds here investigated. Thanks to Kendrick Ng for ongoing IT support, to Lorena Varela-Alvarez for support with laboratory and technical procedures.

I would also like to thank Dr Gary Thompson for help and support with NMR, and Ian Brown for support with microscopy.

Finally I would like to thank my friends and family for their support and my son Eric for his patience.

Table of Contents

Acknowledgements 2

List of Figures 6

Abstract 9

1. Introduction 10

1.1. Background 10

1.2. Bacteria cell walls 11

1.3. Phospholipids in the cytoplasmic membrane 12

1.4. Lipid Structures 15

1.5. Antimicrobials 17

1.6. Antimicrobial Resistance 18

1.7. Global action plan on antimicrobial resistance 20

1.8. Membrane mimetics 20

1.9. Advances in lipid Solubilisation Techniques 22

1.10. Synthetic Amphiphiles 23

1.11. Research on Antimicrobial activity with mimetic membranes 25

1.12. Project Aims and Objectives 26

1.13. Chemical Structures 28

2. Materials and Methods 29

2.1. General 29

2.2. Solubilisation of Poly(styrene-co-maleimide) (SMI) 29

2.3. Solubilisation of Styrene-maleic Anhydride (SMAnh) 30

2.4. SMILPs preparation 30

2.5. SMALPs preparation 30

2.6. Purification 31

2.7. RI of Nano discs 31

2.8. UV-Vis Quantification 31

2.9. DLS studies 32

2.10. Zeta Potential Studies 32

2.11. Transmission Electron Microscopy (TEM) Imaging 32

2.12. NMR ^{1}H 1D 33

2.13. NMR ^{1}H CPMG 33
2.14. NMR Titration 34
3. Results and Discussion 35
3.1. General Structure of Compounds 35
3.2. Poly(styrene-co-maleimide) (SMI_{2000I}) 36
3.3. Styrene-maleic Anhydride (SMAnh) 37
3.4. Nanodiscs 38
3.5. Purification of Nanodiscs 39
3.6. Index of refraction for Nanodiscs 41
3.7. Optimisation 41
3.7.1 DLS intensity weighted particle size distribution of SMILPs 42
3.7.2 DLS number weighted particle size distribution of SMILPs 43
3.7.3 DLS correlation function data 44
3.7.4 TEM Imaging of SMILPs 44
3.7.5 Viability of SMILPs 46
3.7.6 Conclusion 46
3.8. SMALP Results and Discussion 47
3.8.1. UV-Vis Quantification 47
3.8.2 DLS average intensity particle size distribution 48
3.8.3 DLS Number weighted particle size distribution 49
3.8.4 DLS correlation function data 51
3.8.5 Zeta potential 52
3.8.6 TEM Imaging of SMALPs 54
3.9. NMR Results and Discussion 56
3.9.1 Hydrogen preferential binding mode 56
3.9.2 NMR ^{1}H 1D DMPC and *E.coli* [SMALPs]/ [Compound 1] 57
3.9.3 NMR ^{1}H 1D DMPC and *E.coli* [SMALPs]/ [Compound 2] 61
3.9.4 NMR ^{1}H 1D DMPC and *E.coli* [SMALPs]/ [Compound 3] 64
3.9.5 NMR ^{1}H 1D *E.coli* SMALPs [SMALPs]/ [Compound (1) (2) (3)] 66
3.9.6 NMR ^{1}H 1D DMPC [SMALPs]/ [Compound (1) (2) (3)] 68
3.9.7 NMR ^{1}H CPMG DMPC and *E.coli* [SMALPs]/ [Compound 1] 69
3.9.8 NMR ^{1}H CPMG DMPC and *E- coli* [SMALPs]/ [Compound 2] 72
3.9.9 NMR ^{1}H CPMG DMPC and *E.coli* [SMALPs]/[Compound 3] 74
3.9.10 NMR ^{1}H CPMG *E.coli* SMALPs [SMALPs]/[Compound (1)(2)(3)] 77

3.9.11 NMR ^{1}H CPMG DMPC [SMALPs]/[Compound (1)(2)(3)] 78
3.9.12 Secondary binding modes 80
3.9.13 SSA structure-activity 81
4. Overall Conclusions 83
Further work 83
5. References 84
6. Appendices 88
NMR spectra for compounds 1-3 88
Table displaying concentrations used in NMR titrations 89
NMR ^{1}H 1D Data Tables 90
NMR CPMG ^{1}H Data Tables 96

List of Figures

Figure 1: Deaths attributable to AMR compared to other major causes of death.[2] 10
Figure 2: Gram-negative bacteria and gram-positive bacteria. 12
Figure 3: PE and PC phospholipid head groups.....14
Figure 4: *Molecular shapes of lipids.* 16
Figure 5: Nanodisc formation.....23
Figure 6*: General molecular structure of first generation amphiphilic molecules.* 26
Figure 7: Chemical structures, compounds **1-3** + Tetrabutylammonium.....28
Figure 8: Reaction schematic for the protonation of SMI. 36
Figure 9: Reaction schematic for the deprotonation of styrene-maleic anhydride. 37
Figure 10: Gel filtration chromatography DLS results.....40
Figure 11: Average intensity particle size distribution of E.coli SMILPs.....42
Figure 12*: Average number weighted particle size distribution of E.coli SMILPs.* 43
Figure 13*: Correlation function data for E.coli SMILPs.* 44
Figure 14*: TEM image showing results from E.coli SMILPs.* 45
Figure 15: *TEM image showing results from E.coli SMILPs.* 45
Figure 16: Calibration curve for SMA in PB. Error given is the standard error of the mean.....47
Figure 17: *Average intensity particle size distribution of E.coli SMALPs (326.6 µM).* 48
Figure 18*: Average intensity particle size distribution of DMPC SMALPs (412 µM).* 49
Figure 19*: Average number weighted particle size distribution of E.coli SMALPs (326.6 µM).* ..50
Figure 20: Average number weighted particle size distribution of DMPC SMALPs (412 µM). ...50
Figure 21: *Correlation function data relating for E.coli SMALPs (326.6 µM).* 51
Figure 22*: Correlation function data for DMPC SMALPs (412 µM),* 51
Figure 23*: Zeta potential data for E.coli SMALPs (326.6 µM).* 53
Figure 24: Zeta potential data for DMPC SMALPs (412 µM). 53
Figure 25*: TEM image of E.coli SMALPs sample. Scale bar =100 nm* 54
Figure 26: Enlarged TEM image of E.coli SMALPs sample. Scale bar =100 nm.....54
Figure 27: *TEM image of DMPC SMALPs sample. Scale bar =100 nm* 55
Figure 28: Enlarged TEM image of DMPC SMALPs sample. Scale bar =100 nm.....55
Figure 29: Hypothesised unhindered HBA and HBD preferential binding modes with SSA: PE headgroup.....57
Figure 30: Hypothesised sterically hindered electrostatic interactions and HBA and HBD preferential binding modes with SSA: PC headgroup.....57
Figure 31: ^{1}H 1D NMR results for DMPC and E.coli [SMALPs]/ [Compound **1**] 59
Figure 32: ^{1}H 1D NMR results for DMPC and E.coli [SMALPs]/ [Compound **1**] zoomed in 59
Figure 33: ^{1}H 1D NMR spectra stack plot for E.coli [SMALPs]/ [Compound **1**] 60
Figure 34: ^{1}H 1D NMR spectra stack plot for DMPC [SMALPs]/ [Compound **1**] 61
Figure 35: ^{1}H 1D NMR results for DMPC and E.coli [SMALPs]/ [Compound **2**] 62
Figure 36: ^{1}H 1D NMR results for DMPC and E.coli [SMALPs]/ [Compound **2**] zoomed in.....62

Figure 37: ^{1}H 1D NMR spectra stack plot for E.coli [SMALPs]/ [Compound **2**] 63
Figure 38: ^{1}H 1D NMR spectra stack plot for DMPC [SMALPs]/ [Compound **2**] 63
Figure 39: 1H 1D NMR results for DMPC and E.coli [SMALPs]/ [Compound **3**] 64
Figure 40: ^{1}H 1D NMR results for DMPC and E.coli [SMALPs]/ [Compound **3**] zoomed in 65
Figure 41: ^{1}H 1D NMR spectra stack plot for E.coli [SMALPs]/ [Compound **3**] 65
Figure 42: ^{1}H 1D NMR spectra stack plot for DMPC [SMALPs]/ [Compound **3**] 66
Figure 43: *^{1}H 1D NMR results for E.coli [SMALPs]/ [Compound (**1**) (**2**) (**3**)]*.....67
Figure 44: ^{1}H 1D NMR results for E.coli [SMALPs]/ [Compound (**1**) (**2**) (**3**)] zoomed in.....67
Figure 45*:^{1}H 1D NMR results for DMPC [SMALPs]/ [Compound (**1**) (**2**) (**3**)]*.....68
Figure 46*: ^{1}H 1D NMR results for DMPC [SMALPs]/ [Compound (**1**) (**2**) (**3**)] zoomed in*.....69
Figure 47: ^{1}H CPMG NMR results for DMPC and E.coli [SMALPs]/ [Compound **1**].....70
Figure 48: ^{1}H CPMG NMR results for DMPC and E.coli [SMALPs]/ [Compound **1**] Zoomed in.71
Figure 49: CPMG NMR spectra stack plot for E.coli [SMALPs]/ [Compound **1**] 71
Figure 50: CPMG NMR spectra stack plot for DPMC [SMALPs]/ [Compound **1**].....72
Figure 51: ^{1}H CPMG NMR results for DMPC and E.coli [SMALPs]/[Compound **2**].....73
Figure 52: CPMG NMR spectra stack plot for E.coli [SMALPs]/ [Compound **2**].....74
Figure 53: CPMG NMR spectra stack plot for DPMC [SMALPs]/ [Compound **2**].....74
Figure 54: ^{1}H CPMG NMR results for DMPC and E.coli [SMALPs]/[Compound **3**].....75
Figure 55: ^{1}H CPMG NMR results for DMPC and E.coli [SMALPs]/[Compound **3**] Zoomed in .75
Figure 56: CPMG NMR spectra stack plot for E.coli [SMALPs]/ [Compound **3**].....76
Figure 57: CPMG NMR spectra stack plot for DPMC [SMALPs]/ [Compound **3**].....76
Figure 58: *^{1}H CPMG NMR results for E.coli [SMALPs]/[Compound (**1**)(**2**)(**3**)]* 78
Figure 59: ^{1}H CPMG NMR results for E.coli [SMALPs]/[Compound (**1**)(**2**)(**3**)]Zoomed in 78
Figure 60: *^{1}H CPMG NMR results for DMPC [SMALPs]/[Compound (**1**)(**2**)(**3**)]*.....79
Figure 61: ^{1}H CPMG NMR results for DMPC [SMALPs]/[Compound (**1**)(**2**)(**3**)] zoomed in.....80

Abbreviations

CL	Cardiolipin
CPMG NMR	Carr-Purcell-Meiboom-Gill NMR
DHFR	Dihydrofolate reductase
DLS	Dynamic light scattering
DMPC	Dimyristoyl-sn-glycero-3-phosphocholine
E. coli	Escherichia coli
HBA	Hydrogen bond acceptor
HBD	Hydrogen bond donor
MSP	Membrane scaffold protein
MWCO	Molecular weight cut-off
NMR	Nuclear Magnetic Resonance
1D NMR	One-dimensional NMR
PB	Phosphate buffer
PC	Phosphatidylcholine
PE	Phosphatidylethanolamine
RT	Room temperature
SEC	Size exclusion chromatography
SMA	Styrene-maleic Acid
SMALP	Styrene maleic acid lipid particles
SMI	Poly(styrene-co-maleimide)
SMILP	Styrene-co-maleimide lipid particles
T_2	Spin-Spin (transverse) relaxation time of nucleus
TBA	Tetrabutylammonium
UV-Vis	Ultraviolet–visible

Abstract

Novel research in antimicrobials is desperately needed due to high levels of antimicrobial resistance. It has been predicted that by 2050 antimicrobial resistant bacteria will be the cause of more deaths globally per year than cancer.[2] Herein, is the study of novel supramolecular self-associating amphiphilic compounds and their selectivity towards bacterial membranes. Here model membranes are formed mimicking bacterial cells and mammalian cells for comparison. The model membranes are termed nanodiscs and consist of lipid bilayers solubilised with a co-polymer. Nanodiscs provide an excellent mimetic system for the investigation in binding association studies through nuclear magnetic resonance (NMR). This investigation determines how different constituents attached to the same molecules affect their hydrogen bond donating (HBD) and hydrogen bond accepting (HBA) functionalities, through NMR analysis. The HBD/HBA causes membrane disruption and therefore shows potential for their use as future antimicrobial agents.

1. Introduction

1.1. Background

Novel research to discover new antibiotics has become increasingly important in recent years due to antimicrobial resistance rising to dangerously high levels. Increasingly, governments around the world are now seeing the lack of new antibiotics as a major health issue, which is so serious that it threatens modern medicine. A post-antibiotic era, in which common infections and minor injuries can become deadly is a very real possibility for the 21st century.[1] In 2014 the UK conducted a government review (See Figure 1) and predicted that by 2050 the amount of global deaths caused by antimicrobial resistant bacteria, could rise to 10 million, this will far exceed those attributed to cancer. [1]

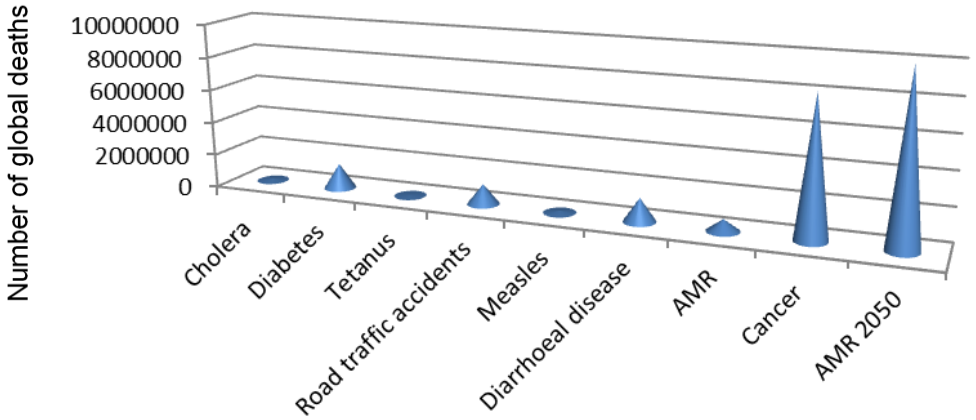

***Figure 1**: Deaths attributable to AMR compared to other major causes of death.*[2]

Sir Alexander Fleming, in 1945, discovered penicillin and shared his vision as a cautionary tale when awarded his Nobel Prize. [3] He warned against its misuse stating "it is not difficult to make microbes resistant to penicillin in the laboratory by exposing them to concentrations not sufficient to kill them." [4] In his account Fleming was referring to under dosing, which forms part the antimicrobial resistance we have today.

1.2. Bacteria cell walls

Bacteria are prokaryotic living organism that can spread quickly and reproduce, to ensure its survival. They can be classified as two major groups, as developed by Christian Gram (1884) gram-positive and gram-negative bacteria.[5] This classification is derived from gram staining, whereby the bacterium maintains the colour of a crystal violet stain then it's gram-positive. Whether or not the bacteria can retain the stain is based on the differences between the chemical and physical properties of their cell walls. Gram-positive bacteria have a thicker relatively impermeable wall, composed of peptidoglycan, which retains the crystal violet on the surface of the cells. Gram-negative has a thinner peptidoglycan wall, with an overlying lipid-protein bilayer outer membrane, this doesn't retain the violet stain will decolorize and stain red. This distinguishes between gram-positive and gram-negative groups by colouring these cells red or violet.[6]

The cell walls are known as the cell envelope. The cell envelope is a complex multilayer structure that allows selective passage of nutrients from the outside, and waste products from the inside, it helps them to survive and protects the bacteria from the environment that surrounds them.[7] Bacterial cell walls are much more complex than just the lipid membrane; a large portion of the gram-positive wall is comprised a thick layer of peptidoglycan with embedded teichoic acid. Gram-negative bacteria cell walls are structurally more complex, they contain a thin layer of peptidoglycan inner membrane, and an outer cytoplasmic membrane containing lipopolysaccharide [8] (Figure 2). This is an essential toxin that protects the cell from the hosts immune system and enable them to cross mucosal barriers, spread, and replicate in distant organs.[9]

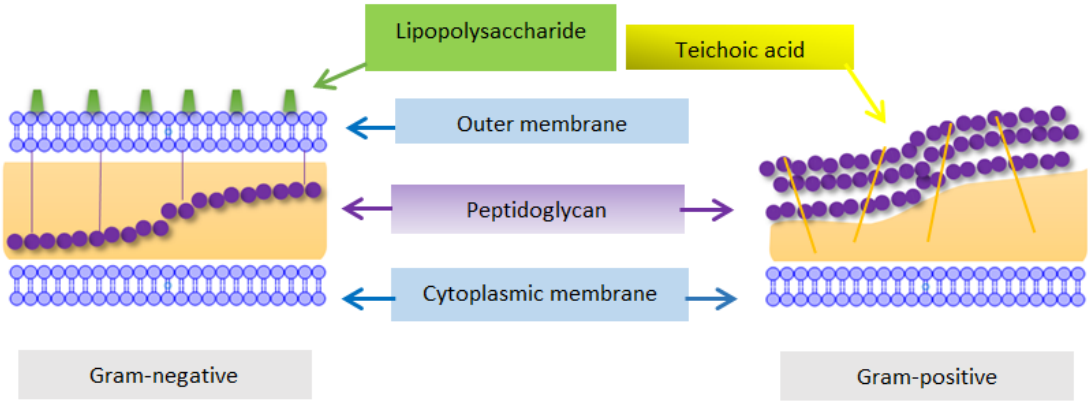

Figure 2: *Gram-negative bacteria and gram-positive bacteria.*

Bacteria can develop defence systems to resist the effects of the antimicrobials, for example they can undergo modifications where they produce enzymes that can inactivate the antimicrobial such as β-lactamase. This enzyme inactivates some penicillin, rendering them harmless to bacteria. Another common defence system is the acquirement of additional efflux pumps that can remove the toxins of the antimicrobials from within the cell, more rapidly than it can enter. These multidrug resistance efflux pumps have been observed with *Staphylococcus aureus* and among other bacterium. [10]

1.3. Phospholipids in the cytoplasmic membrane

Biological membranes form cells that are continuous structures, separating the aqueous phases between the inside and outside of the organism. They also enable living organisms to produce energy and are relatively impermeable, which enables them to be selective towards the substances that enter and leave the cell. They can regulate the communication between cells by sending, receiving and processing information in the form of chemical and electrical signals.[11]

The three major classes of membrane lipids in the cell membrane are phospholipids, glycolipids, and cholesterol. Eukaryotic membranes contain large amounts of cholesterol.[12] Phospholipids are the most dominant lipid in the cell membrane; they are amphiphilic molecules with hydrophobic tails (”water-fearing”) and hydrophilic head groups (”water-loving”) which tends to associate with water. These head groups can be charged or neutral. When in an aqueous environment the amphiphilic characteristic of the phospholipids, drives the assembly of these lipids into bilayers, where the hydrophobic tail of the lipids in each layer is directed inward, and the hydrophilic head groups are exposed to the aqueous environment, these bilayers form the cells wall barrier.[13 14]

The structure of phospholipid head group, determines how they are classified. An example of this head group classification is glycerophospholipids, their general structure consists of a glycerol phosphate backbone that is ester-linked to two fatty acyl chains at the sn-1 and sn-2 positions and a polar head group at the sn-3 position, via a phosphodiester bond.[15] There is an exception to this rule, with mitochondrial lipid cardiolipin (CL), as it contains 4 acyl chains.[16]

The most abundant phospholipid in eukaryotic cells is PC, which makes up 40 to 50% of the total cellular phospholipids, the next most abundant phospholipid in is PE, which make up ~ 40% of total phospholipids.[17] The PE phospholipids are located on the inner leaflet of the membrane.[18] PC and PE are both structurally related, as they both have a phosphate group in their headgroup, (Figure 3). These are classified as zwitterionic having a positive charge on the amine and negative charge on the phosphate.[19,20]

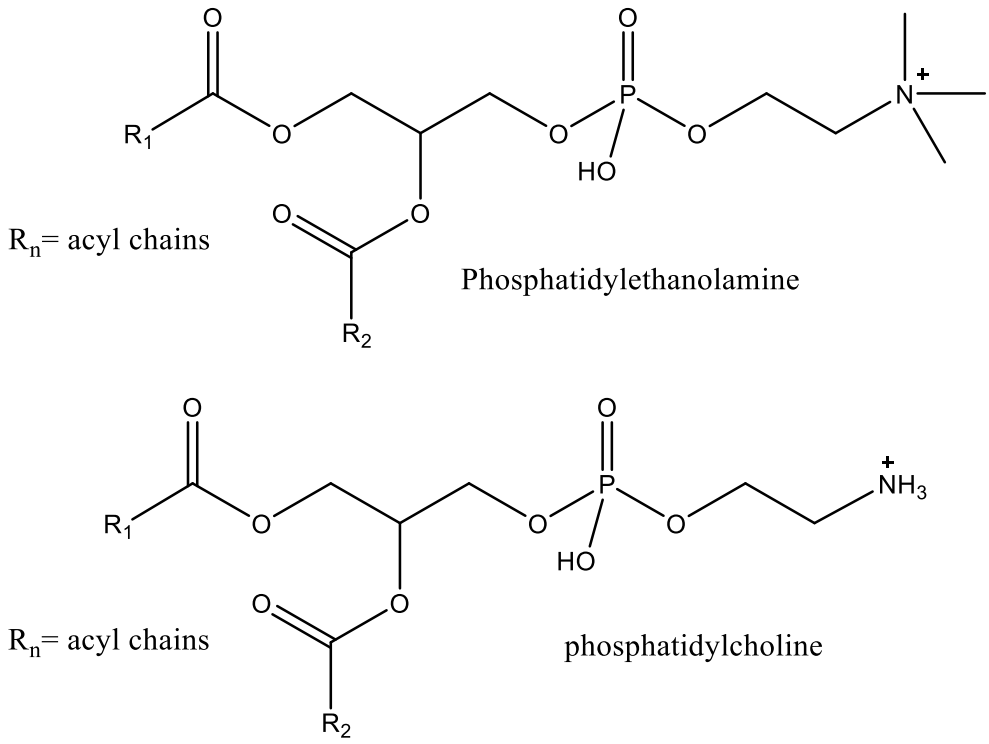

Figure 3: *PE and PC phospholipid head groups*

In bacteria the most abundant zwitterionic phospholipid present is PE. In general Gram-negative bacteria have a higher content of PE than Gram-positive bacteria. All bacteria also have at least 15% of anionic lipids, which is independent to whether they are gram-positive or gram-negative. The most abundant anionic lipids in bacteria are phosphatidylglycerol (PG) and cardiolipin (CL). These anionic lipids are targeted by cationic antimicrobial agents, which are selective towards bacteria cells, but not against mammalian cells.[21] [19]

Although structurally related the PC head group is larger than the PE headgroup, due to the three methyl groups attached to the amine in PC. This causes sterically hindered electrostatic interactions, which interferes with the PC headgroup forming hydrogen bonds. This affects the hydration level of PC which is higher than that of PE and causes weaker lipid to lipid interactions in PC.[19]

1.4. Lipid Structures

Due to the amphiphilic nature of lipids they assemble in to different structures when dispersed in an aqueous environment. The self-assembly occurs due to the hydrophilic head groups, which have a preference to interact with water and the hydrophobic tails repel water forming a bilayer. Different shaped structures can form which is dependent on the shape and the concentration of lipids in solution.[22]

Lipids have polymorphic capabilities; they are able to exist as different shapes. Their ability to adopt different structures is due to their geometry.[23,24] For example micelles, (Figure 4) are formed where the headgroup of the lipid is larger than the hydrophobic tail, giving an overall inverted conical shape.[19] Many molecules such as detergents will form spherical structures, with the head groups surrounded by water and the hydrophobic tails sequestered in the interior. [22]

The inverse micelle has the opposite formation, and occurs when the tails are bulky and the headgroup is relatively small, giving an overall conical shape[19](Figure 4), this leads to aggregated structures with a negative curvature, such as the inverted hexagonal phase (HII).

Another common structure is the lipid bilayer, where the lipids contain a large head group with two hydrophobic tails, such as PC and PE lipids.[19] In aqueous solutions they adopt a bilayer structure,(Figure 4) by arranging in a parallel orientation, with the hydrophobic interactions as the main driving force to form bilayer sheets.[22]

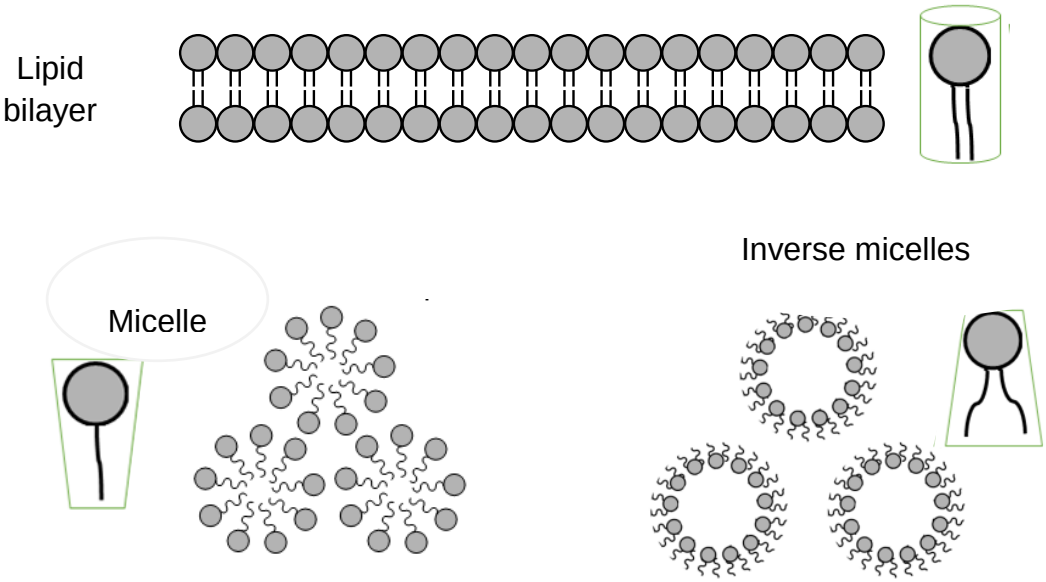

Figure 4: *Molecular shapes of lipids.*

The lipid structures can assemble in different forms, by changing the conditions of the solution, such as the electrolyte concentration, the pH, or temperature. For lipid structures to assemble the lipids must first pass from the ordered gel phase, the phase transition temperature needed to induce this change in the lipids physical state, for each one is different. In the gel phase the hydrocarbon chains are fully extended and closely packed, and in the liquid-crystal phase, the hydrocarbon chains are randomly oriented and fluid.[25] This provides the lipids enough mobility to align correctly and form structures such as micelle or a lipid bilayer. [19,22]

The phase transition temperature can be affected by many factors including the hydrocarbon chain length and headgroup species, charge and decrease in the order of desaturated to mono-unsaturated to di-unsaturated lipids.[22] Generally transition temperature values increase with the increasing acyl chain. This is due to an increase in van der Waals interactions, which in turn requires more energy to disrupt the ordered packing. On the other hand, introducing a cis double bond into the acyl chain produces a bend in the chain, which requires much lower temperatures to induce an ordered packing arrangement. The difference in transition temperatures due to headgroup

species can be seen with PE and PC lipids. These both have similar acyl chain lengths, but with the smaller PE headgroup the acyl chains are more tightly packed. This gives rise to the transition temperature of PE to be around 20 °C higher than that of PC. [22,19]

1.5. Antimicrobials

The term “antimicrobial” is used to describe substances that have the ability to reduce the presence of micro-organisms such as bacteria, fungi, helminths, protozoa and viruses. They can be disinfectants, anti-viral, antifungal, antiseptics, and antibiotics.[26] Antibiotics can be derived from living organisms or can be made synthetically. They have the ability to be bactericidal agents that kill the microbes or bacteriostatic agents, which slow down or stall bacterial growth.[26]

Antimicrobials have different modes of action which can either inhibit cell growth or initiate cell death. Unlike eukaryotic cells bacteria have structural cell wall containing peptidoglycan. Penicillin inhibits the bacteria from forming an intact peptidoglycan cell wall.[26] This results in a very delicate cell wall that does not support the growth of the cell causing it to burst, killing the bacteria.

Some antimicrobials also selectively eradicate bacteria by affecting their metabolic pathways, inhibiting cellular function. The folate metabolic pathway leads to synthesis of required precursors for cellular function and are both present in prokaryotes and eukaryotes. This pathway has dihydrofolate reductase (DHFR) which is a critical enzyme, where micro-organisms folates must be synthesised this is vital for the cells to metabolise amino acids and are required for cell division. [27] Another anti-folate target is dihyropteroate synthase (DHPS), which is an enzyme absent in eukaryotes. The enzyme DHFR is targeted by trimethoprim for antibacterial uses, which contains Sulphonamides, such as sulfamethoxazole, this prevents the bacteria from using para-

aminobenzoic acid for folate biosynthesis.[28] Once the enzyme is inhibited the bacteria can no longer grow.[27]

Another mechanism of action is the inhibition of protein synthesis leading to impaired growth. An example of this is the antibiotic is tetracycline that inhibits bacterial growth by stopping protein synthesis. Both prokaryotic and eukaryotic cells carry out protein synthesis on ribosome structures. But prokaryotic cells have an active uptake mechanism that is not found in eukaryotic cells, and this is exploited. Tetracycline can bind in high concentrations to a single site on the 30S ribosomal subunit of bacterial ribosomes, this inhibits the binding of aminoacyl-tRNAs stopping protein synthesis. [26,]

Fluoroquinolones such as ciprofloxacin can specifically target and block the ligase domain of DNA gyrase (topoisomerase II) in bacteria. These enzymes can relax tightly wound chromosomal DNA, which are essential for the replication and repair of the DNA. With the inhibition of this enzyme the bacteria is killed, and the human host isn't affected. Ciprofloxacin is bactericidal towards some gram-positive and most gram-negative bacteria.[26]

1.6. Antimicrobial Resistance

While antibiotic use is rising, the pace at which we are discovering novel antibiotics has slowed drastically.[2] Research in new antibiotics has diminished over the past decades due to the lack of return on the pharmaceutical companies' investment.[29] This is due to their short term use and they often become unusable due to the microbes becoming resistant to the new drugs. The amount of approved antimicrobials has also declined, due to unacceptable side effects and difficulty demonstrating they are not inferior to existing drugs already available.[30]

Antimicrobial resistance is now one of the biggest threats to global health, food security, and development. Microbes can develop a resistance mechanism in various

ways, one mechanism is through selective pressure, this occurs naturally when the bacteria grows, it can develop mutations in its DNA that result in resistance to certain types of drugs. Microbes present without the resistance mechanism will be inhibited or will die, and the ones that carry resistant genes can survive and multiply by dividing over time, which can be hours or just a few minutes, giving a resistant strain.[31]

The misuse of antibiotics through societal pressures has unintentionally helped drive this evolution forward with the widespread use, which are sometimes unnecessary. An example of this is when a healthcare provider has prescribed an antibiotic, due to a demanding patient, prior to a diagnosis. Also broad-spectrum antibiotics are prescribed to patients instead of a specific antibiotic due to incomplete information to diagnose an infection. The increased use of antibiotics in hospitals on critically ill patients can create an environment where antimicrobial resistant microbes can spread easily. A growing number of infections, such as pneumonia and tuberculosis are becoming harder to treat as the antibiotics used to treat them become less effective. Antibiotics are also misused agriculturally, where antibiotics are added to agricultural feed, as a precaution to maintain healthy animals, this promotes drug resistance, which can escalate the speed at which bacteria can evolve into superbugs.[31]

The organisms posing the most danger are known as “ESKAPE pathogens” which include, *Enterococcus faecium, Staphylococcus aureus, Klebsiella pneumoniae, Acinetobacter baumanii, Pseudomonas aeruginosa*, and *Enterobacter species*, these are both Gram-positive and Gram-negative species and have the ability to evade the effect of antimicrobial drugs.[32]

1.7. Global action plan on antimicrobial resistance

In 2015 The World Health Organization created a five objective global action plan to address antimicrobial resistance, which outlines five objectives: [33] The objectives focus on developing new antimicrobial drugs and slowing down microbe evolution by decreasing the misuse and overuse of the antimicrobial drugs.

The five objectives

1. Improve awareness and understanding of antimicrobial resistance through effective communication education and training.

2. Strengthen the knowledge and evidence base through surveillance and research

3. Reduce the incidence of infection through effective sanitation, hygiene and infection prevention measures.

4. Optimize the use of antimicrobial medicines in human and animal health.

5. Develop the economic case for sustainable investment that takes account of the needs of all countries and to increase investment in new medicines, diagnostic tools, vaccines and other interventions antimicrobial resistance and to coordinate numerous international sectors.

1.8. Membrane mimetics

The natural membrane is a complex environment and this has led to an interest and need for model membranes for the study and development of the membrane.[34] The physicochemical properties of the model lipid membranes can be controlled, leading to different forms of lipid structures.[35] Currently the most utilised models for cell membranes are liposomes, detergent stabilized micelles, bicelle aggregates and disc shaped supported lipid bilayers.[36]

Liposomes are small artificial spherical vesicles, consisting of one or more lipid bilayers. These can be used for the study of cell interactions and drug delivery. Liposomes have different classifications based on size and number of bilayers. Unilamellar liposomes are made up of a single phospholipid bilayer sphere. These can be further classified into two categories: large unilamellar vesicles (LUV) and small unilamellar vesicles (SUV). The multilamellar liposomes have two or more bilayer membranes, and have an onion type structure. With many unilamellar vesicles of varying sizes within one another, this leads to the multilamellar structure.[37] These are restricted by use of NMR; however micelles and nanodiscs are not.

Nanodiscs are self-assembled soluble particles that range from ~10 to 50 nm in diameter. [38] They are a useful membrane mimetic system, which consists of a non-covalent bilayer assembly of phospholipids, wrapped by either a membrane scaffold protein (MSP)[39] or a copolymer in a belt-like configuration. The MSP is only useful when studying proteins; the polymer however self-inserts into membranes and extracts membrane patches in the form of a nanodisc [40] (Figure 5). An advantage of polymer belted nanodiscs is their modularity where different compositions of phospholipids can be incorporated, and these soluble discs can then be studied.[38] Nanodiscs are often used in NMR spectroscopy in ligand-binding research. This is an important technique used within the drug discovery process for the analysis of synthetic compounds and for its ability to identify small ligands that bind to a specific target, such as nanodiscs. Information about the exact ligand binding mode is needed to improve the design of the ligand for its intended purpose.[41]

In 2007 Sligar et al [42] developed the new technology termed nanodiscs. Since then the first report of a nanodisc library was recognised from E.coli membrane proteins in 2013 by Marty et al, Where membrane proteins were extracted and incorporated into nanodiscs with different loading ratios,[43] thus optimising the MSP to lipid ratios, and they quantified how efficient the integration was by SDS-PAGE gels.[42]

1.9. Advances in lipid Solubilisation Techniques

Due to difficulties associated with structural and functional studies of the complex structure of the lipid bilayer, various solubilisation techniques have been developed. These techniques consist of a solubilising agent that satisfies the hydrophobic nature of the transmembrane segments.

The first and most common method used for membrane protein solubilisation is the use of detergents; these have been successful in extracting the proteins from their native lipid environment, and they replace the lipids with detergent molecules. Compatible detergents have been developed for specific membrane proteins, including non-ionic, sulfonated and zwitterionic.[44] Detergents as solubilising agents have their limitations; they tend to be denaturing which can lead to a loss in activity. This denaturing effect is partially improved with amphipols, which are a class of surfactants, containing amphiphilic polymers,[45] designed to keep membrane proteins soluble in water without the need for detergents, but they still denature sensitive proteins. With the side effects of the amphipols and detergents, other alternative strategies for solubilisation have been developed to better mimic the cellular membrane.[46]

In the past few years, the styrene maleic acid (SMA) copolymer has gained attention as a detergent-free approach for membrane solubilisation. [47] The amphipathic polymer solubilizes intact membrane patches in the form of nanodiscs; these particles are referred to as styrene maleic acid lipid particles (SMALPs). [46] The solubilisation of the bilayer membrane occurs in three stages. Initially the SMA will bind to the surface of the membrane. Next the polymer molecules insert into the hydrophobic core of the membrane, driven by the hydrophobic effect. Finally, the membrane is solubilized and nanodiscs are formed.[47] (Figure 5) The planar lipid bilayers discs formed are suitable for experimental studies such as NMR and are an excellent alternative to detergent solubilization.[48]

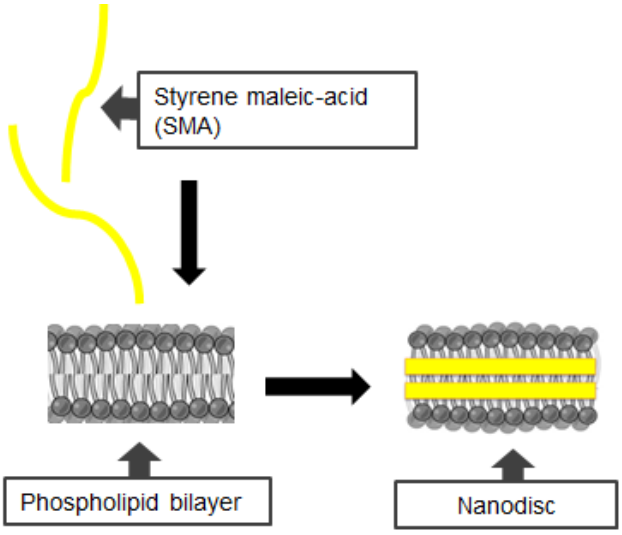

Figure 5: Nanodisc formation

The SMA polymer has many advantages it extracts the lipids in a water-soluble form, reducing disruption to the patch of membrane around them, thus keeping them stable as a SMALP complex. [47]

SMALPs can be constructed in different sizes which depend on the molar ratio of styrene to maleic acid, the general size of the 2:1 ratio SMALP is around ~10 nm.[49] SMA also has its drawbacks as it is pH sensitive, in acidic conditions below a pH of 6.5, [50] it will precipitate and in the presence of divalent cations, which are required for many applications.[51] More recently poly (styrene-co-maleimide) (SMI), a modification of SMA has been successful in overcoming these limitations. SMI forms similar nanodiscs in the size range 6 to 12 nm, with comparable efficiency to SMA, and isn't affected by acidic pH or high concentrations of divalent cations.[51]

1.10. Synthetic Amphiphiles

Amphiphilic is a term used to describe a chemical compound that possesses both hydrophilic and hydrophobic region linked by covalent bonds. The hydrophobic regions facilitate insertion of molecules into the hydrophobic regions of bacterial lipid membranes, which induces membrane disruption.[52]

Detergents are amphiphilic molecules, and can insert their hydrophobic tails into the lipid membrane, causing disruption as the concentration of detergent increases.[50] These molecules transform into detergent–lipid–protein mixed micelles which extract the membrane-embedded proteins.[53] this is one of the most widely used agents for membrane protein extraction and stabilisation in experimental studies.

Research with synthetic amphiphilic compounds, has shown that they can self-associate in to larger structures, where they form well-defined structures in aqueous solutions. The self-assembly of these molecules is the same as phospholipids with the formation of non-covalent bond interactions, these include, but not limited to electrostatics, π−π stacking, charge transfer, and hydrogen bond formations.[14] The construction of various monomeric units, was explored with different constituents, and revealed that these interactions dictated the global solution and solid state properties of the formed structures.[54,55]

Research into amphiphilic compounds as medicines, has been of increasing interest in the recent search for novel antimicrobials. A recent study of supra molecular self-associating amphiphilic compounds was investigated and demonstrated how the molecules self-assemble at the molecular level, this permitted the design and formation of over 65 self-associating compounds, which contain hydrogen bond donating (HBD) and accepting (HBA) functionalities in the structure.

The self-associative and physicochemical properties for over 30 of these self-associating amphiphilic compounds was investigated for structure–activity relationships in the solid, solution and gas phases as well as antibacterial activity. Here they found that the formation of self-associated structures is imperative for delivery of the compound to the bacterial cell, resulting in membrane disruption. [56] These compounds have a general structure with a hydrogen bond donor group and an acceptor group that can self-associate through one or more hydrogen bonds and usually the integration of an aromatic moiety. The hydrogen bond donor group is usually urea or thiourea, and

the hydrogen bond acceptor group is usually a sulfonate or phosphate moiety, however there are many other constituents that have been investigated, with the number of possible structures continuously growing.[56,54] These structure—activity studies from the general structure has shown to increase the antibacterial efficacy and have shown antibacterial activity towards methicillin-resistant *Staphylococcus aureus,* which is one of the "ESKAPE" pathogens.[56]

1.11. Research on Antimicrobial activity with mimetic membranes

A recent study investigated the associations between designer antimicrobial peptides with the phospholipid bilayer. The insertion of the cationic peptides in to the membrane altered the organisation and fluidity of the membrane. This created fluid areas in the packing of the phospholipids, which led to the delocalization of membrane bound proteins, contributing to the cells destruction. This study was conducted on model membrane system of *Bacillus subtilis,* with variations in the phospholipid composition. This better explained the implications of using model membranes in experimental studies, as these have defined properties, unlike biological membranes, which is often disputed. The results indicated that changing the lipid compositions of the bacterial membrane didn't affect susceptibility to the peptides.[57]

In another study by U. Divakara et al [58] in 2016, it was reported that maleic anhydride based novel cationic polymers, joined with amide side chains showed antibacterial efficacy against many "ESKAPE" pathogens. These polymers interact with the bacterial cell membranes by causing membrane depolarization, permeabilization and energy depletion. This was achieved by modifying the side amide chains which optimised the hydrophobicity of the amphiphilic polymers; this played an important role in selective toxicity to bacteria avoiding the mammalian cells.[58]

1.12. Project Aims and Objectives

The aim of this project is to study synthetic compound-membrane interactions, aiding research in the fight against antimicrobial resistance.

The synthetic compounds used in this study, are novel Supramolecular Self-associating Antimicrobials SSAs, these form part of a novel family of amphiphilic molecules. The three compounds selected each have unique substituents attached to the general structure shown in Figure 6. With R= Chemical substituents, A= anionic group, Y= cationic group, X= Oxygen/Sulfonate. It has been hypothesised that these create antimicrobial selectivity towards the phospholipid bilayers.

General structure:

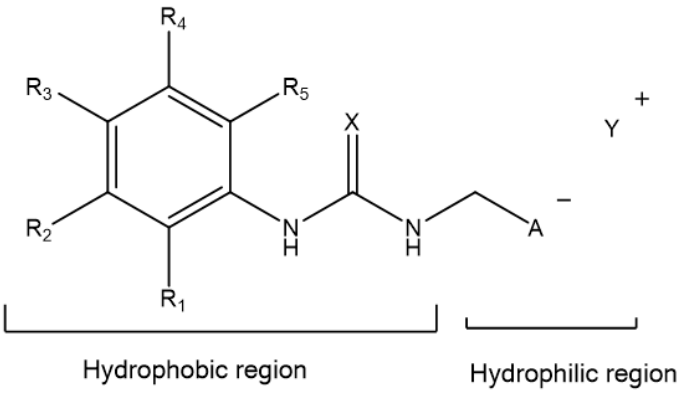

***Figure 6**: General molecular structure of first generation amphiphilic molecules.*

It has been confirmed in previous studies that the SSA monomers will self-associate through hydrogen bonding. This is significant to the antimicrobial activity of these molecules. Models for the complex include but not limited to; dimer formation through the creation of four urea-anion hydrogen bonds and polymerization[55,54] as illustrated in Figure 7. The complexes formed increase in size, with the increase in concentration of the SSA. In this study experiments were not preformed to confirm how the concentration affects the structure; however this has been confirmed with previous studies conducted by L.White et al. [61] The accuracy of these predicted models form part of ongoing studies at the University of Kent.

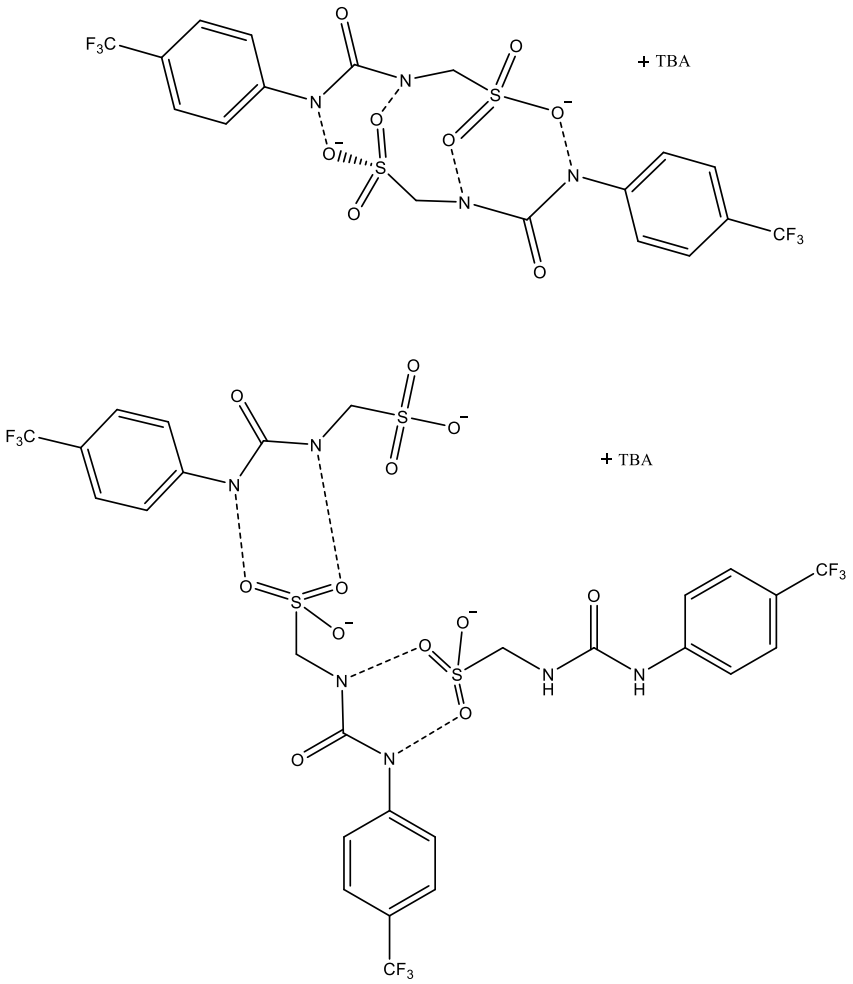

Figure 7: *SSA schematic illustrating self-association hydrogen bonding motif.*

My aim was to determine which compounds display a stronger binding affinity towards different types of phospholipid membranes, comparing those of bacterial and eukaryotic cells. The phospholipid bilayers were belted together with an appropriate synthetic polymer, which formed disc shaped planar bilayers (nanodiscs). These nanodiscs required a lipid composition comparable to bacterium cells and a second type of nanodisc comparable to mammalian cells. The resulting nanodiscs were characterised, purified and quantified to enable accurate results. The SSAs were hypothesised to interact with lipids primarily through the formation of hydrogen bonds and electrostatic interactions; these were investigated with NMR ^{1}H analysis.

1.13. Chemical Structures

The SSAs used within this study include:

1

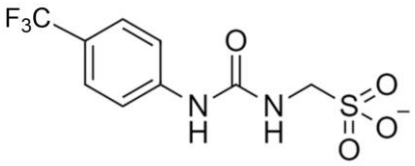

MW 539.478 g/mol

2

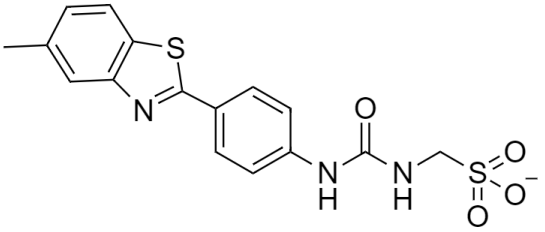

MW 618.896 g/mol

3

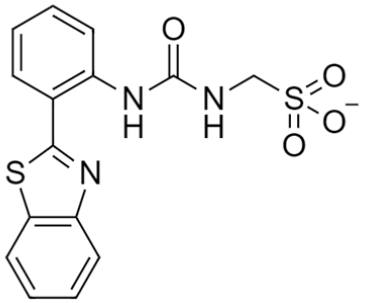

MW 604.87 g/mol

Figure 7: Chemical structures, compounds **1-3** + Tetrabutylammonium

These structures have been chosen, as they all contain the same HBA/HBD functionalities; including, urea moiety and sulfonate.

2. Materials and Methods

2.1. General

Compounds **1**-**3** were obtained from L. White, a PHD student within the J.Hiscock Laboratory. Compound **1** MW 539.478 g/mol, compound **2** MW 618.896 g/mol and compound **3** MW 604.87 g/mol. SMI_{2000I} resin, MW of 7500 and SMA_{2000} (poly(styrene-co-maleic anhydride) SMAnh), MW of 7500, sourced from Cray Valley. *E.coli* Total lipids purchased from Avanti Polar stored at -80 ^{o}C. 14:0 PC (DMPC) 1,2-dimyristoyl-sn-glycero-3-phosphocholine, MW 677.933 purchased from Avanti Polar Lipids, stored at -20 ^{o}C. Phosphate buffer NaCl 20 mM Na_2PO_4, 20 mM pH 7.0 and Phosphate buffer NaCl 20 mM Na_2PO_4 20 mM pH 7.4, was filtered and degassed prior to use. All solvents and starting materials were purchased from commercial sources or chemical stores where available and used as purchased unless stated otherwise.

2.2. Solubilisation of Poly(styrene-co-maleimide) (SMI)

SMI_{2000I} polymer was hydrolysed under reflux conditions. SMI resin (25 g) was initially ground in a pestle until a fine powder was obtained. The resulting powder suspended in HCl (250 mL, 1 M) with anti- bumping granules (0.1 g) and slowly heated to reflux (100 °C) with constant stirring. Solution refluxed for ~4 hours, until all of the solid SMI dissolved, giving a pale yellow colour. Once the solution cooled (20 ^{o}C) The SMI was precipitated by increasing pH to 8 with the addition of NaOH (5 M), and checked using pH paper. The precipitated polymer was centrifuged at 11,000 *g* for 15 minutes (4 ^{o}C), the supernatant was removed and the precipitate was washed 3 times with Milli Q water (250 mL). The polymer was suspended in HCl (0.6 M) and adjusted to pH 7.4, and left in an incubator overnight to dissolve, once completely solubilised the polymer was lyophilized and stored at room temperature.

2.3. Solubilisation of Styrene-maleic Anhydride (SMAnh)

SMA_{2000} polymer was hydrolysed under reflux conditions. SMA anhydride powder (25 g) was suspended in NaOH (250 mL, 1 M) with anti- bumping granules (0.1 g) and slowly heated to reflux (100 °C) with constant stirring. Solution refluxed for ~4 hours, until all of the solid SMA dissolved. Once the solution cooled (20 ^{o}C) The SMA was precipitated by reducing the pH to below 5 with the addition of concentrated HCl. and checked using pH paper. The precipitated polymer was centrifuged at 11,000 *g* for 15 minutes (4 ^{o}C), the supernatant was removed and the precipitate was washed 3 times with Milli Q water (250 mL). The polymer was suspended in NaOH (0.6 M) and adjusted to pH 7.4, and left in incubator overnight to dissolve, once completely solubilised the polymer was lyophilized and stored at room temperature.

2.4. SMILPs preparation

E.coli Total lipid extract (10 mg) was dissolved in methanol and chloroform (1:1 ratio) and evaporated under a stream of Nitrogen gas, to a thin lipid film. The resulting lipid film was dried for a further 1 hour under nitrogen gas. Next the lipid film was hydrated with phosphate buffer (pH 7) (1 mL) sonicated and vortexed vigorously. SMI (50 mg) was added to the opaque lipid solution and incubated for 1 h at 37 °C, giving a translucent solution.

2.5. SMALPs preparation

E.coli Total lipid extract (10 mg) was dissolved in methanol and chloroform (1:1 ratio) and evaporated under a stream of Nitrogen gas, to a thin lipid film. The resulting lipid film was dried for a further 1 hour under nitrogen gas. Next the lipid film was hydrated with phosphate buffer (pH 7.4) (1 mL) sonicated and vortexed vigorously. SMA (50 mg) was added to the opaque lipid solution and incubated for 1 h at 37 °C, giving a

translucent solution. DMPC Polar Lipids (10 mg) were prepared in the same way as above, and incubated for 1 h at 25 °C, giving a translucent solution.

2.6. Purification

Nanodiscs samples (1 mL) were centrifuged at 208000 *g* for 30 minutes at 4 ^{o}C, the supernatant was collected and the pellet discarded. The nanodiscs were then dialysed overnight against 4 L phosphate buffer (20 mM) pH 7 for SMILPs and pH 7.4 for SMALPs with a 50 kDa cut-off dialysis tubing.

Further purification was achieved by gel filtration chromatography where nanodisc samples were concentrated prior to injection, using a centrifugal concentrator with a 30,000 Da MWCO membrane, centrifuged at 3220 *g* (20 min) (4^{o}C) to below 400 µl and fractionated on a Superdex 200 10/300 GL column (GE Healthcare). With a flow rate of 0.5 ml/min, with phosphate buffer pH 7 for SMILPs and pH 7.4 for SMALPs, while monitoring nanodisc absorbance at 260 nm. Pump B on the machinery was initially washed with deionised H_2O and equilibrated in the relevant buffers; all solutions were filtered and degassed accordingly to remove any air and small particles present. Fractions (0.5 ml) were collected for further analysis.

2.7. RI of Nano discs

Nanodiscs were concentrated and purified using a centrifugal concentrator with a 30,000 Da, MWCO membrane at 3220 *g* (20 min) (4^{o}C). The refractive index was determined by taking the average of three samples of nanodiscs, using a manual benchtop refractometer ABBE 5 BS. Hexane was used as a control with an RI 1.375.

2.8. UV-Vis Quantification

Quantification of nanodiscs was carried out through UV-Vis spectrum using NanodropOne_AZY1705795. SMA (165 µM) sample was serial diluted 10 times with a

variety of different concentrations and each sample measured in a quartz cuvette (0.5 mL) this was repeated 3 times. Calibration was preformed prior to use with a blank, and all spectra were zeroed at 750 nm. The λ_{max} was determined and the averages of all 3 plotted in excel giving a linear calibration curve. This was then used to quantify the concentration of nanodiscs in solution through the straight line equation.

2.9. DLS studies

DLS studies were carried out using Anton Paar Litesizer^{TM} 500 and processed using KalliopeTM Professional. All vials used for preparing the samples were clean and dry. All solvents used were filtered to remove any particulates that may interfere with the results obtained. The nanodisc sample sizes were kept to 0.5 mL, and allowed to equilibrate for 10 minutes followed by a series of 10 ‘runs’ on each sample to give enough data to derive an appropriate average. In some instances, the raw correlation data indicated that a greater amount of time may be needed for the samples to reach a stable state. For this reason, only the last 9 ‘runs’ were included in the average size distribution calculations.

2.10. Zeta Potential Studies

Zeta potential studies were carried out using Anton Paar Litesizer^{TM} 500 and processed using KalliopeTM Professional. All vials used for preparing the samples were clean and dry. All solvents used were filtered to remove any particulates that may interfere with the results obtained. The nanodisc samples were measured in an Omega cuvette 0.35 mL, by a series of 10 ‘runs’ on each sample to give enough data to derive an appropriate average.

2.11. Transmission Electron Microscopy (TEM) Imaging

For electron microscopy, a droplet (2 µL) of sample was applied to formvar/carbon coated 600 mesh copper grids (Agar Scientific) and left for 5 minutes at RT. Excess

liquid was aspirated from the grid and a drop of 2 % uranyl acetate (aqueous) was applied to the grid an immediately aspirated. Grids were then dried at room temperature. Images were recorded on a Jeol 1230 TEM operating at an accelerating voltage of 80 kV equipped with a Gatan One View 16 MP digital camera.

2.12. NMR ^{1}H 1D

NMR ^{1}H 1D spectra were determined with a Bruker Avance III 600 Hz spectrometer at 298 K. Data was collected with 32768 points and a spectral width of 16.0242 ppm, receiver gain was set to 256, with 128 scans, 4 dummy scans and an acquisition time of 1.7 s at 298 K. Water suppression was achieved using excitation sculpting 1D, with double pulse field gradient spin echo. All data was processed using Bruker topspin 3.6.1 software, all spectra were phased, baseline corrected and calibrated to the centre of the DSS (4,4-dimethyl-4-silapentane-1-sulfonic acid) peak, with the chemical shifts reported in parts per million (ppm) the peak height in intensity [abs], (the absolute peak intensity) and Intensity [rel], (the relative peak intensity).

2.13. NMR ^{1}H CPMG

NMR ^{1}H CPMG spectra were determined with a Bruker Avance III 600 Hz spectrometer at 298 K. Data was collected with 16,384 points and a spectral width of 16.0242 ppm, receiver gain was set to 256, with 128 scans, 16 dummy scans and an acquisition time of 0.85 s at 298 K. Water suppression was achieved using pre-saturation Watergate block dpfgse_water. The CPMG element used 300 cycles and a delay of 1 ms between 180-degree pulses, Data was processed using Bruker topspin 3.6.1 software, all spectra were phased, baseline corrected and calibrated to the centre of the DSS (4,4-dimethyl-4-silapentane-1-sulfonic acid) peak, with the chemical shifts reported in parts per million (ppm), the peak height in intensity [abs], (the absolute peak intensity) and Intensity [rel], (the relative peak intensity).

2.14. NMR Titration

Stock solutions of compounds **1-3** 5000 µM (550 µL) were dissolved in phosphate buffer (pH 7.4). Compound **1** (539.478 g/mol) (1.48 mg), compound **2** (618.896 g/mol) (1.70 mg) and compound **3** (604.87 g/mol) (1.66 mg). To ensure full solubilisation the compounds were sonicated, heated where necessary and vortexed vigorously. The stock solutions of compounds **1-3** were further diluted to 100 µM (550 µL) before adding to an NMR tube (5 mm). SMALPs were added step-wise to the SSA at varying concentrations starting at 0.01 µM up to 100 µM. NMR ^{1}H 1D and CPMG spectra were obtained at each step, no extra time was given for equilibration. The addition of the SMALPs to the compound gave rise to the concentration of compounds **1-3** decreasing during the experiment; this was corrected by calculating the increase in volume, (Table 1), which led to a lower concentration of the compound at each step and reporting the final result as a molar ratio. The intensity % of the peaks chosen was plotted against the molar ratio of compound: SMALP.

Table 1: *Molar ratio of compound **1-3** to SMALP*

SSA (µM)	E.coli SMALP (µM)	Molar ratio	SSA (µM)	DMPC SMALP (µM)	Molar ratio
100.0	0.0	0.000	100.0	0.0	0.000
99.7	0.2	0.002	99.5	0.2	0.002
99.3	0.4	0.004	99.0	0.4	0.004
99.0	0.6	0.006	98.6	0.6	0.006
98.7	0.8	0.008	98.1	0.8	0.008
98.3	1.0	0.010	97.6	1.0	0.010
97.5	1.5	0.015	96.5	1.5	0.016
96.8	2.0	0.021	95.4	2.0	0.021
95.2	3.0	0.032	93.2	3.0	0.032
93.7	4.0	0.043	91.1	4.0	0.044
93.4	6.0	0.064	90.7	6.0	0.066
93.1	8.0	0.086	90.3	8.0	0.089
92.8	10.0	0.108	89.9	10.0	0.111
92.1	15.0	0.163	89.0	15.0	0.169
91.4	20.0	0.219	88.0	20.0	0.227
90.7	25.0	0.276	87.1	25.0	0.287
87.4	50.0	0.572	82.7	50.0	0.605
84.3	75.0	0.890	78.8	75.0	0.952
81.4	100.0	1.229	75.2	100.0	1.330

3. Results and Discussion

3.1. General Structure of Compounds

All compounds used in this study form part of a series of novel supramolecular amphiphilic antimicrobials. The general structure consists of a hydrogen bond donor group and an acceptor group in one molecule that can self-associate through one or more hydrogen bonds.

For this study the interactions between SMALPs and three individual amphiphilic compounds were investigated.

Compound **1**: consists of a (trifluoromethyl)benzene aromatic, with a HBD and HBA urea moiety, and a HBA sulfonate functionality, with a TBA counter cation (Figure 7).

Compound **2**: Consists of 2-phenylbenzo[d]thiazole fluorescent moiety in the para position, with HBD, HBA urea moiety and HBA sulfonate functionality, with a TBA counter cation (Figure 7).

Compound **3:** Consists of a 2-phenylbenzo[d]thiazole fluorescent moiety in the ortho position, with HBD, HBA urea moiety and HBA sulfonate functionality, with a TBA counter cation.(Figure 7)

3.2. Poly(styrene-co-maleimide) (SMI_{2000l})

SMI_{2000l} was not soluble in a deprotonated form, the method used to solubilise the resin was protonation, which formed a soluble salt acid from the Poly(styrene-co-maleimide). This involved the use of a reflux setup, which gradually heated the solution to reflux at 100 °C. Prior to adding the resin to the HCl the resin was ground in a pestle until a fine powder to reduce the reaction time. The HCl gave an acidic aqueous environment, which led to protonation of the ternary amine, giving a cationic derivative. The protonation of the ternary amine group was essential in the polymer becoming water soluble.[59] (Figure 9) Next the polymer was precipitated by increasing pH to 8 with the addition of NaOH, and washed before undergoing lyophilisation, which resulted in a dry white powder.

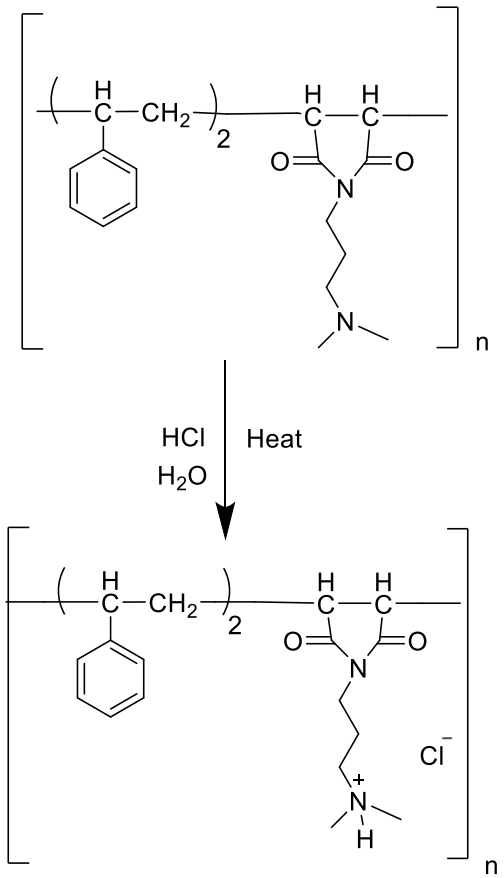

Figure 8: *Reaction schematic for the protonation of SMI.*

3.3. Styrene-maleic Anhydride (SMAnh)

SMA_{2000} was not soluble as an anhydride, the method used to solubilise the powder was deprotonation, which formed a soluble acid from the SMAah. The method used for the hydrolysis of the anhydride to the acid involved the use of a reflux setup, which gradually heated the solution to reflux at 100 °C. The NaOH gave an alkaline aqueous environment, where the hydroxide ions were consumed. This was by either acting as a nucleophile and reacting with the anhydride ring and/or acting as a base deprotonating the resulting carboxylic acids (COOH → COO−) that were formed when the anhydride ring opened. The deprotonation of the acidic groups was important in the polymer becoming water soluble.[60] (Figure 10) Next the polymer was precipitated by reducing the pH to below 5 with the addition of concentrated HCl. and washed before undergoing lyophilisation, which resulted in a dry white powder.

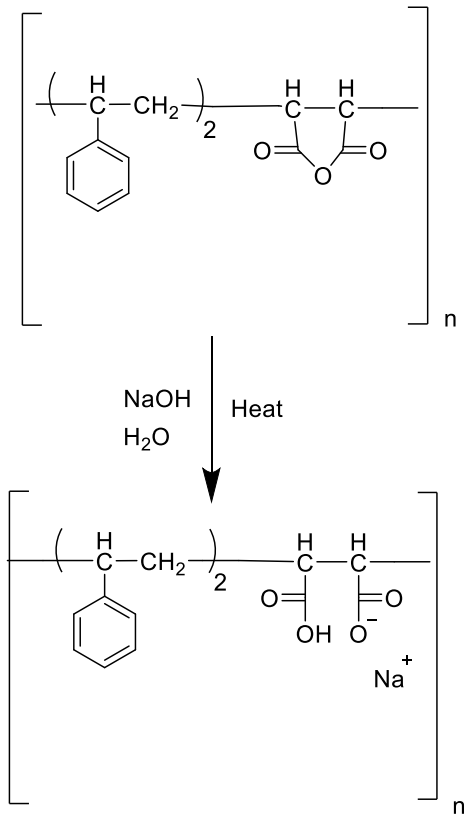

Figure 9: *Reaction schematic for the deprotonation of styrene-maleic anhydride.*

3.4. Nanodiscs

There are three types on nanodiscs that were investigated, *E.coli* SMILPs, *E.coli* SMALPs and DMPC SMALPs. Here *E.coli* lipids are representing a prokaryotic bacterial membrane, with PE as the most abundant lipid present and the DMPC lipids represent a eukaryotic mammalian membrane.

DMPC lipid nanodiscs alone are a simplistic mimetic of the eukaryotic membrane; for this preliminary study it's suitable as a model due to the composition of the outer eukaryotic membrane containing predominantly PC lipids. Although PE lipids make up ~40% of the eukaryotic membrane these are contained within the inner leaflet, and do not play a part in the membrane interactions with other compounds such as SSAs, hence this allows for the discrimination between the membrane types.

The difference between the SMILPs and the SMALPs was the copolymer that belted the lipid bilayer together. The SMI polymer was cationic and stable under both neutral and acidic conditions and the SMA polymer is anionic and only stable under neutral or basic conditions. Both of the polymers preformed similarly and were able to solubilise the lipid bilayers in to nanodiscs, this was observed through the solution changing from a cloudy solution to a translucent solution, upon the addition of the copolymer. With the *E.coli* lipid extract the transition temperature needed to be higher than the DMPC lipid extract. This led to a higher incubation temperature; that was a direct effect of the *E.coli* lipids containing PE as its most abundant lipid.[61,62] The head group of the PC is larger that of PE due to the three methyl groups attached to the amine, which PE lipids do not have, this causes sterically hindered electrostatic interactions and causes weaker lipid to lipid interactions, hence less energy is required to solubilise the membrane.[19]

3.5. Purification of Nanodiscs

After the nanodiscs were formed they were purified using various techniques to ensure a pure sample of nanodiscs. First the nanodiscs were centrifuged, at 208000 *g* for 30 mins at 4 ^{o}C, this forced any unbound lipids to the bottom of the sample and only the supernatant was collected with the formed nanodiscs. All three samples produced only a small amount of insoluble material as a pellet, which was discarded. This indicated that the majority of the lipids were bound by the copolymers and in solution.

Next the nanodiscs were separated from any remaining reagents and low molecular weight products, such as free copolymer by dialysis against 4 L phosphate buffer (20 mM) pH 7 for SMILPs and pH 7.4 for SMALPs with a 50 kDa cut-off dialysis tubing. The conditions for the SMI copolymer were required to be slightly acidic to avoid precipitation.

Further purification was achieved by gel filtration chromatography, which separated the nanodiscs by their size. The first eluted particles are the biggest, followed by the smaller ones. This is due to the smaller particles spending more time in the pores, within the column, where the larger ones cannot fit. The elution of the nanodiscs was detected using UV-Vis at 260 nm, which allowed for the identification of aggregates containing styrene. The fractions were collected and the size of the nanodiscs analysed with DLS prior being mixed together and concentrated back to ~1 mL. This procedure assured that in every sample only the fractions containing the correctly assembled, homogenous nanodiscs were collected and used for further experiments. Any other larger or smaller aggregates that may have still been present were discarded. Fractions (0.5 ml) were collected for further analysis with DLS to determine the size of the particles.

DLS is commonly used to detect the particle size of a sample, in an aqueous environment. Fractions (0.5 ml) were eluted and collected from ~10 ml to ~20 ml depending on UV-Vis detection, each fraction was analysed with DLS in disposable

cuvettes of 500 μL to determine the size of particles present. The results of the particle size were as expected, particles that eluted at 16.5 ml (Figure 10 **a**) were ~100 nm in size, and the ones that eluted at 19 ml **(**Figure 10 **b**), were ~10 nm in size. Here sample **a**, was discarded and sample **b**, was stored at 5 ^{o}C for further studies.

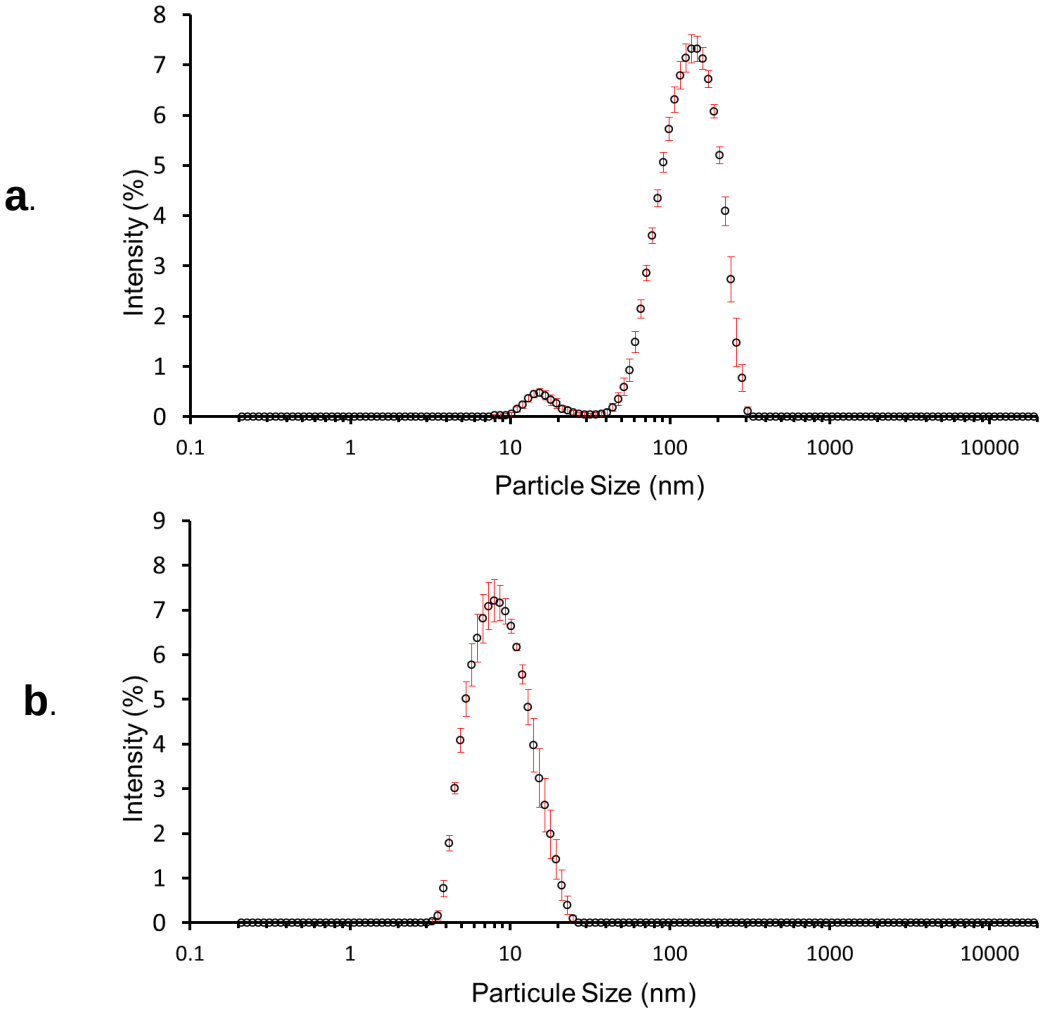

Figure 10: *Gel filtration chromatography DLS results.*

Average intensity particle size distribution of E.coli SMALPs, in phosphate buffer pH 7.4, calculated from 9 DLS runs at 298 K. Error given is the standard error of the mean.

3.6. Index of refraction for Nanodiscs

A refractometer measures the amount of light that is refracted within a sample. The refractive index (RI) of the nanodiscs needed to be established to aid in DLS studies on particle size. First the SMILP sample was concentrated in a centrifugal concentrator to remove excess PB, to ensure the resulting RI was from the nanodiscs and not the PB. The RI was determined by taking the average of three samples of nanodiscs, resulting in an average RI of 1.35,(see Table 1) All samples were measured on a manual benchtop refractometer. The RI of Hexane is well documented at 1.375 at 20ºC; this was used as a control to ensure the results were reliable.

Table 1: Index of refraction for nanodiscs

Sample	Index of refraction
Hexane	1.375
Phosphate buffer pH 7.0	1.335
SMI copolymer	1.341
SMILPs sample 1	1.349
SMILPs sample 2	1.349
SMILPs sample 3	1.350

3.7. Optimisation

The first nanodiscs investigated were the SMILPs, for their size and stability to determine the most viable nanostructure, for the binding association studies.

3.7.1. DLS intensity weighted particle size distribution of SMILPs

DLS is commonly used to detect the particle size of a sample, in an aqueous environment. This technique can be used on a small amount of sample typically 1 mL and is non-invasive. This makes it an ideal tool for extensive particle analysis.

DLS was used to establish the average intensity particle size distribution; this was done to determine if the nanodiscs had successfully formed. The first sample of nanodiscs measured was the *E.coli* SMILPs; these formed the majority of particles in solution around 10 nm, (Figure 11). This size of nanodiscs formed with SMI was coherent with the reported size in literature which is around ~6 to 12 nm.[51] Another peak formed around 100 to 1000 nm which may be due be aggregation, or dust particles. The size is determined by the contribution of each particle in the distribution, to the intensity of light scattered by the particle.[63]

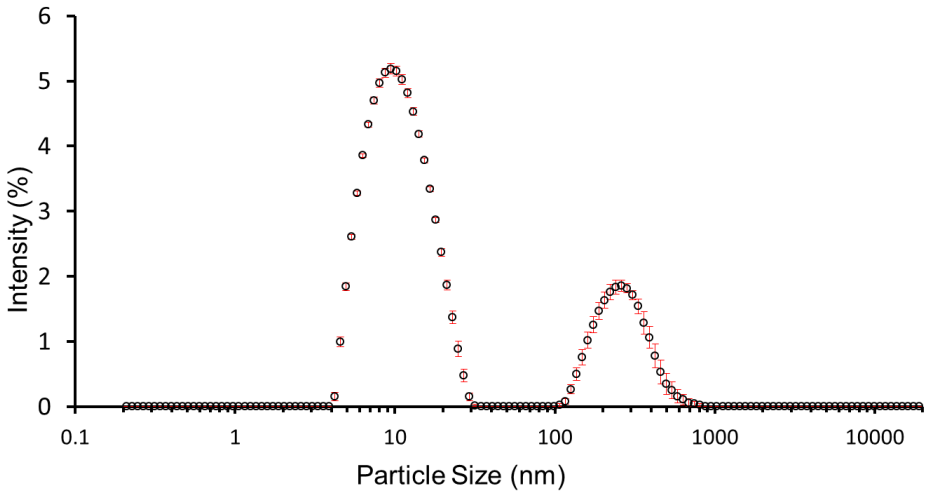

Figure 11: *Average intensity particle size distribution of E.coli SMILPs.*

Average intensity particle size distribution of *E.coli* SMILPs, in phosphate buffer pH 7.0, calculated from 9 DLS runs at 298 K. Error given is the standard error of the mean.

3.7.2. DLS number weighted particle size distribution of SMILPs

The number weighted distribution is useful in determining the number of particles of a certain size in solution. The same set of DLS data used in plotting, Figure 12, also reports the average number weighted particle size distribution.

All of the particles in solution were within the size range of ~5 nm to 12 nm, with no sign of larger aggregates,(Figure 12). This is due to the number contribution from the larger aggregates is so small (<0.001%) that it is no longer considered relevant and not displayed. This further confirms that the peak on Figure 11, of 100-1000 nm is from an anomaly within the sample.

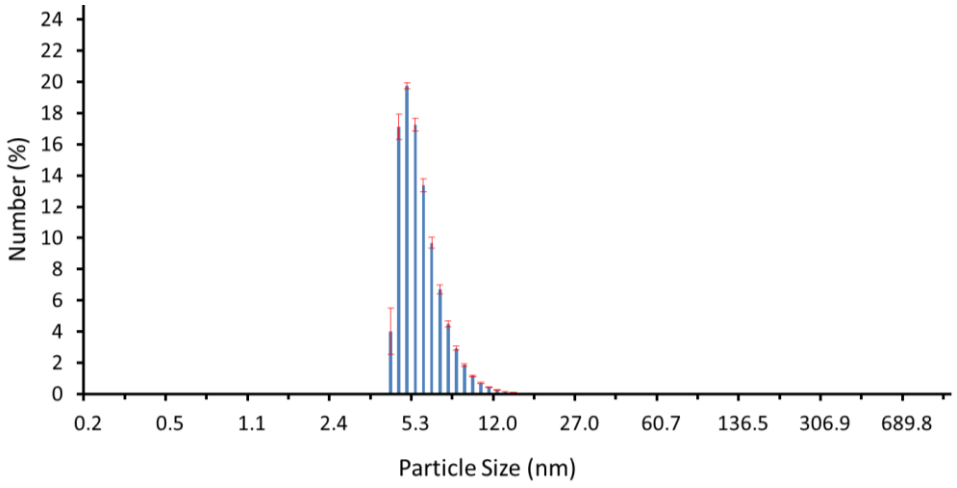

***Figure 12**: Average number weighted particle size distribution of E.coli SMILPs.*

Average number weighted particle size distribution of *E.coli* SMILPs, in phosphate buffer pH 7.0, calculated from 9 DLS runs at 298 K. Error (standard error of the mean)

3.7.3. DLS correlation function data

The correlation function gives information about the signal-to-noise ratio as well as on the presence of dust particles or aggregate. The degree of similarity between the signals is processed; a strong correlation indicates that the data is consistent and therefore reproducible.

The correlation data for the SMILPs is from the same data set as the particle size distributions. All of the 9 runs were all consistent and therefore the data collected regarding the size of the particles is credible, (Figure 13).

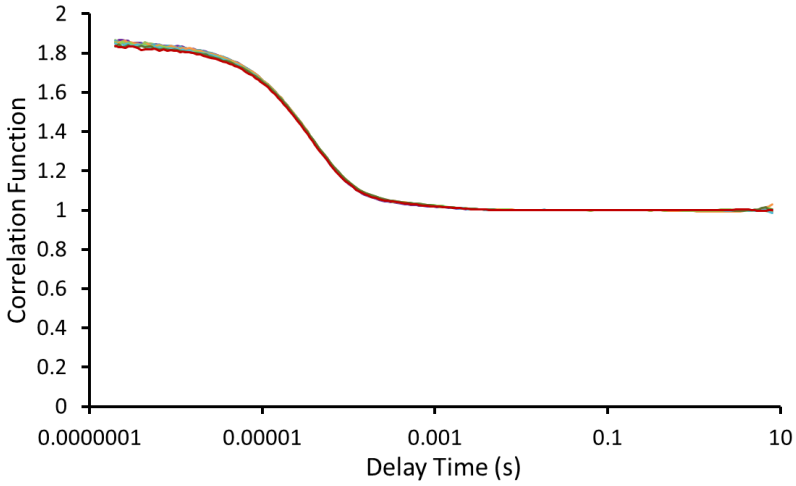

***Figure 13**: Correlation function data for E.coli SMILPs.*

The correlation function data for *E.coli* SMILPs was calculated from 9 DLS runs at 298 K

3.7.4. TEM Imaging of SMILPs

The next step to investigate the formation of nanodiscs is to visualise them using TEM. After experiencing precipitation within the sample, storage conditions were investigated. The SMILP sample was divided in half and stored in different environments overnight. One was stored at 4^{o}C and the other at RT. The sample stored at 4^{o}C became slightly cloudy, indicating that the structures were disassembling. Images were taken of both samples for comparison. The spherical shapes in Figure 14,

were from the sample stored at 4^{o}C and not believed to be nanodiscs, as the solution was slightly cloudy due to precipitation. The presence of formed nanodiscs in Figure 15 is questionable.

Negatively stained uranyl acetate TEM image showing results from *E.coli* SMILPs (Figue 14) sample stored at 4^{o}C, Visual evidence of nanodiscs was questionable Scale bar =100 nm

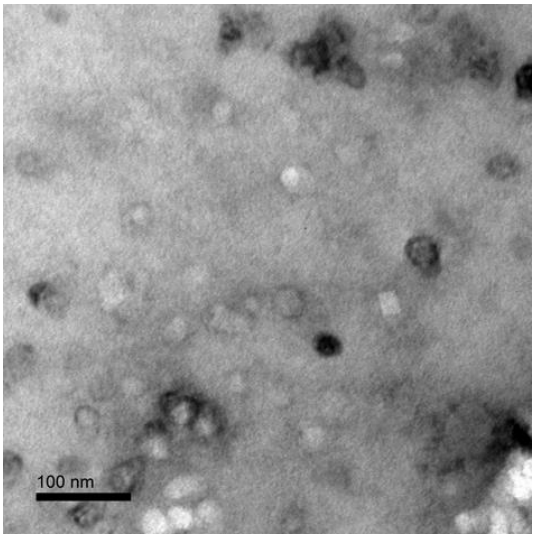

Figure 14*: TEM image showing results from E.coli SMILPs.*

Negatively stained uranyl acetate TEM image showing results from *E.coli* SMILPs sample stored at RT. (Figur 15) Visual evidence of nanodiscs was questionable. Scale bar =100 nm

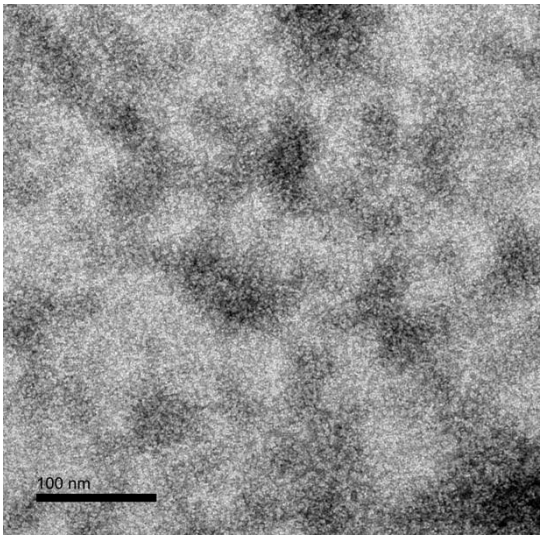

Figure 15: *TEM image showing results from E.coli SMILPs.*

3.7.5. Viability of SMILPs

SMILPs were formed successfully, however the nanodisc samples were found to be unstable and precipitated upon storage (4 ^{0}C) over a short period of time (~24 hours). Further storage conditions were investigated, such as RT, which slightly increased the longevity on the nanostructures. TEM images were acquired; however the identification of nanostructures was questionable within the images. It was also determined that the SMILPs were precipitating during the purification stage causing impairment to the Superdex 200 10/300 GL column. Alternative purification techniques were also investigated, however due to the instability of the nanodiscs, the copolymer SMI was substituted with SMA and SMILPs were not used any further in this study.

3.7.6. Conclusion

In literature SMI copolymer is deemed to be a a more versatile copolymer in forming nanodiscs. This is due to the SMI not being affected by acidic pH or high concentrations of divalent cations.

The nanodiscs in this study were formed in a neutral environment, with no divalent cations present, however this polymer was investigated due to comparable efficiency to SMA.

Although the SMI has a similar thermodynamic driving force for the formation of nanodiscs, it was found in a study that SMI had slightly larger negative free energy change upon interaction with the lipids, [51] when being compared with SMA. This indictes a less favorable self-assembly for SMI and may of contributed to the unstability of the SMILPs.

3.8. SMALP Results and Discussion

3.8.1. UV-Vis Quantification

Nanodiscs are often quantified by the protein encapsulated within the structure; however in this study the nanodiscs didn't contain any protein and so a new method was formulated to quantify the amount of discs in solution.

A calibration curve is a common method for determining the concentration of a substance in an unknown sample by comparing the unknown to a set of standard samples of known concentration.

First SMA (165 µM) was serial diluted 10 times, and the resulting absorbance at $\boldsymbol{\lambda}_{max}$ (260 nm) was plotted against the concentration, giving a linear calibration curve (Figure 16). This was then used to determine the concentration of the purified SMALP samples, by detecting the amount of SMA present. The SMALPs were diluted 1:10 dilution prior to obtaining the absorbance value; this was due to a high absorbance reading with the original sample, which fell outside of the instrument's linear range. The final concentration was determined using the straight line equation. $y = mx + c$

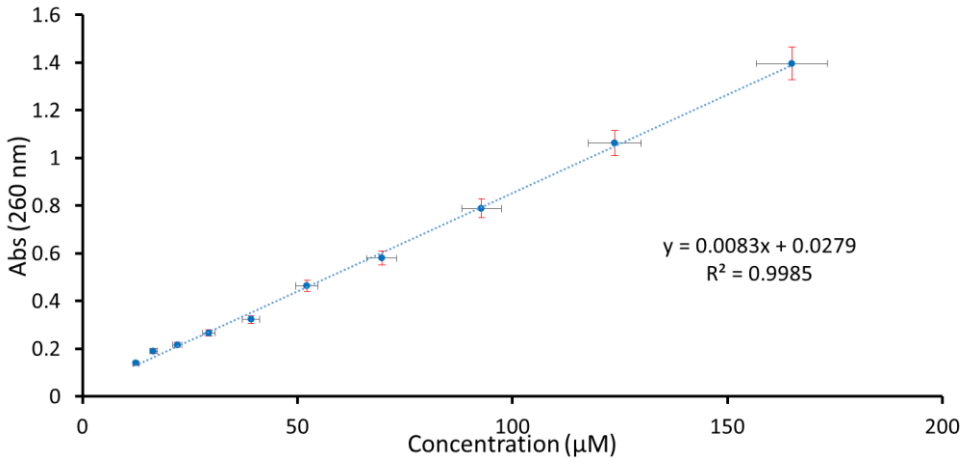

Figure 16: *Calibration curve for SMA in PB. Error given is the standard error of the mean.*

The concentration of SMA relates directly to the concentration of nanodiscs in solution. In literature previous studies have shown that one SMA chain will form one nanodisc.[64]

The length of the SMA polymer chain depends on the styrene to maleic acid ratio. The SMA used in this research was a 2:1 ratio with a molecular weight of 7500 g/mol, this gives a polymer chain length of ~24 monomeric units. For the purpose of this research the assumption was made that one SMA polymer chain produces one nanodisc.

3.8.2. DLS average intensity particle size distribution

The average intensity particle size distribution is a well-known technique for the determination of particle size. This technique is the most accurate to determine the size of the SMALPs as it measures hydrodynamic diameter as particle diffuses within a fluid.[65] DLS was used to establish the average intensity particle size distribution to determine if the SMALPs successfully formed. The *E.coli* SMALPs intensity distribution resulted in two peaks, one around 10 nm, that indicates that the nanodiscs have formed and another 100 nm, indicating that another larger particle may be present, (Figure 17). In this set of results the size of DMPC SMALPs were also investigated, and resulted in two peaks, one around 10 nm, that indicates that the nanodiscs have formed and another smaller one around 100 nm,(Figure 18). This as previously mentioned may be due to aggregation, or dust particles.

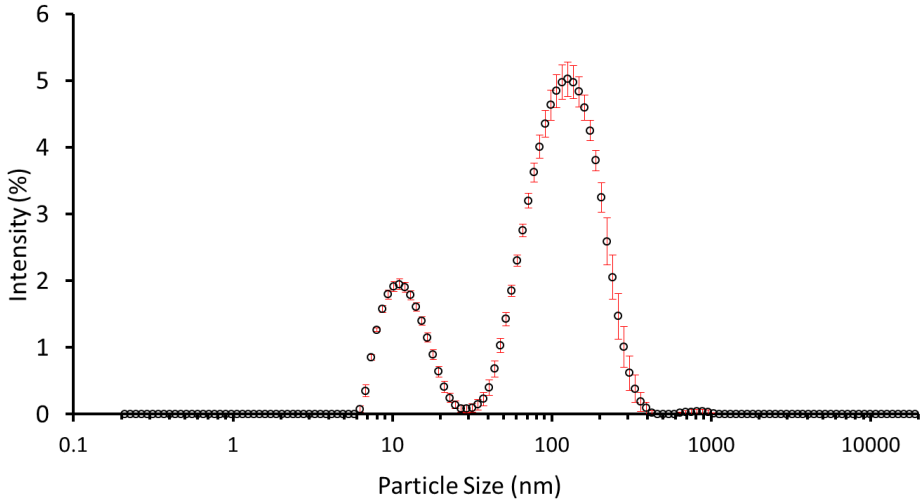

Figure 17: *Average intensity particle size distribution of E.coli SMALPs (326.6 µM).*

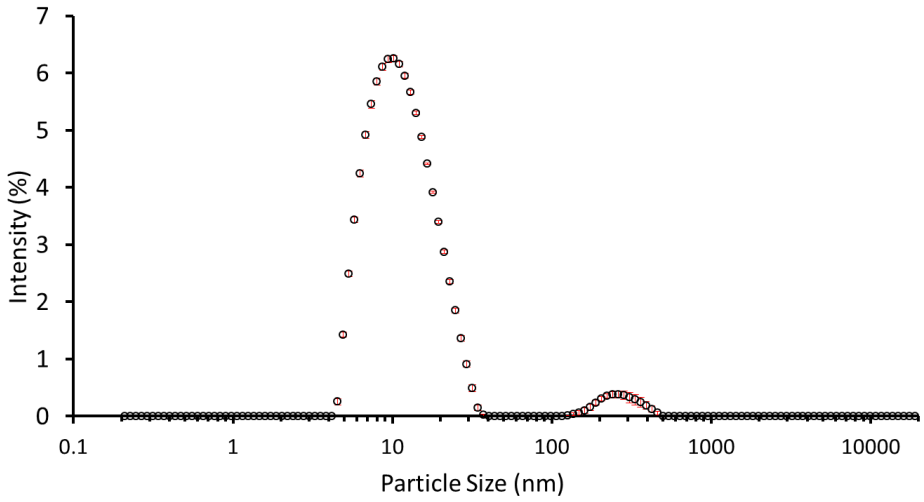

***Figure 18**: Average intensity particle size distribution of DMPC SMALPs (412 µM).*

The results from the average intensity particle size distribution of *E.coli* SMALPs (326.6 µM) and DMPC SMALPs (412 µM) was suspended in phosphate buffer pH 7.4, and calculated from 9 DLS runs at 298 K. Error given is the standard error of the mean.

3.8.3. DLS Number weighted particle size distribution

To obtain more detail about the size of the nanodiscs, the number distribution was investigated, which reports the smallest size measured in solution. This data is supporting information to the average intensity particle size distribution, and is not a viable way to measure the size of particles alone.[63]

The Number weighted particle size distribution was determined to further investigate the particle size of the SMALPs. The same set of DLS data used in plotting Figure 17/18, also reports the average number weighted particle size distribution as previously mentioned. All of the particles in solution were within the size range of ~5 nm to 12 nm, (Figure 19/20) which was coherent with the size reported in literature. Both graphs do not display the larger aggregates, which were present with the intensity weighted graphs. This is due to the number contribution from the larger aggregates was so small (<0.001%) that it is no longer considered relevant and therefore not displayed. This

further confirms that the peak on Figure 17, of 100-1000 nm was from an anomaly within the sample.

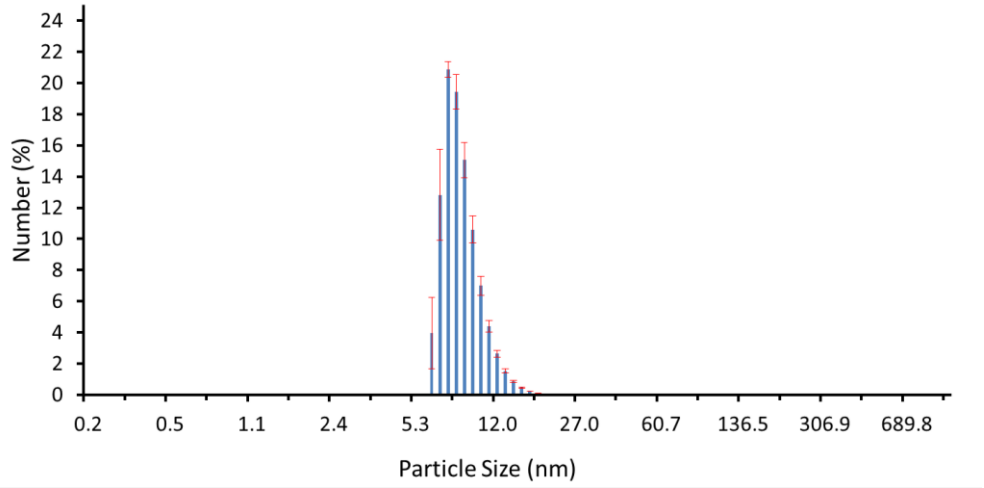

***Figure 19**: Average number weighted particle size distribution of E.coli SMALPs (326.6 µM).*

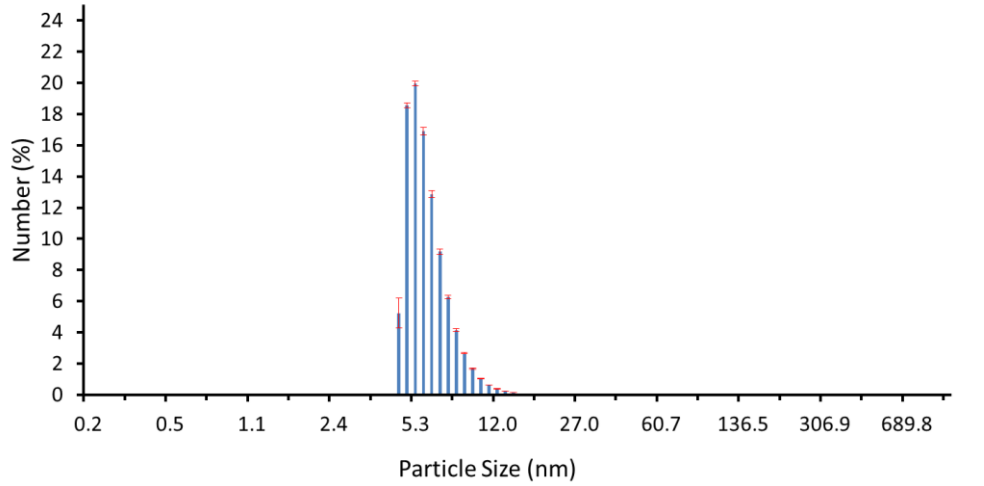

***Figure 20**: Average number weighted particle size distribution of DMPC SMALPs (412 µM).*

Results from the number weighted particle size distribution of *E.coli* SMALPs (326.6 µM) and DMPC SMALPs (412 µM) suspended in phosphate buffer pH 7.4, and calculated from 9 DLS runs at 298 K. Error given is the standard error of the mean.

3.8.4. DLS correlation function data

The correlation function data was determined to establish the uniformity of the sample. With the same set of data from used to determine the size. Correlation data for the *E.coli* SMALPs (Figure 21) shows than the 9 runs were all consistent, and the DMPC SMALPs (Figure 22) show only a slight variation in the correlation function, which is still considered to be acceptable data. Therefore given the repeatable correlation functions, the data collected regarding the size of the particles for both *E.coli* and DMPC SMALPs is credible.

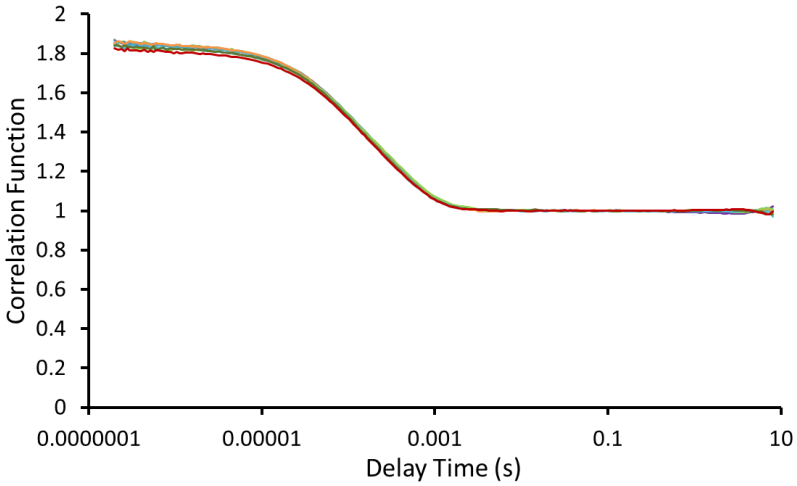

Figure 21: *Correlation function data relating for E.coli SMALPs (326.6 µM).*

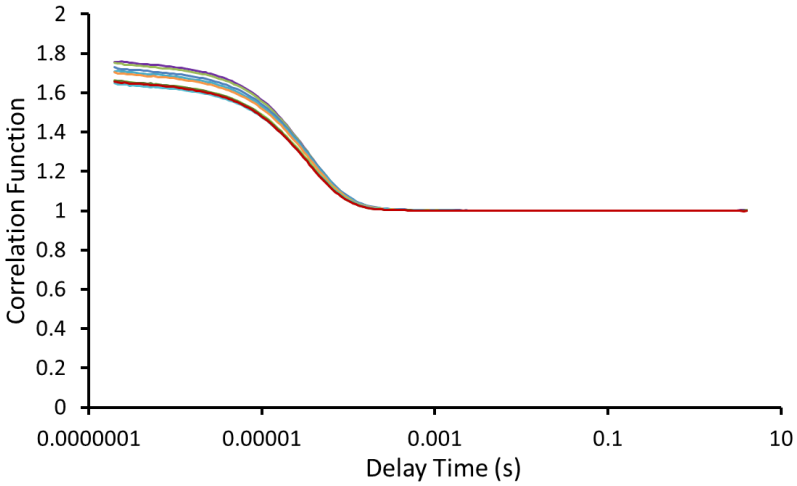

Figure 22*: Correlation function data for DMPC SMALPs (412 µM),*

Results from the correlation function data relating to average intensity weighted particle size and the average number weighted particle size for both *E.coli* SMALPs (326.6 µM) and DMPC SMALPs (412 µM), calculated from 9 DLS runs at 298 K.

3.8.5. Zeta potential

Zeta potential is a measure of magnitude of charges on nanoparticles and provides information about particle stability. The zeta potential relates to charged species present at the particles surface, that impairs aggregation and/or precipitation, higher magnitude of potential increases electrostatic repulsion within the colloidal system. The more positive or negative the zeta potential is, increases the colloidal stability, a value of +/-30 mV indicates good stability. [66]

The zeta potential of the SMALPs was measured to determine the stability of their structure. The mean zeta potential for the *E.coli* SMALPs is -47.66 mV, (Figure 23). The mean zeta potential for the DMPC SMALPs is -8.50 mV (Figure 24). This shows the stability of *E.coli* SMALPs to be slightly higher than the stability of DMPC SMALPs, due to the increased zeta potential and therefore increased colloidal stability.

The zeta potential determined for DMPC SMALPs is deemed to be fairly unstable with a low mean average. The *E.coli* SMALPs were more stable with a slightly higher mean average. Samples that have low zeta potential are coherent with poor physical stability, and are more susceptible to aggregation and/or precipitation. [67] As a result the SMALPs were regularly checked with DLS to determine whether or not there were any changes to the samples.

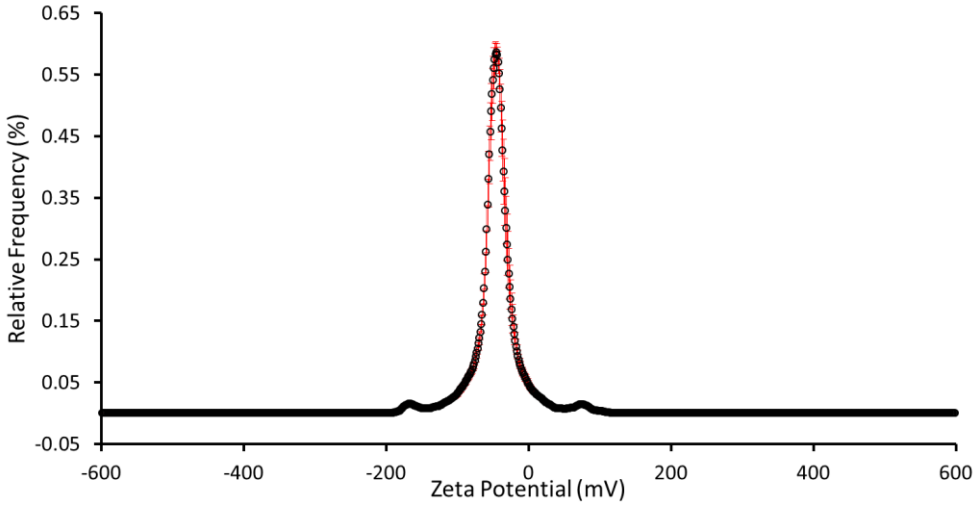

***Figure 23**: Zeta potential data for E.coli SMALPs (326.6 µM).*

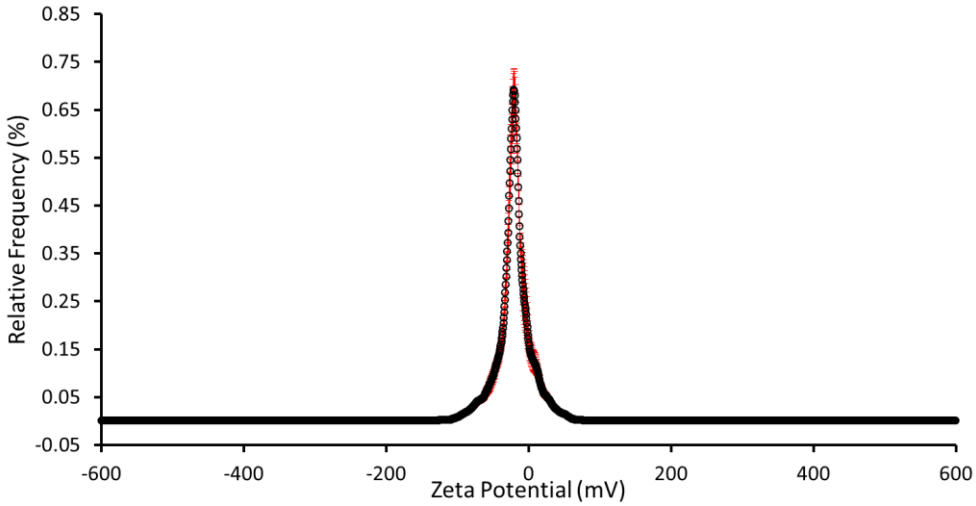

***Figure 24:** Zeta potential data for DMPC SMALPs (412 µM).*

The graphs display the results for zeta potential data for *E.coli* SMALPs (326.6 µM) with a mean average of -47.66 mV and DMPC SMALPs (412 µM) with a mean average of -8.50 mV, calculated from 10 DLS runs at 298 K. Error given is the standard error of the mean.

3.8.6. TEM Imaging of SMALPs

The next step to investigate the formation of nanodiscs was to visualise them using TEM. The negatively stained uranyl acetate TEM results showing images of *E.coli* SMALPs in Figure 25. The image has been enlarged with red circles, indicating the spherical shapes.(Figure 26) Visual evidence of spherical structures was observable and coherent with the size of reported nanodiscs ~10 nm, this further confirms the presence of formed SMALPs.

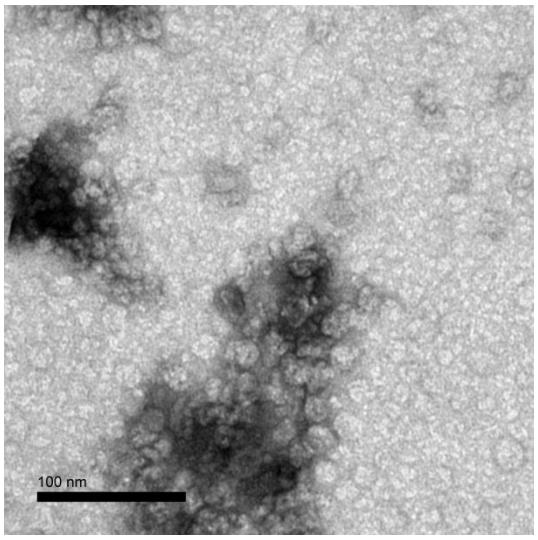

***Figure 25**: TEM image of E.coli SMALPs sample. Scale bar =100 nm*

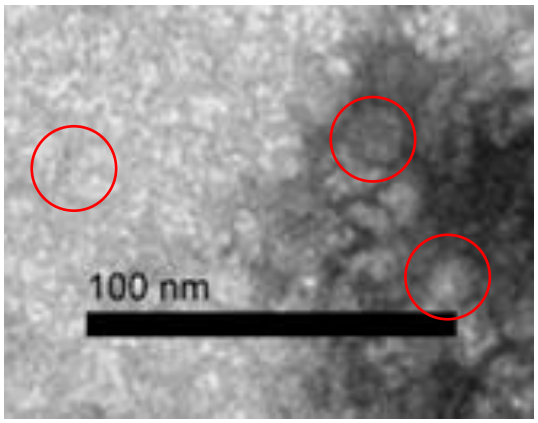

***Figure 26**: Enlarged TEM image of E.coli SMALPs sample. Scale bar =100 nm*

TEM results shows images of DMPC SMALPs in Figure 27. The image has been enlarged with red circles, indicating the spherical shapes (Figure 28). Visual evidence of spherical structures was observable and coherent with the size of reported nanodiscs ~10 nm, this further confirms the presence of formed SMALPs.

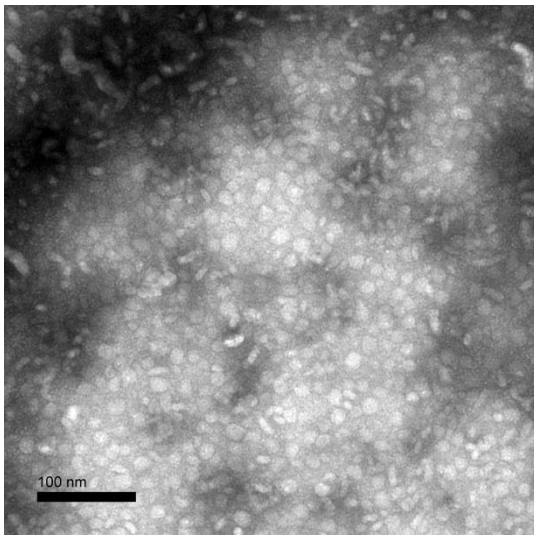

Figure 27: *TEM image of DMPC SMALPs sample. Scale bar =100 nm*

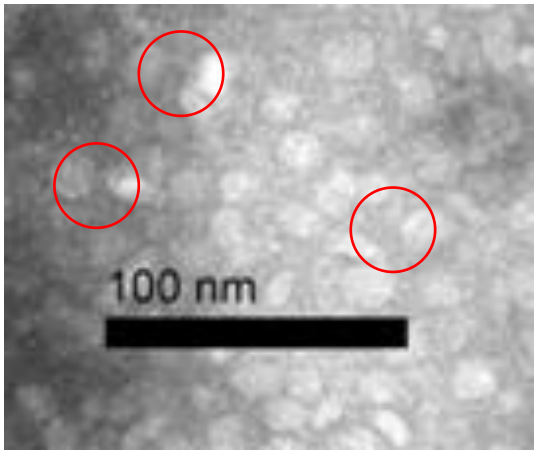

Figure 28: *Enlarged TEM image of DMPC SMALPs sample. Scale bar =100 nm*

3.9. NMR Results and Discussion

3.9.1. Hydrogen preferential binding mode

The most abundant lipid component of *E.coli* lipid extract is PE lipid; it is hypothesised that the SSAs can bind to PE SMALPs more than to the PC SMALPs. This is due to the unhindered electrostatic interactions of the PE phospholipid headgroups. This is useful as the SSAs will have selectively towards bacterial membranes, and not towards mammalian eukaryotic cells.

The electrostatic interactions include hydrogen bonding. The hypothesised HBD and HBA headgroup binding modes for SSA with PE, can be seen in, Figure 29. Here the SSA can interact with the phospholipid headgroup, through hydrogen bond associations to induce antimicrobial activity, causing membrane disruption on the surface of the cytoplasmic membrane, which can then lead to cell death.

The hypothesised HBD and HBA headgroup binding modes for SSA with PC can be seen in, Figure 30. The SSA is not able to form all of the hydrogen bonds and interact with the phospholipid headgroup. This is due to three methyl groups present that sterically hinder the electrostatic interactions;[19] this impedes the hydrogen bonding to the eukaryotic cell membrane and therefore will not cause membrane disruption to the mammalian cells.

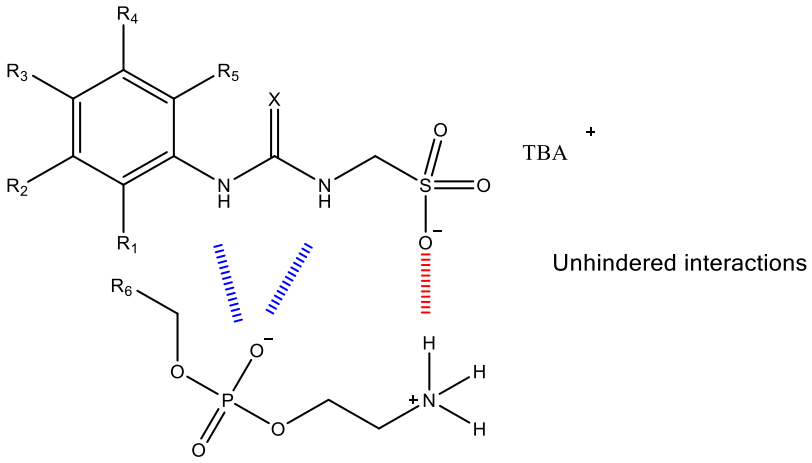

***Figure 29**: Hypothesised unhindered HBA and HBD preferential binding modes with SSA: PE headgroup.*

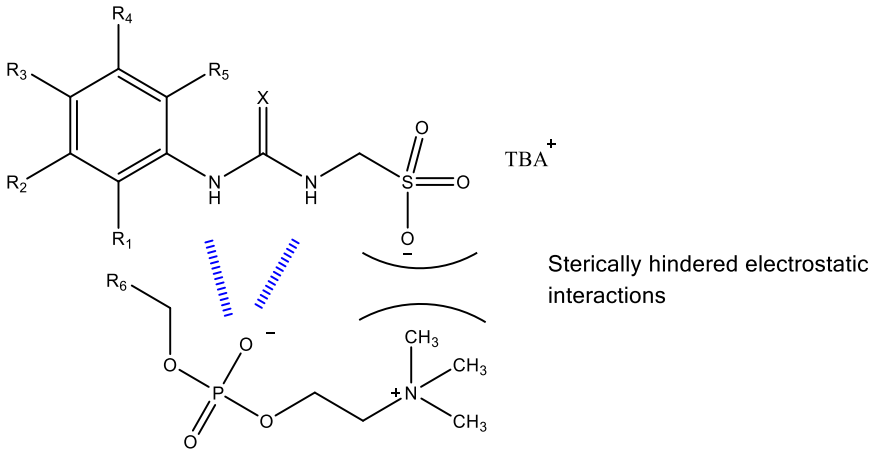

***Figure 30:** Hypothesised sterically hindered electrostatic interactions and HBA and HBD preferential binding modes with SSA: PC headgroup.*

3.9.2. NMR ^{1}H 1D DMPC and *E.coli* [SMALPs]/ [Compound 1]

NMR was an ideal technique for observing the interactions between the SSAs and the SMALPs.[42] To investigate the interactions of **1-3**, with phospholipid nanodiscs, ^{1}H NMR titration studies with SMALPs were conducted. All of the results for ^{1}H 1D NMR comparison show the change in intensity % for compounds **1-3**. The concentration of the SMALPs (guest) was increased against compounds **1**, **2** and **3**, (host) (100 μM) (550μL) and represented as a molar ratio [SMALPs]/[Compound **1-3**] which permitted comparable results. This technique was based on observing the SSA in its free

unbound state, to the SSA-SMALP bound state. This was observed by NMR with the resonance frequency which is directly proportional to the strength of the magnetic field applied; therefore the electromagnetic frequency signal is the same as the magnetic field at the nucleus of the complex being observed.

To determine the interactions of the SSA to the SMALPs, a series of NMR titration studies were performed. The spectra were phased, base line corrected and calibrated to the centre of the solvent peak. Within the data the optimal peak to monitor was selected and determined. The aromatic peaks of the compounds from the NMR spectra were selected, and monitored for peak reduction. This indicates that the compound is binding to the nanodiscs, creating larger structures and this causes the peak to eventually become very broad and can no longer be detected by NMR. The aromatic peaks were deemed to be the most reliable as they did not readily exchange hydrogens with the solvent (water), which happens with the N-H group of the molecule. Only one peak from the aromatic region from spectra was analysed, it is noted that analysing two or more peaks average intensity, may have produced less noisy more reliable data. The spectra of SSA alone does not display any evidence of supramolecular complexes formed, this is due to the low concentrations. However with the addition of SMALPs the peaks observed become less intense and broader peaks appear suggesting that larger supramolecular complexes are being formed, this can be seen in the NMR stack plots below. Tables with the full sets of the data collected for the ^{1}H NMR titration studies and ^{1}H 1D NMR Spectra for compound **1-3** (100 µM) can be found in the appendices.

The first set of results were the change in intensity % against the molar ratio of DMPC and *E.coli* [SMALPs]/ [Compound **1**], (Figure 31). All of the Data for the NMR results were plotted in excel. The first point on the graph represents ^{1}H 1D NMR data of the SSA in its free unbound state. The plotted graph shows successfully binding to the SMALPs; this was confirmed through the decrease in intensity %, which is a direct

effect of part of the SSA being in a bound state and no longer detectable by NMR. However this drop in intensity was similar for both the *E.coli* and DMPC compositions, this was seen with the plotted data. This indicates that they both have a similar degree of association, which was not expected, further investigative methods were required. ^{1}H 1D NMR graph is for clarification of the lower value molar ratio [SMALPs]/ [Compound **1**] (Figure 32). The non-uniform data within the results is later discussed.

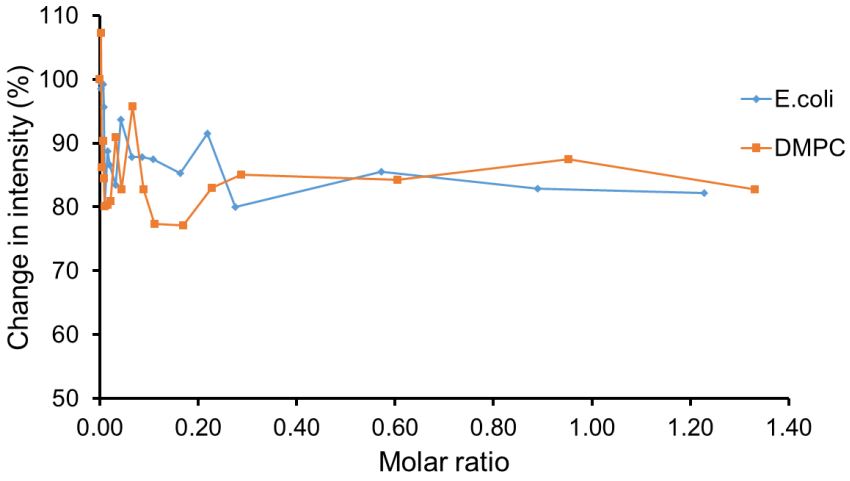

***Figure 31**: ^{1}H 1D NMR results for DMPC and E.coli [SMALPs]/ [Compound **1**]*

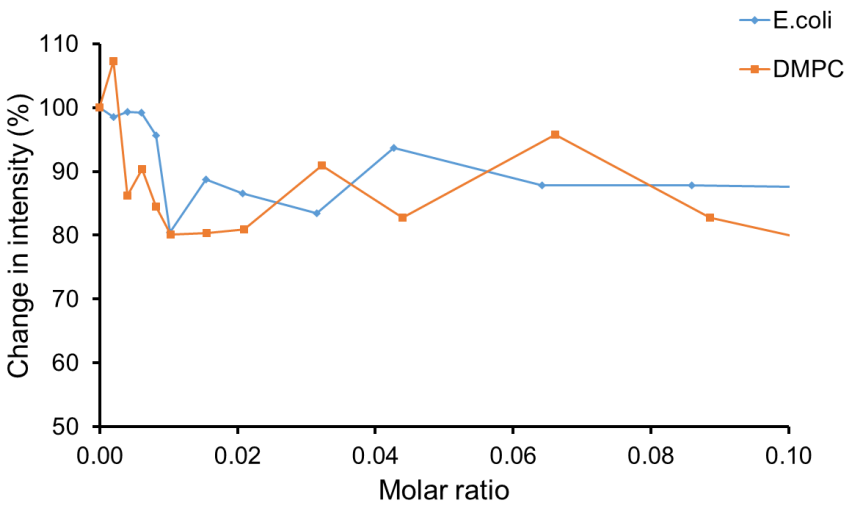

***Figure 32**: ^{1}H 1D NMR results for DMPC and E.coli [SMALPs]/ [Compound **1**] zoomed in*

The concentrations of the molar ratios chosen for the stack plots can be found in Table 2. Full set of measurements and ^{1}H 1D NMR Spectra for compound **1** (100 μM**)** can be found in the appendices.

Due to the concentration of the SMALPS being slightly different the molar ratios also differ slightly. The concentration added of SMALPs was consistent however the volume was slightly different. In retrospection it would have been better to dilute down or concentrate the SMALPs to the same concentrations prior to starting the NMR titrations.

***Table 2:**: Colour scheme for NMR spectra stack plots with matching molar measurement.*

Colour	E.coli Molar ratio	DMPC Molar ratio
Yellow	0.000	0.000
Purple	0.010	0.010
Green	0.108	0.111
Red	0.572	0.605
Blue	1.229	1.330

NMR spectra stack plot for *E.coli* [SMALPs]/ [Compound **1**] (Figure 33) arrow indicates peak observed at 7.6651 ppm and DMPC [SMALPs]/ [Compound **1**] (Figure 34) arrow indicates peak observed at 7.6664 ppm.

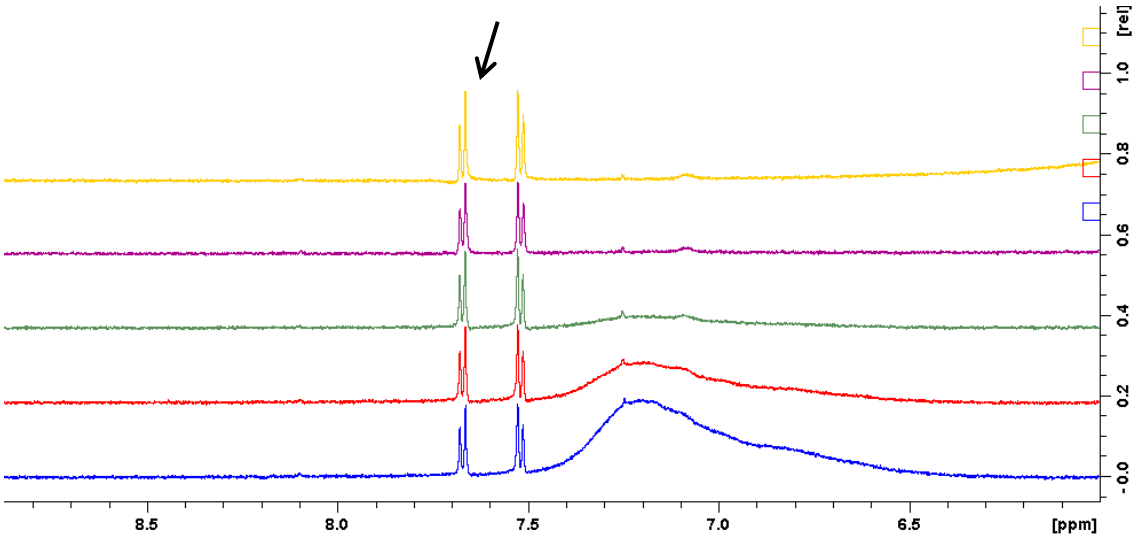

***Figure 33:** ^{1}H 1D NMR spectra stack plot for E.coli [SMALPs]/ [Compound **1**]*

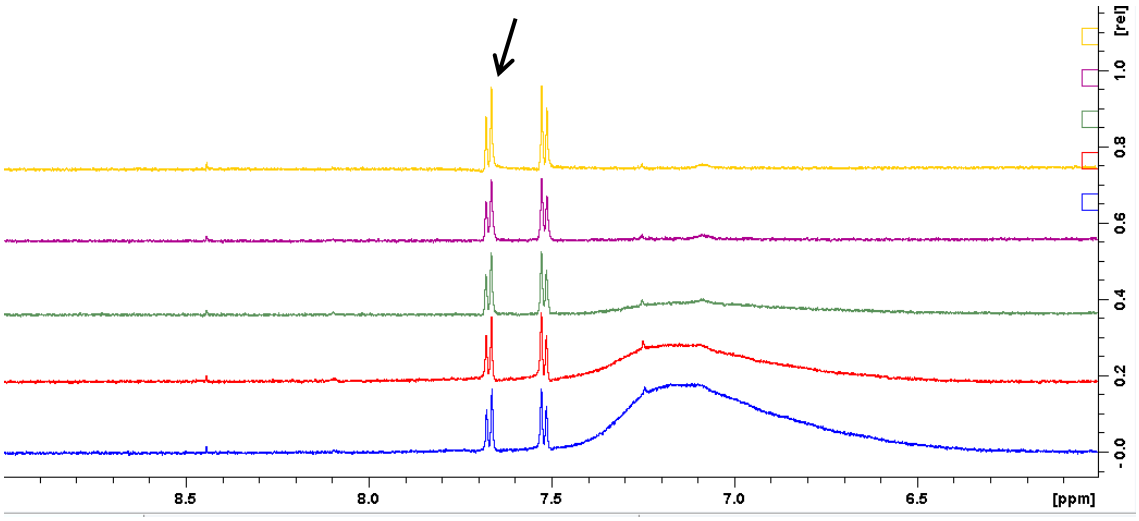

Figure 34: *^{1}H 1D NMR spectra stack plot for DMPC [SMALPs]/ [Compound **1**]*

The NMR stack plots coincided with the graphs, displaying that the addition of the SMALPs with compound **1** has less self-association than with other compounds studied. Further studies would include increasing the concentration of SMALPs added.

3.9.3. NMR ^{1}H 1D DMPC and *E.coli* [SMALPs]/ [Compound 2]

The next set of titration results were the change in intensity against the molar ratio of DMPC and *E.coli* [SMALPs]/[Compound **2**], (Figure 35) The first point on the graph represents ^{1}H 1D NMR data of the SSA in its free unbound state, the same as in **3.9.2**. The plotted graph shows successfully binding to the SMALPs; this was confirmed through the decrease in intensity %, which is a direct effect of the SSA being in a bound state and no longer detectable by NMR, hence only the free unbound SSA is detectable.

As expected the drop in intensity was greater for *E.coli* than for DMPC SMALPs, this was seen with the plotted data. In this experiment the same SSA and the same SMA copolymer was present. The only different components were the phospholipids. This indicates that the difference in intensity % is directly related to the electrostatic

interactions. More precisely the hindered hydrogen bonding, between the SSA and the PC lipids due to three methyl groups present that sterically hinders the electrostatic interactions, as discussed in **3.9.1.** See Figure 36, ^{1}H 1D NMR graph for clarification of the lower value molar ratios [SMALPs]/[Compound **2**] which displayed the same trend at the lower molar ratio.

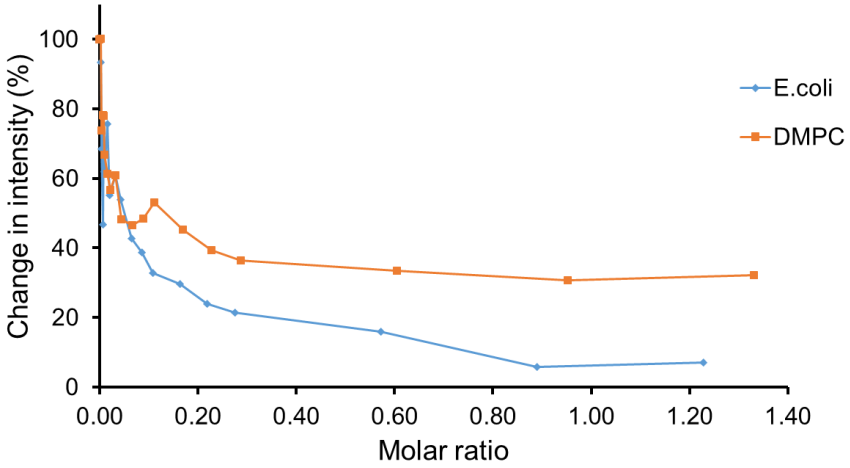

***Figure 35**: ^{1}H 1D NMR results for DMPC and E.coli [SMALPs]/ [Compound **2**]*

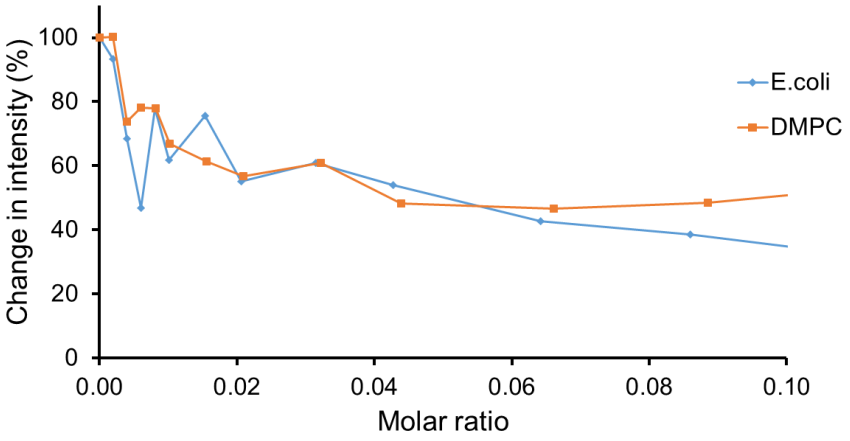

***Figure 36**: ^{1}H 1D NMR results for DMPC and E.coli [SMALPs]/ [Compound **2**] zoomed in.*

NMR spectra stack plot for *E.coli* [SMALPs]/ [Compound **2**] (Figure 37) arrow indicates peak observed at 7.9684 ppm and DMPC [SMALPs]/ [Compound **2**] (Figure 38) arrow indicates peak observed at 7.9727 ppm. The concentrations of the molar ratios applied

in the stack plots can be found in Table 2 in section **3.9.2**. Full set of measurements and ^{1}H 1D NMR Spectra for compound **2** (100 μM**)** are located in the appendices.

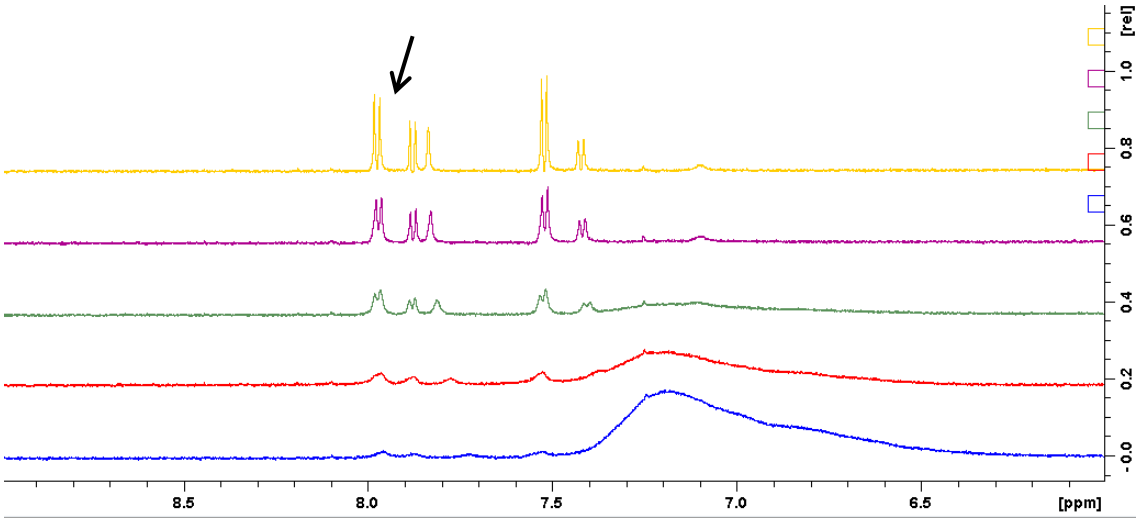

Figure 37: *^{1}H 1D NMR spectra stack plot for E.coli [SMALPs]/ [Compound **2**]*

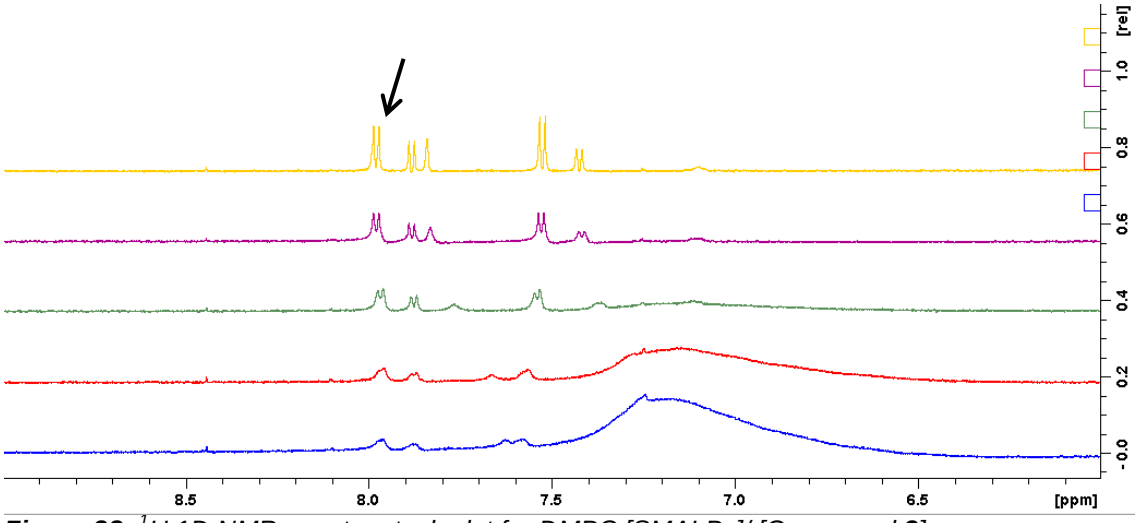

Figure 38: *^{1}H 1D NMR spectra stack plot for DMPC [SMALPs]/ [Compound **2**]*

The NMR stack plots coincide with the graphs, displaying the addition of the SMALPs with compound **2**. Here self-association can be seen with the peaks becoming broader, indicating the nanodiscs were binding to the compound.

3.9.4. NMR ^{1}H 1D DMPC and *E.coli* [SMALPs]/ [Compound 3]

The last set of ^{1}H 1D titration results was the change in intensity against the molar ratio of DMPC and *E.coli* [SMALPs]/ [Compound **3**] (Figure 39). The first point on the graph represents ^{1}H 1D NMR data of the SSA in a free unbound state, the same as in **3**.**9.2**.

The graph shows a clear difference in the binding associations, between the two types of SMALPs. These results were as expected with the drop in intensity % was greater for *E.coli* than for DMPC SMALPs, as can be seen with the plotted data. Similar results were seen and discussed in **3**.**9.3** with compound **2,** however, it's noted that the drop in intensity % was considerably less, than the previous results with compound **2**, indicating less electrostatic interactions between the SSA-SMALPs. See Figure 40 for ^{1}H 1D NMR graph for clarification of the lower value molar ratios [SMALPs]/ [Compound **3**] which displayed the same trend.

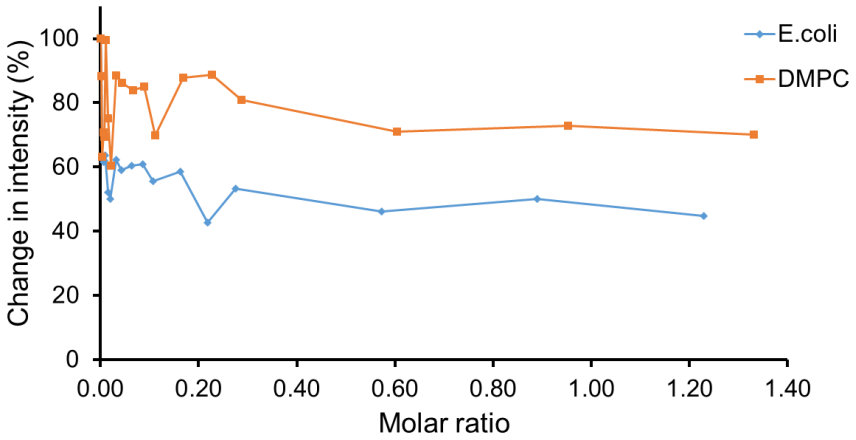

***Figure 39**: 1H 1D NMR results for DMPC and E.coli [SMALPs]/ [Compound **3**]*

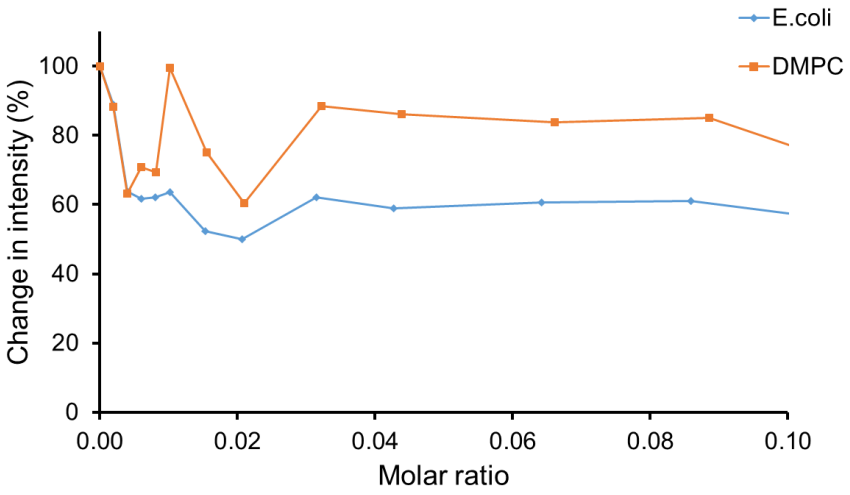

***Figure 40**: ^{1}H 1D NMR results for DMPC and E.coli [SMALPs]/ [Compound **3**] zoomed in*

NMR spectra stack plot for *E.coli* [SMALPs]/ [Compound **3**] (Figure 41) arrow indicates peak observed at 8.1372 ppm and DMPC [SMALPs]/ [Compound **3**] (Figure 42) arrow indicates peak observed at 8.1369 ppm. The concentrations of the molar ratios applied in the stack plots can be found in Table 2 in section **3.9.2**. Full set of measurements and ^{1}H 1D NMR Spectra for compound **3** (100 μM**)** are located in the appendices.

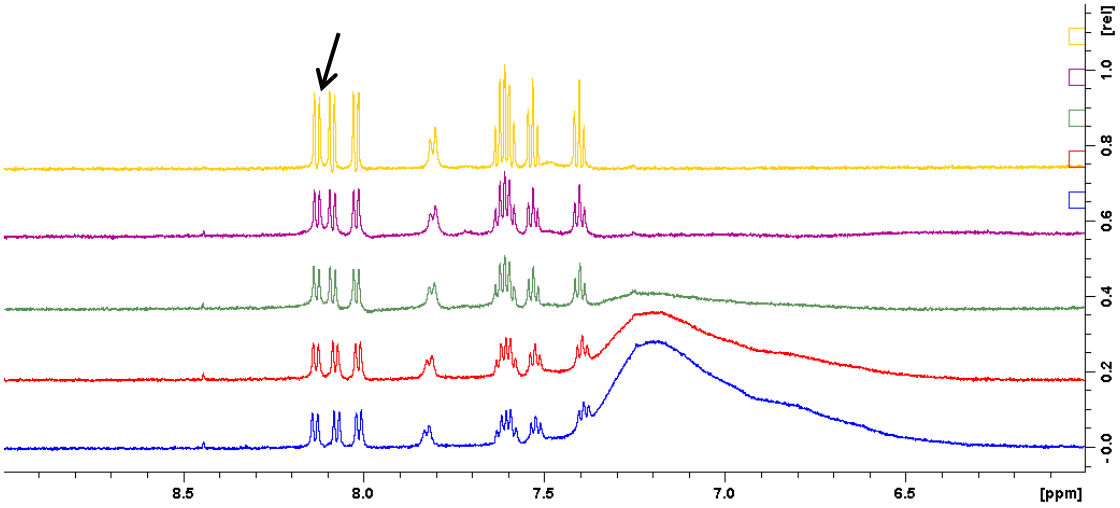

***Figure 41:** ^{1}H 1D NMR spectra stack plot for E.coli [SMALPs]/ [Compound **3**]*

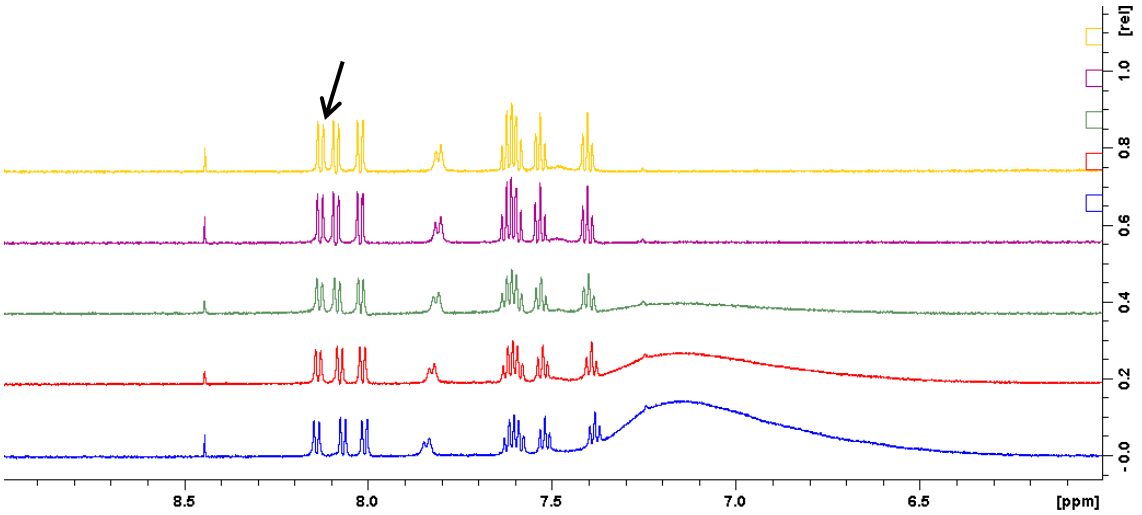

Figure 42: *^{1}H 1D NMR spectra stack plot for DMPC [SMALPs]/ [Compound **3**]*

The NMR stack plots coincided with the graphs, displaying the addition of the SMALPs with compound **3**. Here self-association can be seen with the peaks becoming smaller, indicating the nanodiscs were binding to the compound, resulting in less free SSA being detected.

3.9.5. NMR ^{1}H 1D *E.coli* SMALPs [SMALPs]/ [Compound (1) (2) (3)]

The next set of results was a comparison with *E.coli* SMALPs against compounds **1-3**, from the titrations in **3.9.2-3.9.4.** These were compared to determine how the different SSAs bind with a bacterial membrane.

The results in the graph, (Figure 43) display the change in intensity % for each compound when interacting with the SMALP. All of the SSAs had a change in peak intensity from the NMR spectra. This peak reduction and broadening, indicates electrostatic binding interactions. Compound **1,** had the least amount of change in intensity %, up to ~20% drop, compound **2,** displayed the greatest decrease in intensity with a decrease of around 95%, and compound **3,** had a change in intensity % up to 60% drop. The differences between compounds **2-3** were as expected, due to the 2-phenylbenzo[d]thiazole on **3** in the ortho position**,** hindering the HBA/HBD groups between the urea and the phosphate. In **2** the 2-phenylbenzo[d]thiazole is in the para

position, allowing for unhindered HBA/HBD interactions. Finally **1,** has a trifluoromethyl in the para position, this compound was expected to display similar associations as **2** with unhindered HAD/HBD. However this data indicates that the trifluoromethyl did not contribute to SSA-SMALP binding, in the same way as 2-phenylbenzo[d]thiazole. See Figure 44, ^{1}H 1D NMR graph for clarification of the lower value molar ratios *E.coli* [SMALPs]/ [Compound (**1**) (**2**) (**3**)] which displayed the same trend.

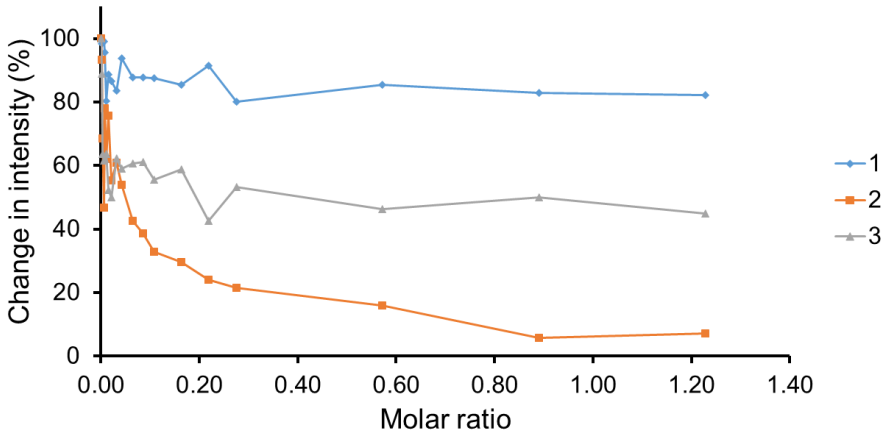

Figure 43: *^{1}H 1D NMR results for E.coli [SMALPs]/ [Compound (**1**) (**2**) (**3**)]*

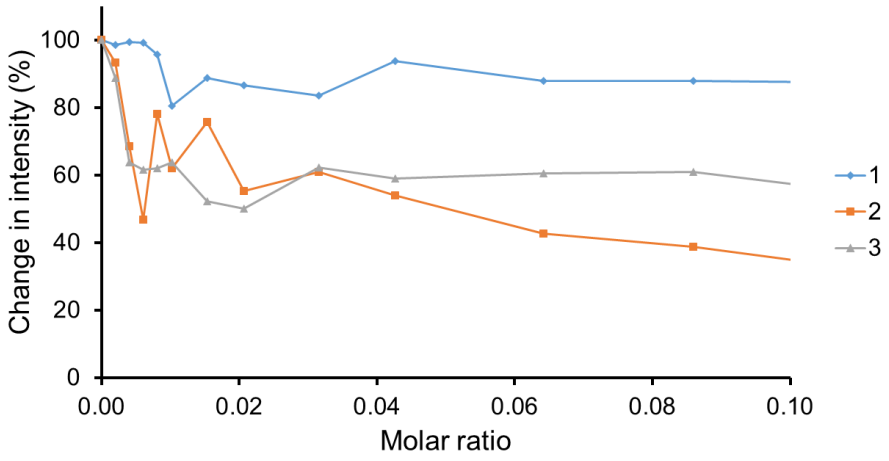

Figure 44*: ^{1}H 1D NMR results for E.coli [SMALPs]/ [Compound (**1**) (**2**) (**3**)] zoomed in*

3.9.6. NMR ^{1}H 1D DMPC [SMALPs]/ [Compound (1) (2) (3)]

The next set of results was a comparison with DMPC SMALPs against compounds **1-3**, from the titrations in **3.9.2-3.9.4.** These were compared to determine how the different SSAs bind with a mammalian membrane. The results in the graph, (Figure 45) display the change in intensity for each compound when interacting with the SMALP. All of the SSAs had a change in intensity with a similar pattern to the results discussed in **3.9.5,** however these decreases in intensity, were not as high as the ones with *E.coli* SMALPs due to hindered interactions of the PC phospholipid headgroup, as previously discussed.

Compound **1,** has the least amount of change in intensity of ~20%, compound **2,** displayed the greatest decrease in intensity with a decrease of around 70%, and compound **3,** has a change in intensity of ~30%. The difference in results between **1-3**, follows the same trend as in **3.9.5** and has been previously discussed.

See, Figure 46, ^{1}H 1D NMR graph for clarification of the lower value molar ratios DMPC [SMALPs]/[Compound (**1**)(**2**)(**3**)] which shows that **1** and **3** had a similar decrease in intensity, indicating higher concentration of SMALPs may have been needed to establish the differences in binding.

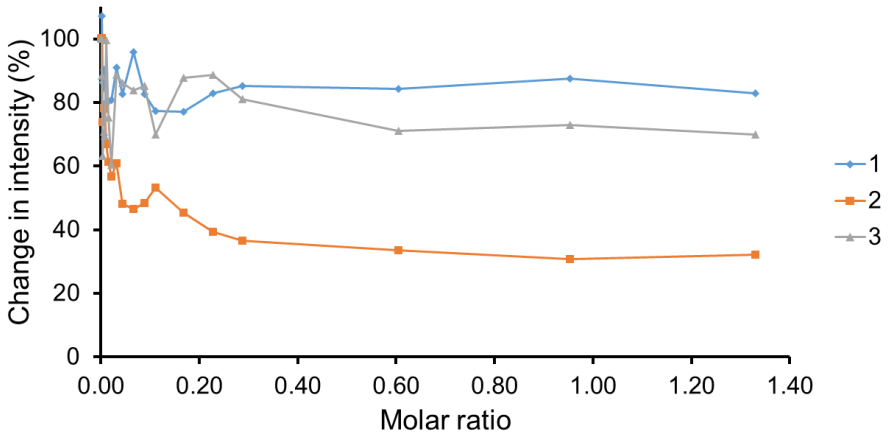

***Figure 45**:^{1}H 1D NMR results for DMPC [SMALPs]/ [Compound (**1**) (**2**) (**3**)]*

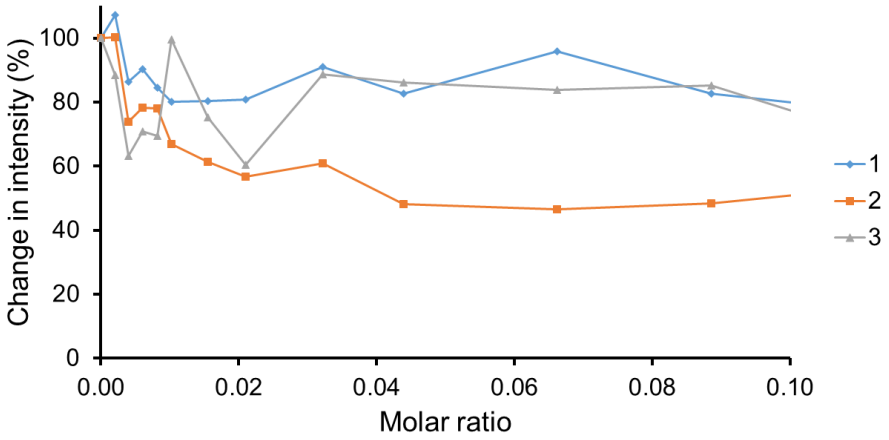

***Figure 46**: [1]H 1D NMR results for DMPC [SMALPs]/ [Compound (**1**) (**2**) (**3**)] zoomed in*

3.9.7. NMR ^{1}H CPMG DMPC and *E.coli* [SMALPs]/ [Compound 1]

The last experiment was CPMG NMR, with the aim to further investigate the interactions of **1-3**, with phospholipid nanodiscs. With CPMG NMR the spin-spin T_2 relaxation time is measured and applied to a series of spin-echo pulse elements. The T_2 relaxation is caused by transient magnetic fields due to molecular motion. This detects the interactions of the ligand with the nanodisc, these interactions cause de-phasing as the protons can no longer be completely refocused. This decay in signal indicates successful ligand binding interactions. In practice, a CPMG spectrum of the SSA sample was taken and compared to the CPMG spectrum of the ligand with the SMALPs sample. The more the signal decays the more the compound-SMALP interactions were occurring. This was indicated by broadening and reduction in the peak signals.[68,69]

To determine the interactions of the SSA to the SMALPs, the aromatic peaks of the compounds from the NMR spectra were selected, and monitored for peak reduction, for reasons previously discussed. This indicates that the SSA was interacting with the nanodiscs, similar to the ^{1}H NMR experiments. However this experiment was different as the peak reduction on the NMR spectra relates to all of the SSA that has interacted with the SMALP, and not just the bound in real time. This was measured through the

change in T_2 relaxation time, which is a result from successful binding within the sample.[68]

All of the results for ^{1}H CPMG NMR comparison show the change in intensity % for compound **1-3** (host) at 100 µM, the concentration of SMALPs (guest) was increased the data was represented as a molar ratio [SMALPs]/[Compound **1-3**] PB/5 % D_20 solution (298 K). Tables with the full sets of the data collected for the CPMG NMR titration studies are located in the appendices.

The first set of CPMG results show the change in intensity % against the molar ratio of DMPC and *E.coli* [SMALPs]/ [Compound **1**], (Figure 47). The first point on the graph represents CPMG NMR data of the SSA with no SMALPs. The plotted graph shows successfull interactions with to the SMALPs; this was confirmed through the decrease in intensity. Here there was a clear difference in the interactions with the higher concentration of SMALPs, with the *E.coli* SMALPs interacting more than the DMPC SMALPs, as can be seen with the plotted data. On examination of the lower molar ratio there is little difference between the *E.coli* binding and the DMPC SMALPs, however the *E.coli* has a more consistent interactions with the compound. Graph ^{1}H CPMG NMR for clarification displaying the lower value molar ratios for [SMALPs]/ [Compound **1**] (Figure 48).

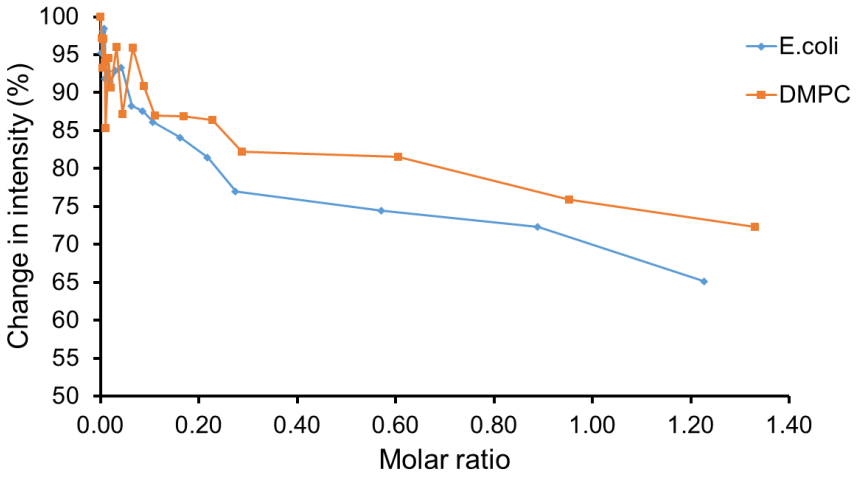

Figure 47: *^{1}H CPMG NMR results for DMPC and E.coli [SMALPs]/ [Compound **1**]*

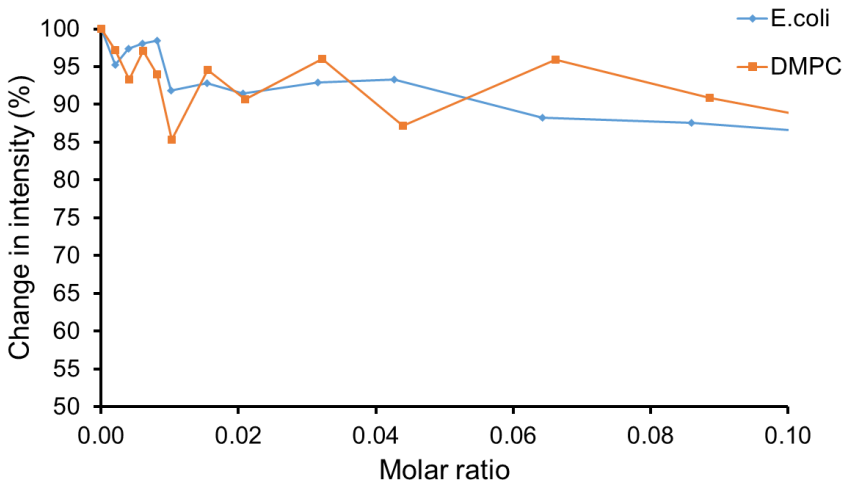

Figure 48: *^{1}H CPMG NMR results for DMPC and E.coli [SMALPs]/ [Compound **1**] Zoomed in*

NMR spectra stack plot for *E.coli* [SMALPs]/ [Compound **1**] (Figure 49) arrow indicating peak observed at 7.6698 ppm and DMPC [SMALPs]/ [Compound **1**] (Figure 50) arrow indicating peak observed at 7.6797 ppm. The concentrations of the molar ratios included in the stack plots were from 0 (yellow) to 1.229 (blue) for *E.coli* and 0 (yellow) to 1.330 (blue) for DMPC, full set of molar ratios included can be found in Table 2 in section **3.9.2**.

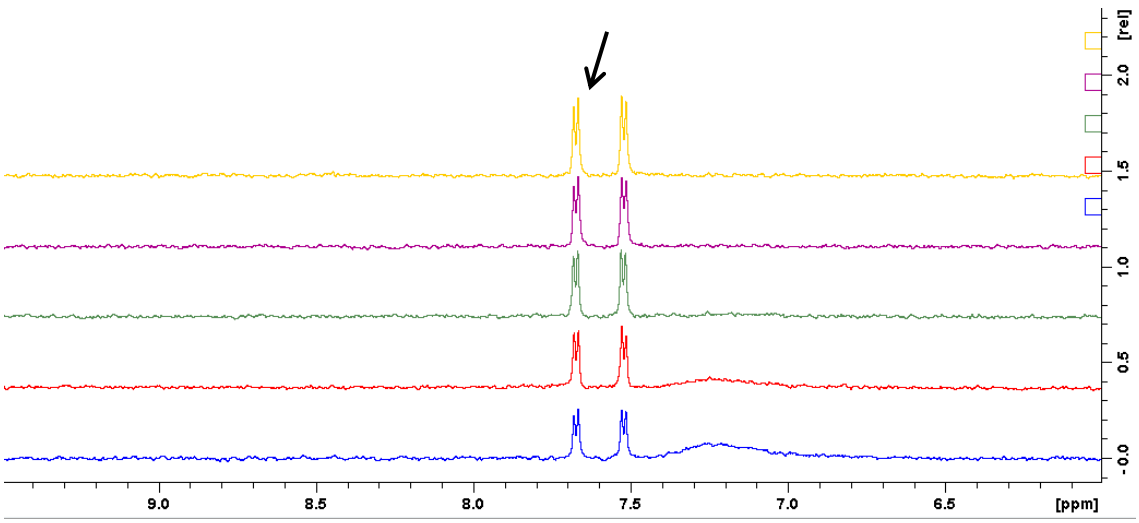

Figure 49: *CPMG NMR spectra stack plot for E.coli [SMALPs]/ [Compound **1**]*

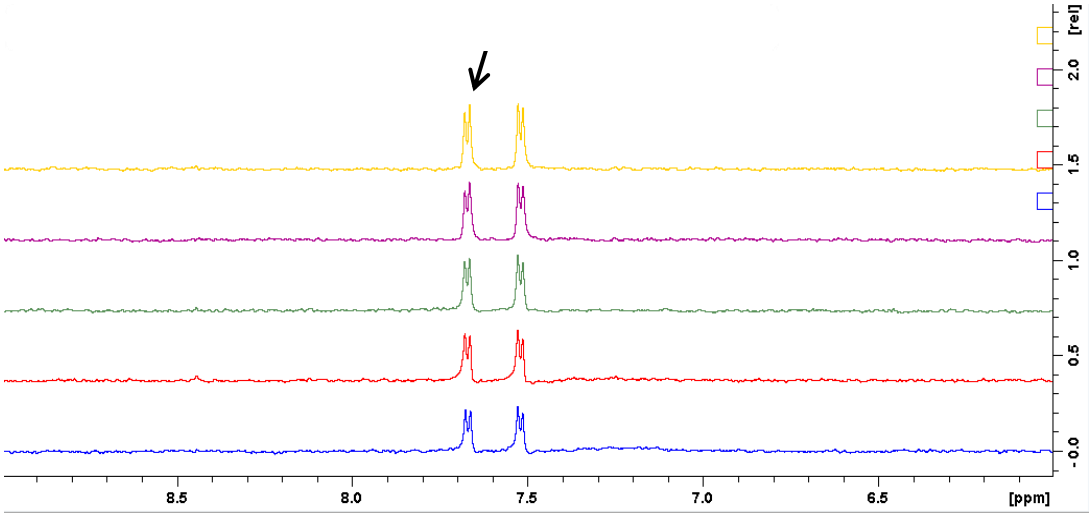

Figure 50: *CPMG NMR spectra stack plot for DPMC [SMALPs]/ [Compound **1**]*

The NMR stack plots coincide with the graphs, displaying the addition of the SMALPs with compound **1**. Here self-association can be seen with the peaks becoming smaller, indicating the nanodiscs were binding to the compound, resulting in a reduced amount SSA being detected.

3.9.8. NMR ^{1}H CPMG DMPC and *E- coli* [SMALPs]/ [Compound 2]

The next set of titration results were for ^{1}H CPMG NMR comparison showing the change in intensity for compound **2** (host) at 100 µM (Figure 51) The graph below shows that initially the differences in binding, was *E.coli* interacting and binding more than the DMPC SMALPs, but the PC SMALP intensity decreased much faster and with lower concentrations, of ~0.05 molar ratio. This represents that compound **2** was binding to SMALPs even at low concentrations leading to a rapid decay in the electromagnetic signal. These results were not coherent with the ^{1}H 1D NMR results discussed in **3.9.3** as in the previous studies, where the DMPC SMALP results continued to have a lower drop in intensity % than the *E.coli*, however this measured just the bound state resulting in broader peaks and the CPMG measured the T_2. Here the DMPC SMALPs have interacted with the SSA, however these electrostatic

interactions may be weaker binding than with *E.coli* SMALPs, further studies were needed.

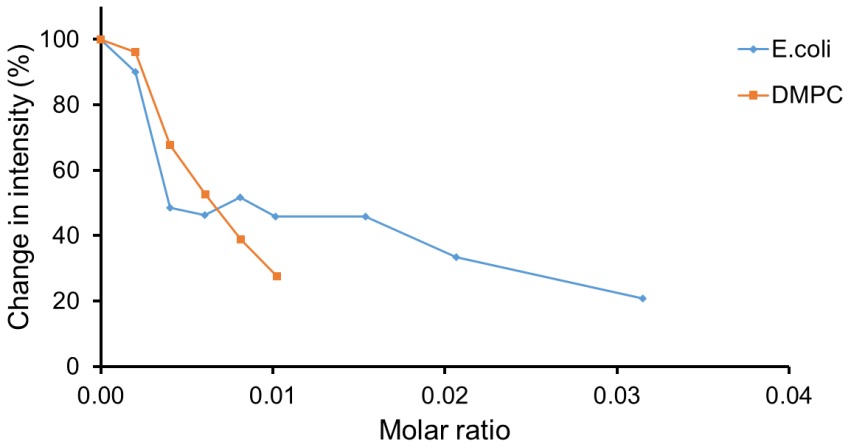

Figure 51: *^{1}H CPMG NMR results for DMPC and E.coli [SMALPs]/[Compound **2**]*

NMR spectra stack plot for *E.coli* [SMALPs]/ [Compound **2**] (Figure 52) arrow indicates peak observed at 7.961 ppm and DMPC [SMALPs]/ [Compound **2**] (Figure 50) arrow indicates peak observed at 7.9730 ppm.

The concentrations of the molar ratios included in the stack plots for compound **2,** are located in Table 3, the full set are located in the appendices.

Table 3: *Colour scheme for NMR CPMG stack plots with matching molar measurement for compound **2**.*

Colour	E.coli Molar ratio	DMPC Molar ratio
Yellow	0.000	0.000
Purple	0.004	0.004
Green	0.006	0.006
Red	0.010	0.010
Blue	0.015	0.016

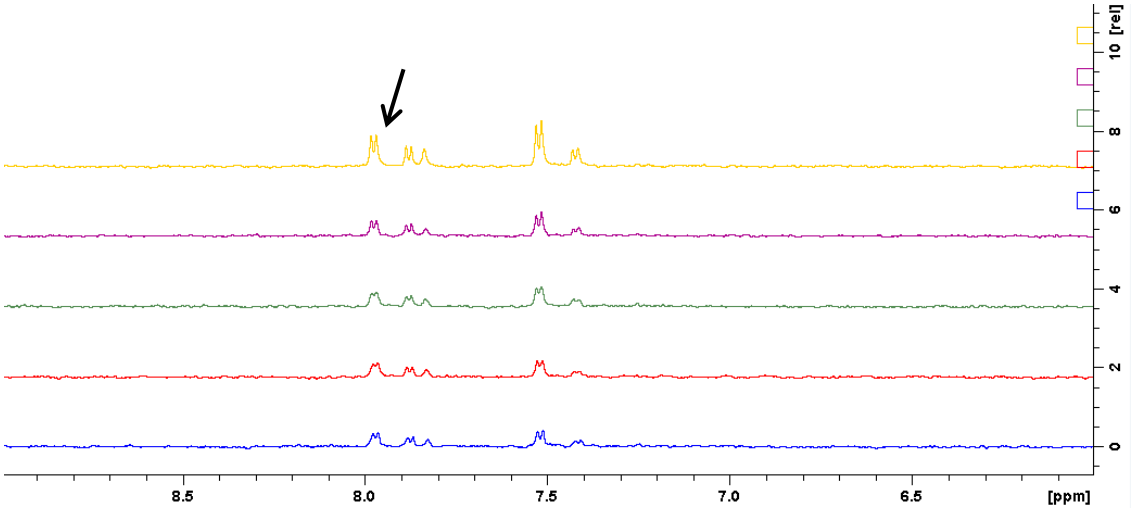

Figure 52: *CPMG NMR spectra stack plot for E.coli [SMALPs]/ [Compound **2**]*

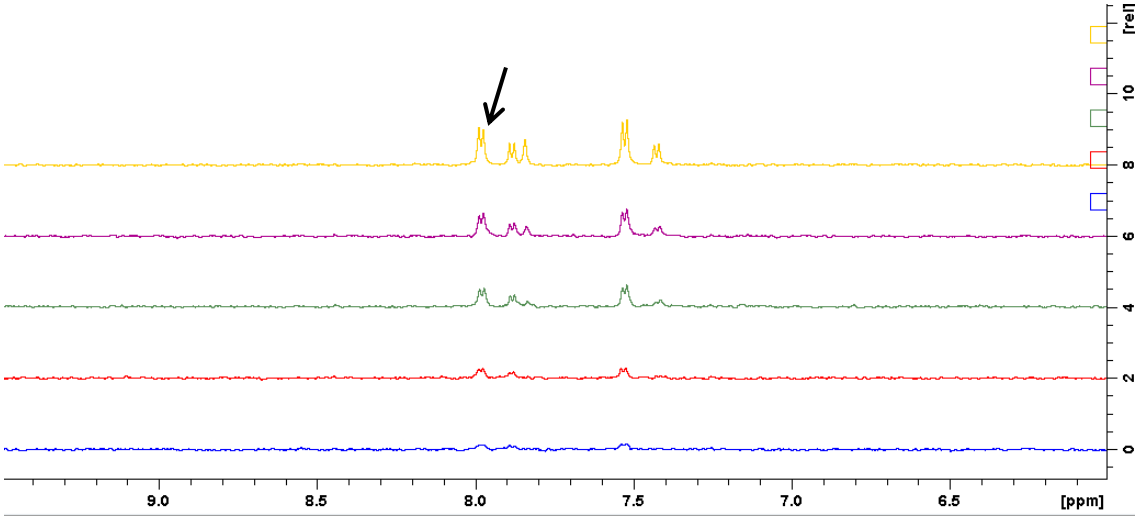

Figure 53: *CPMG NMR spectra stack plot for DPMC [SMALPs]/ [Compound **2**]*

The NMR stack plots coincided with the graphs, displaying the addition of the SMALPs with compound **2**. Here self-association was seen with the peaks becoming broader and less intense, indicating the nanodiscs were binding to the compound.

3.9.9. NMR ^{1}H CPMG DMPC and *E.coli* [SMALPs]/[Compound 3]

The last set of results for ^{1}H CPMG NMR were a comparison showing the change in intensity for compounds **3** (host) at 100 µM) (Figure 54)

The graph shows a clear difference in the interactions, between the two types of SMALPs, with an increased decay in the SSA peak intensity, when interacting with *E.coli*. These results were as expected with the drop in intensity, greater for *E.coli* than for DMPC SMALPs, as can be seen with the plotted data and were coherent with the ^{1}H 1D NMR results with **3**. How the compounds interact with the SMALP has been previously discussed with similar results **9.3-9.4.** See Figure 55, for 1H CPMG NMR graph for clarification of the lower value molar ratios [SMALPs]/[Compound **3**], which displayed the same trend.

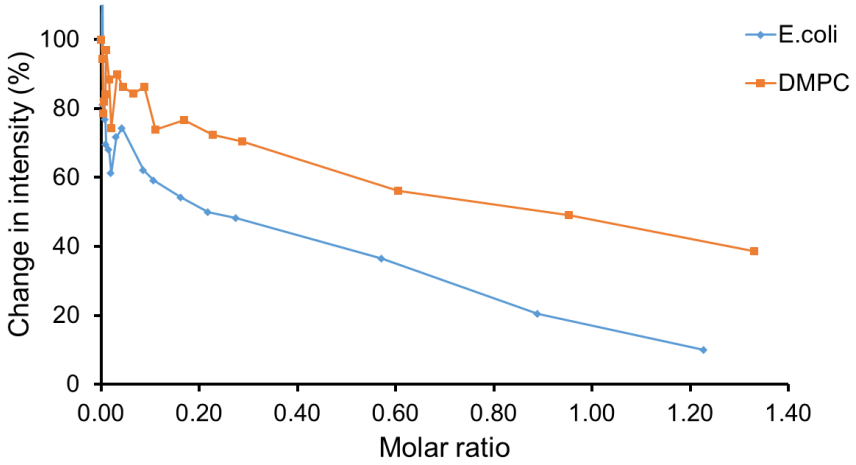

Figure 54: *^{1}H CPMG NMR results for DMPC and E.coli [SMALPs]/[Compound **3**]*

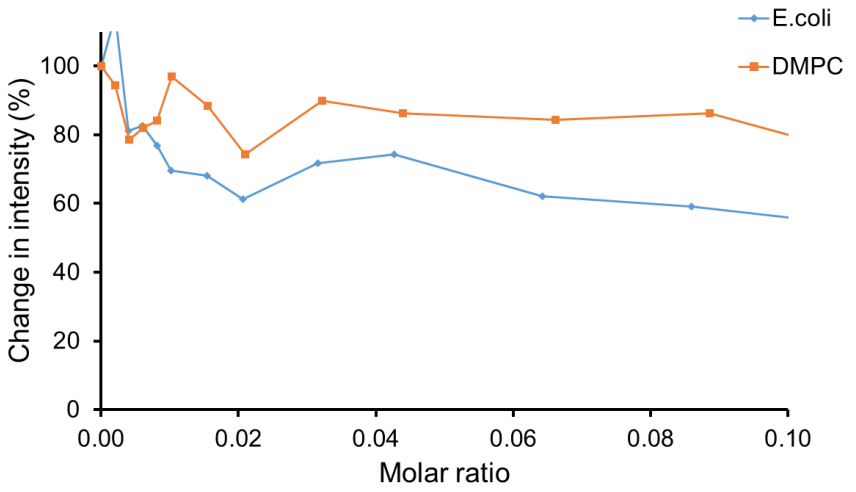

Figure 55: *^{1}H CPMG NMR results for DMPC and E.coli [SMALPs]/[Compound **3**] Zoomed in*

NMR spectra stack plot for *E.coli* [SMALPs]/ [Compound **3**] (Figure 56) arrow indicates the peak observed at 8.1372 ppm and DMPC [SMALPs]/ [Compound **3**] (Figure 57) arrow indicates the peak observed at 8.1369 ppm. The concentrations of the molar ratios included in the stack plots were from 0 (yellow) to 1.229 (blue) for *E.coli* and 0 (yellow) to 1.330 (blue) for DMPC, full set of molar ratios included can be located in Table 2 in section **3.9.2**.

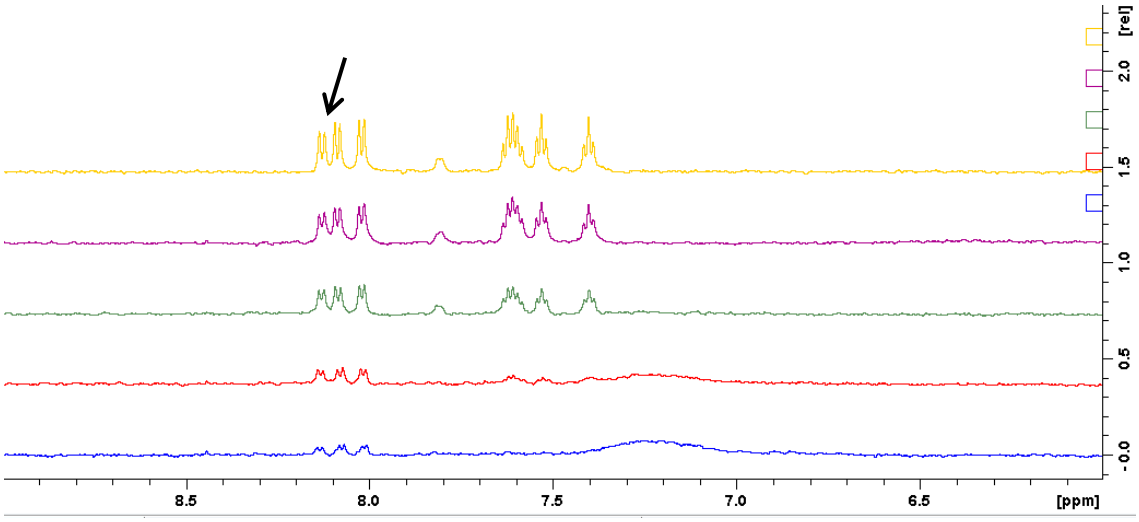

Figure 56: *CPMG NMR spectra stack plot for E.coli [SMALPs]/ [Compound **3**]*

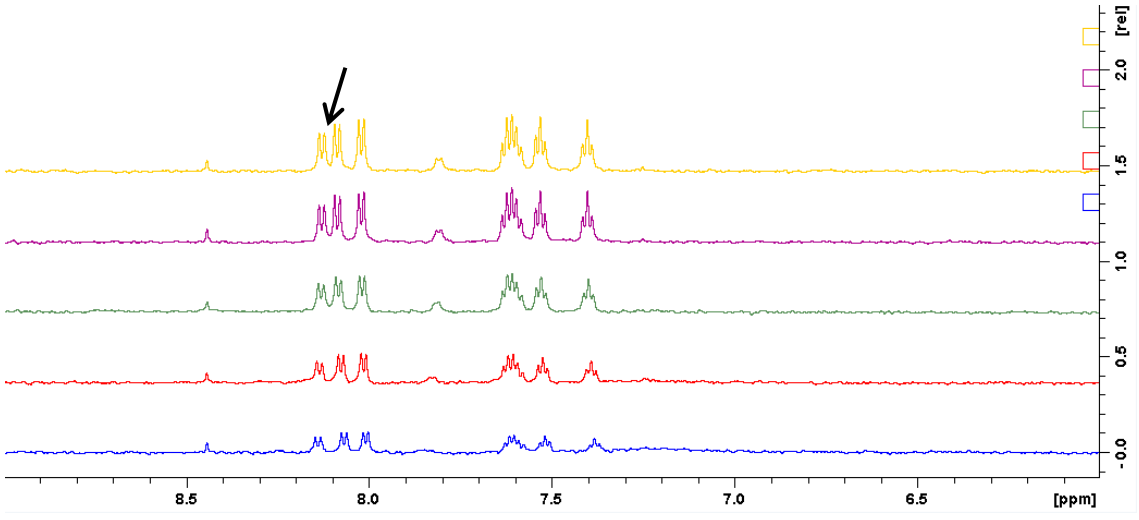

Figure 57: *CPMG NMR spectra stack plot for DPMC [SMALPs]/ [Compound **3**]*

The NMR stack plots coincided with the graphs, displaying the addition of the SMALPs with compound **3**. Here self-association was seen with the peaks becoming broader, indicating the nanodiscs were binding to the compound, with the *E.coli*: compound **3,** the peaks ~ 7.5 ppm became so broad they can no longer be detected.

3.9.10. NMR ^{1}H CPMG *E.coli* SMALPs [SMALPs]/[Compound (1)(2)(3)]

The next set of results displays a comparison with *E.coli* SMALPs against compounds **1-3**, from the titrations in **3.9.7-3.9.9**. These were compared to determine how the different SSAs bind with a bacterial membrane.

The results in the graph, (Figure 58) display the change in intensity for each compound when interacting with the SMALP. All of the SSAs had a change in peak intensity from the NMR spectra. This peak reduction and broadening, indicates electrostatic interactions and self-associations between the SSA and SMALPs. Compound **1**, has the least amount of change in intensity % of ~ 40%, compound **2**, displayed a rapid decay of the signal, indicating binding and the formation of supramolecular complexes. Compound **3**, had a change in intensity % of ~95%. The differences between compounds **2-3** were as expected, and were coherent with the ^{1}H 1D NMR data, in **3.9.6** how the compounds interacted with the SMALPs has been previously discussed with similar results **3.9.3-3.9.4.** See Figure 59, for ^{1}H CPMG NMR graph for clarification of the lower value molar ratios [SMALPs]/[Compound (**1**)(**2**)(**3**)].

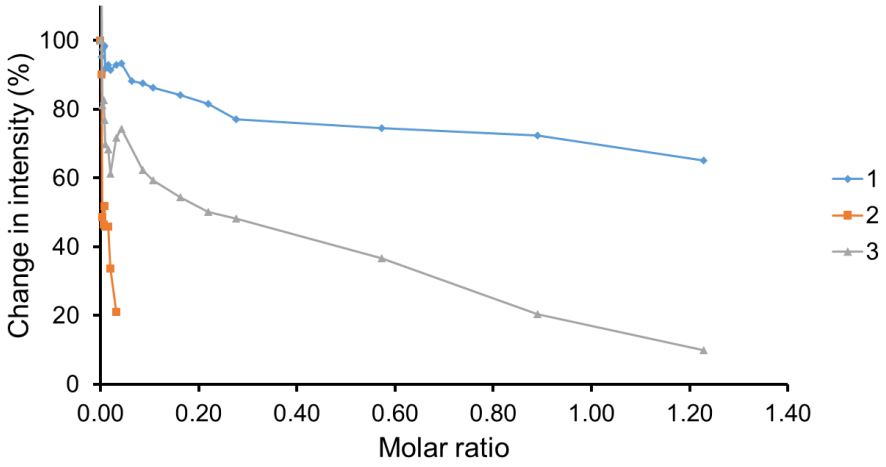

Figure 58: *^{1}H CPMG NMR results for E.coli [SMALPs]/[Compound (**1**)(**2**)(**3**)]*

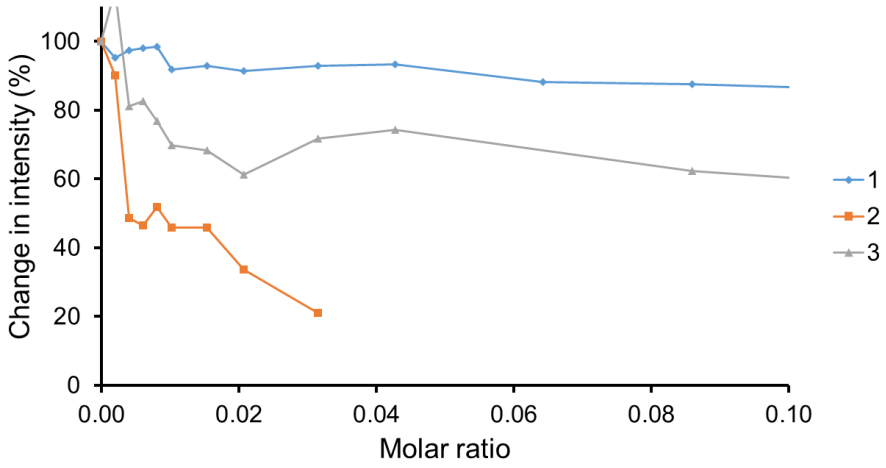

Figure 59*: ^{1}H CPMG NMR results for E.coli [SMALPs]/[Compound (**1**)(**2**)(**3**)]Zoomed in*

3.9.11. NMR ^{1}H CPMG DMPC [SMALPs]/[Compound (1)(2)(3)]

The last comparison was results for ^{1}H CPMG NMR showing the change in intensity for each compound **1-3,** against PC SMALPs from the titrations in **3.9.7-3.9.9.**

The results in the graph (Figure 60) show a clear difference in the interactions between the compounds, with compound **2**, showing a larger decrease in intensity %. These results follow trend with the results in **3.9.10,** however in this set of results the change

in intensity % was smaller than with the *E.coli* results. This was expected and coherent with the rest of the NMR analysis within this study. How the molecular structures, influence the interactions has been previously discussed in **3**.**9.5**. See Figure 61, for ^{1}H CPMG NMR graph for clarification of the lower value molar ratios [SMALPs]/[Compound (**1**)(**2**)(**3**)].

NMR results were coherent with this hypothesis as the results for both the ^{1}H CPMG and ^{1}H 1D, exhibit a more interactions towards the *E.coli* SMALPs when compared to the binding with the DMPC SMALPs with compound **2**-**3**. The only exception was NMR ^{1}H 1D with compound **1**, where the binding appeared to be similar, however this was an anomaly when compared to the rest of the data. Further investigation was needed at higher concentrations and/or more scans to improve the signal to noise ratio to determine the HBD and HDA binding modes in more depth.

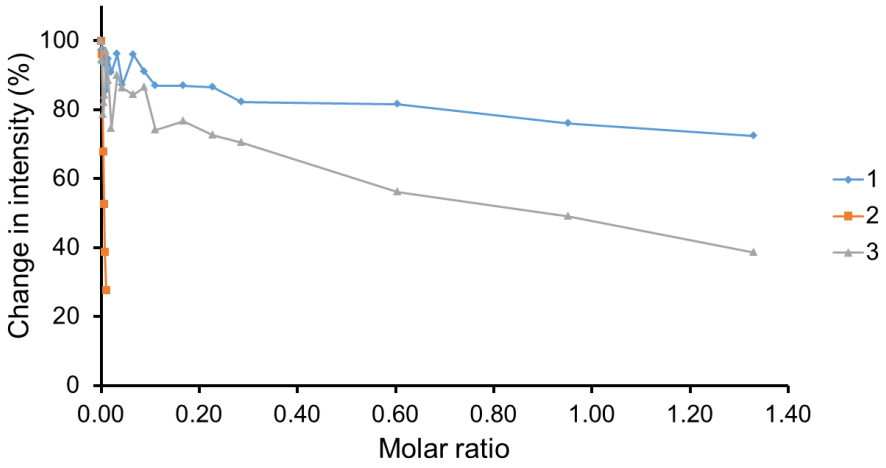

Figure 60: *^{1}H CPMG NMR results for DMPC [SMALPs]/[Compound (**1**)(**2**)(**3**)]*

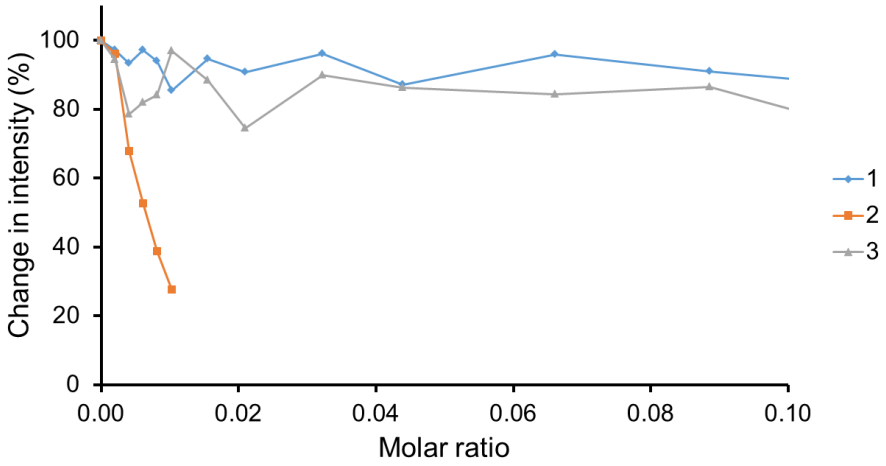

Figure 61: *^{1}H CPMG NMR results for DMPC [SMALPs]/[Compound (**1**)(**2**)(**3**)] zoomed in*

3.9.12. Secondary binding modes

The NMR titration results displayed that some of the plotted intensity results were non-uniform, and did not always follow trend. This could be due to many factors, the simplest one could be a mixing error, or the sample may have needed more time to equilibrate, as no extra time was given, however this can have repercussions as the compounds antimicrobial activity may be time dependant, leading to a sample with only the compound and disassembled nanodiscs. The non-uniform data may also have been improved by analysing the average of more than just one aromatic peak, again further studies were needed.

A hypothesis for the non-uniform intensity results can be due to multiple interactions with secondary hydrogen binding sites of the SMALPs. The secondary site includes the hydrogen bond donating of the urea moiety of the compound.

An example of this is with the PE SMALPs, where adding the SMALPs to the compound; the sulfonate moiety will primarily bind to the amine. Once most of the primary binding sites are full, causing complete saturation of the binding site, [38] then the compound will start to bind in other places. These include HBD/HBA interactions with the urea moiety and phosphate as seen in Figure 29. These contribute towards the

secondary weaker binding sites. With the addition of more SMALPs the compound will be attracted to the new primary binding sites and will momentarily be free in solution, resulting in non-uniform data with an increase in intensity.

The PC SMALPs with the amphiphilic compounds also exhibit some non-uniform data, this can be attributed to other non-covalent bond interactions which have been described in literature and include electrostatics, π−π stacking, charge transfer and hydrogen bond interactions.[70] These interactions not only occur with the compound-SMALP binding but also with compound self-association.

3.9.13. SSA structure-activity

In the literature previous studies with self-associating amphiphiles have revealed that changing compound composition affects antimicrobial action. All of the self-associating molecules in this study, were synthesised from the same general structure as seen in the literature, with urea oxygen in the hydrophobic region, sulfonate in the hydrophilic region and with TBA as a counter cation. Keeping these functionalities the same focused this study on the modifications of the constituents attached to the benzene ring only. Compound **2** and compound **3** with 2-phenylbenzo[d]thiazole displayed more interactions towards the *E.coli* SMALPs, the position of this R group played an important role, with the 2-phenylbenzo[d]thiazole in the para position resulted in enhanced activity when compared to the ortho position. This change in activity is directly related to the 2-phenylbenzo[d]thiazole hindering the hydrogen bond donating functionality of the urea oxygen when in the ortho position. This reveals that urea is vital for hydrogen bonding and therefore vital for antimicrobial activity.

When comparing selectivity towards the bacterial membranes and mammalian membranes, the results have shown that the compounds will interact and accumulate on the surface with the bacterial membranes more intensely than the mammalian membranes. This was seen through the ^{1}H 1D NMR studies, where nearly all of the compounds displayed a greater change in intensity with *E.coli* SMALPs, indicating that

the compounds were binding to the SMALP. These compounds will also aggregate on the surface of the *E.coli* SMALP due to their self-associating properties; this was observed with similar self-associating molecules in literature, where they found that self-associated structures is imperative for effective drug delivery to the bacterial cell.[56]

The ^{1}H CPMG results displayed the same pattern as the ^{1}H 1D study, with the broadening and reduction in the intensity of the signals, with increasing SMALP to compound interactions. The resulting peaks in this experiment were much smaller than with the ^{1}H 1D study, this was due to the signal decay upon the interaction of the SMALPs with the compound. [68]

The PC SMALPs resulted in fewer binding interactions, which as previously mentioned may be due to electrostatic interactions other than the phospholipids headgroup with the sulfonate. This was not favourable due to the three methyl groups attached to the amine, leading to electrostatic hindrance. However weaker binding interactions were still observed, these are thought to be insufficient to disrupt the structure of the mammalian membranes.

4. Overall Conclusions

In conclusion, this preliminary research investigated the binding interactions between supramolecular self-associating molecules, and the cell membrane. The model membranes were formed with a SMA co-polymer that solubilises a patch of phospholipid bilayers in to nanodiscs. This allowed for the formation of nanodiscs with different lipid compositions, mimicking the bacterial cells and mammalian cells. The nanodiscs were characterised through DLS, TEM and quantified. The binding associations between three self-associating compounds and the model membranes were investigated through ^{1}H 1D and CPMG NMR analysis. The results indicate that the compounds structure affects the binding with the nanodiscs. The compounds were all identical with the same HBD/HBA functionalities, with the only one different constituent attached to a benzene ring. This verified that the change in binding observed towards the model membranes was a direct result of the constituent. The position of the constituent affected the hydrogen bonding, thus affecting its antimicrobial properties. The results reveal that that the all three compounds exhibit selective binding towards *E.coli*, when compared to the binding of mammalian cells. This shows potential for their use as future antimicrobial agents, aiding in the fight against antimicrobial resistance.

Further work

In this study only three compounds were investigated, which form part of a family of over 65 molecules. Further work would include the binding studies with other amphiphilic compounds against *E.coli* and against other bacterial strains. Further work with the compounds presented in this study would include fluorescence anisotropy binding studies, on the fluorescent molecules compound **2** and compound **3** and confocal microscopy to visualise the compounds interacting with the nanodiscs, which will help determine if the compounds are bacteriostatic or bactericidal. Both of these methods of investigation were initialised but due to time constraints were not realised.

5. References

1 Antimicrobial Resistance: Global Report on Surveillance, https://apps.who.int/iris/bitstream/handle/10665/112642/9789241564748_eng.pdf, (accessed 22 July 2019).

2 J. O. ' Neill, Antimicrobial Resistance: Tackling a crisis for the health and wealth of nations The Review on Antimicrobial Resistance Chaired, https://amr-review.org/sites/default/files/AMR Review Paper - Tackling a crisis for the health and wealth of nations_1.pdf, (accessed 24 July 2019).

3 B. L. Ligon, *Semin. Pediatr. Infect. Dis.*, 2004, **15**, 58–64. DOI 10.1053/J.SPID.2004.02.002

4 P. Aggleton, A. Broom and J. Moss, *Practical justice: Principles, practice and social change*, Routledge, 2019, DOI 10.4324/9781351010498

5 A. G. Mainous III, C. Pomeroy, T. S. Stalder and L. C. Preheim, in *Management of Antimicrobials in Infectious Diseases*, 2003, pp. 29–41, DOI: 10.1385/1-59259-036-5:29.

6 T. J. Beveridge, *Biotech. Histochem.*, 2001, **76**, 111–118, DOI:10.1080/bih.76.3.111.118

7 T. J. Silhavy, D. Kahne and S. Walker, *Cold Spring Harb. Perspect. Biol.*, 2010, **2**, DOI: 10.1101/cshperspect.a000414.

8 W. Keenleyside, 3.3: Unique Characteristics of Prokaryotic Cells - Biology LibreTexts, https://bio.libretexts.org/TextMaps/Microbiology/Book%3A_Microbiology_(OpenStax)/03%3A_The_Cell/3.3%3A_Unique_Characteristics_of_Prokaryotic_Cells, (accessed 24 July 2019).

9 G. Ramachandran, *Virulence*, 2014, **5**, 213–218, DOI: 10.4161/viru.27024.

10 A. Mahamoud, J. Chevalier, S. Alibert-Franco, W. V. Kern and J. M. Pagès, *J. Antimicrob. Chemother.*, 2007, **59**, 1223–1229, DOI: 10.1093/jac/dkl493

11 H. Watson, *Essays Biochem.*, 2015, **59**, 43–70, DOI: 10.1042/BSE0590043.

12 J. J. Koh, H. Zou, S. Lin, H. Lin, R. T. Soh, F. H. Lim, W. L. Koh, J. Li, R. Lakshminarayanan, C. Verma, D. T. H. Tan, D. Cao, R. W. Beuerman and S. Liu, *J. Med. Chem.*, 2016, **59**, 171–193, DOI: 10.1021/acs.jmedchem.5b01500.

13 S. Mashaghi, T. Jadidi, G. Koenderink and A. Mashaghi, *Int. J. Mol. Sci.*, 2013, **14**, 4242–4282, DOi: 10.3390/ijms14024242.

14 G. Yu, K. Jie and F. Huang, *Chem. Rev.*, 2015, **115**, 7240–7303, DOI: 10.1021/cr5005315.

15 C. Osman, D. R. Voelker and T. Langer, *J. Cell Biol.*, 2011, **192**, 7–16 ,DOI: 10.1083/jcb.201006159.

16 M. Aktas, L. Danne, P. Moller and F. Narberhaus, *Front. Plant Sci.*,2018, DOI:10.3389/fpls.2014.00109.

17 J. N. van der Veen, J. P. Kennelly, S. Wan, J. E. Vance, D. E. Vance and R. L. Jacobs, *Biochim. Biophys. Acta - Biomembr.*, 2017, **1859**, 1558–1572, DOI: 10.1016/j.bbamem.2017.04.006.

18 H. I. Ingoífsson, M. N. Melo, F. J. Van Eerden, C. Clément Arnarez, C. A. Lopez, T. A. Wassenaar, X. Periole, A. H. De Vries, D. Peter and S. J. Marrink, 2014 , DOI:10.1021/ja507832e.

19 A. I. P. M. de Kroon, P. J. Rijken and C. H. De Smet, *Prog. Lipid Res.*, 2013, **52**, 374–394, DOI: 10.1016/j.plipres.2013.04.006.

20 O. Geiger, I. M. López-Lara and C. Sohlenkamp, *Biochim. Biophys. Acta - Mol. Cell Biol. Lipids*, 2013, **1831**, 503–513, DOI: 10.1016/j.bbalip.2012.08.009.

21 R. M. Epand and R. F. Epand, *Biochim. Biophys. Acta - Biomembr.*, 2009, **1788**, 289–294, DOI: 10.1016/j.bbamem.2008.08.023

22 E. Van Den Brink-Van Der Laan, J. Antoinette Killian and B. De Kruijff, *Biochim. Biophys. Acta - Biomembr.*, 2004, **1666**, 275–288, DOI: 10.1016/j.bbamem.2004.06.010.

23 P. R. Cullis, M. J. Hope and C. P. S. Tilcock, *Chem. Phys. Lipids*, 1986, **40**, 127–144, DOI: 10.1016/0009-3084(86)90067-8.

24 V. A. Frolov, A. V. Shnyrova and J. Zimmerberg, *Cold Spring Harb. Perspect. Biol.*, 2011, .DOI: 10.1101/cshperspect.a004747.

25 B. A. C. Horta, A. H. de Vries and P. H. Hünenberger, *J. Chem. Theory Comput.*, 2010, **6**, 2488–2500, DOI: 10.1021/ct100200w

26 D. G. Waller and A. P. Sampson, in *Medical Pharmacology and Therapeutics*, Elsevier, 2018, 581–629, DOI: 10.1016/b978-0-7020-7167-6.00051-8.

27 C. R. Bourne, *Antibiot. (Basel, Switzerland)*, 2014, **3**, 1–28, DOI: 10.3390/antibiotics3010001.

28 A. Bermingham and J. P. Derrick, *BioEssays*, 2002, **24**, 637–648, DOI: 10.1002/bies.10114.

29 G. D. Wright, *Chem. Biol.*, 2012, **19**, 3–10, DOI: 10.1016/j.chembiol.2011.10.019

30 E. Sukkar, *Pharm. J.*, 2015 , DOI:10.1211/pj.2013.11130209.

31 bioMerieux | Superbugs: Evolution, Resistance & Impact on Health, http://www.myrolematters.com/superbugs.html, (accessed 22 July 2019).

32 S. Santajit and N. Indrawattana, *Biomed Res. Int.*, 2016, 1–8, DOI: 10.1155/2016/2475067.

33 WHO, *Global Action Plan on Antimicrobial Resistance. Geneva, WHO, 2015, 1-28. Availablefrom: http://www.wpro.who.int/entity/drug_resistance/resources/global_action_plan_eng.pdf*, 2015. (accessed 23 July 2019).

34 A. M. Seddon, P. Curnow and P. J. Booth, *Biochim. Biophys. Acta - Biomembr.*, 2004, **1666**, 105–117, DOI: 10.1016/j.bbamem.2004.04.011

35 T. K. Lind, H. Wacklin, J. Schiller, M. Moulin, M. Haertlein, T. G. Pomorski and M. Cárdenas ,2015, **10**, DOI:10.1371/journal.pone.0144671.

36 X. Wang, Z. Mu, Y. Li, Y. Bi and Y. Wang, *Protein J.*, 2015, **34**, 205–211, DOI: 10.1007/s10930-015-9613-2

37 A. Akbarzadeh, R. Rezaei-Sadabady, S. Davaran, S. W. Joo, N. Zarghami, Y. Hanifehpour, M. Samiei, M. Kouhi and K. Nejati-Koshki, *Nanoscale Res. Lett.*, 2013, **8**, DOI:10.1186/1556-276X-8-102.

38 A. H. Zhang, I. A. Edwards, B. P. Mishra, G. Sharma, M. D. Healy, A. G. Elliott, M. A. T. Blaskovich, M. A. Cooper, B. M. Collins, X. Jia and M. Mobli, *Front. Chem.*, 2019, DOI:10.3389/fchem.2019.00238.

39 S. Moon, B. Kong, Y. H. Jung, Y. Kim, S. Yu, J. bum Park, J. Shin and D. H. Kweon, *Process Biochem.*, 2018, **66**, 230–236, DOI: 10.1016/j.procbio.2017.12.005.

40 T. H. Bayburt and S. G. Sligar, *FEBS Lett.*, 2010, **584**, 1721–1727, DOI: 10.1016/j.febslet.2009.10.024.

41 C. Nitsche and G. Otting, *Curr. Opin. Struct. Biol.*, 2018, **48**, 16–22, DOI: 10.1016/j.sbi.2017.09.001.

42 J. E. Rouck, J. E. Krapf, J. Roy, H. C. Huff and A. Das, *FEBS Lett.*, 2017, **591**, 2057–2088, DOI: 10.1002/1873-3468.12706.

43 M. T. Marty, K. C. Wilcox, W. L. Klein and S. G. Sligar, *Anal. Bioanal. Chem.*, 2013, **405**, 4009–4016, DOI: 10.1007/s00216-013-6790-8.

44 T. Ravula, N. Z. Hardin and A. Ramamoorthy, *Chem. Phys. Lipids*, 2019, **219**, 45–49, DOI: 10.1016/j.chemphyslip.2019.01.010

45 C. Tribet, R. Audebert and J.-L. Popot, *Proc. Natl. Acad. Sci.*, 2002, DOI:10.1073/pnas.93.26.15047.

46 V. Schmidt and J. N. Sturgis, *Biochim. Biophys. Acta - Biomembr.*, 2018, **1860**, 777–783, DOI: 10.1016/J.BBAMEM.2017.12.012

47 J. M. Dörr, S. Scheidelaar, M. C. Koorengevel, J. J. Dominguez, M. Schäfer, C. A. van Walree and J. A. Killian, *Eur. Biophys. J.*, 2016, **45**, 3–21, DOI: 10.1007/s00249-015-1093-y.

48 J. M. Dörr, M. C. Koorengevel, M. Schäfer, A. V. Prokofyev, S. Scheidelaar, E. A. W. Van Der Cruijsen, T. R. Dafforn, M. Baldus and J. A. Killian, *Proc. Natl. Acad. Sci. U. S. A.*, 2014, **111**, 18607–18612, DOI: 10.1073/pnas.1416205112.

49 M. Jamshad, V. Grimard, I. Idini, T. J. Knowles, M. R. Dowle, N. Schofield, P. Sridhar, Y. Lin, R. Finka, M. Wheatley, O. R. T. Thomas, R. E. Palmer, M. Overduin, C. Govaerts, J. M. Ruysschaert, K. J. Edler and T. R. Dafforn, *Nano Res.*, 2015, **8**, 774–789, DOI: 10.1007/s12274-014-0560-6.

50 A. Stetsenko and A. Guskov, *Crystals*, 2017, **7**, 197, DOI: 10.3390/cryst7070197.

51 S. C. L. Hall, C. Tognoloni, J. Charlton, É. C. Bragginton, A. J. Rothnie, P. Sridhar, M. Wheatley, T. J. Knowles, T. Arnold, K. J. Edler and T. R. Dafforn, *Nanoscale*, 2018, **10**, 10609–10619, DOI: 10.1039/c8nr01322e.

52 M. He, Y. Zhou, H. Xiao and P. Lu, *New J. Chem.*, 2016, **40**, 1354–1364, DOI: 10.1039/c5nj02145f.

53 D. Lichtenberg, H. Ahyayauch, A. Alonso and F. M. Goñi, *Trends Biochem. Sci.*, 2013, **38**, 85–93, DOI: 10.1016/j.tibs.2012.11.005.

54 L. J. White, S. N. Tyuleva, B. Wilson, H. J. Shepherd, K. K. L. Ng, S. J. Holder, E. R. Clark and J. R. Hiscock, *Chem. - A Eur. J.*, 2018, **24**, 7761–7773, DOI: 10.1002/chem.201801280.

55 J. R. Hiscock, G. P. Bustone, B. Wilson, K. E. Belsey and L. R. Blackholly, *Soft Matter*, 2016, **12**, 4221–4228, DOI: 10.1039/C6SM00529B.

56 S. N. Tyuleva, N. Allen, L. J. White, A. Pépés, H. J. Shepherd, P. J. Saines, R. J. Ellaby, D. P. Mulvihill and J. R. Hiscock, *Chem. Commun.*, 2019, **55**, 95–98, DOI: 10.1039/C8CC08485H.

57 S. Omardien, J. W. Drijfhout, F. M. Vaz, M. Wenzel, L. W. Hamoen, S. A. J. Zaat and S. Brul, *Biochim. Biophys. Acta - Biomembr.*, 2018, **1860**, 2404–2415, DOI: 10.1016/j.bbamem.2018.06.004.

58 D. S. S. M. Uppu, S. Samaddar, C. Ghosh, K. Paramanandham, B. R. Shome and J. Haldar, *Biomaterials*, 2016, **74**, 131–143, DOI: 10.1016/j.biomaterials.2015.09.042.

59 SMA ® Imide Resins SMA ® 1000I, 2000I, 3000I and 4000I, https://pdfslide.net/documents/sma-imide-resins-sma-1000i-2000i-3000i-and-sma-1000i-2000i-3000i-and-4000i.html, (accessed 10 July 2019).

60 A. H. Kopf, M. C. Koorengevel, C. A. van Walree, T. R. Dafforn and J. A. Killian, *A simple and convenient method for the hydrolysis of styrene-maleic anhydride copolymers to styrene-maleic acid copolymers*, Elsevier, 2019, **218**, 85-90, DOI: 10.1016/j.chemphyslip.2018.11.011.

61 T. K. Lind, H. Wacklin, J. Schiller, M. Moulin, M. Haertlein, T. G. Pomorski and M. Cárdenas, *PLoS One*, 2015, **10**, DOI: 10.1371/journal.pone.0144671.

62 G. F. White, K. I. Racher, A. Lipski, F. R. Hallett and J. M. Wood, *Biochim. Biophys. Acta - Biomembr.*, 2000, **1468**, 175–186, DOI: 10.1016/S0005-2736(00)00255-8.

63 S. Bhattacharjee, *J. Control. Release*, 2016, **235**, 337–351, DOI: 10.1016/j.jconrel.2016.06.017.

64 M. Xue, L. Cheng, I. Faustino, W. Guo and S. J. Marrink, *Biophys. J.*, 2018, **115**, 494–502, DOI: 10.1016/j.ejmech.2018.08.061.

65 Malvern instruments Ltd, *Dynamic Light Scattering technical note*, https://www.malvernpanalytical.com/en/learn/knowledge-center/technical-notes/TN101104DynamicLightScatteringIntroduction (accessed 12 July 2019).

66 B. K. Nanjwade, A. B. Sarkar and T. Srichana, in *Characterization and Biology of Nanomaterials for Drug Delivery*, Elsevier, 2019, pp. 337–350, DOI: 10.1016/b978-0-12-814031-4.00012-x

67 G. W. Lu and P. Gao, in *Handbook of Non-Invasive Drug Delivery Systems*, Elsevier, 2010, pp. 59–94, DOI: 10.1016/b978-0-8155-2025-2.10003-4

68 O. Neudert, C. Mattea and S. Stapf, *Microporous Mesoporous Mater.*, 2018, **269**, 103–108, DOI: 10.1016/j.micromeso.2017.05.061.

69 I. R. Kleckner and M. P. Foster, *Biochim. Biophys. Acta - Proteins Proteomics*, 2011, **1814**, 942–968, DOI: 10.1016/j.bbapap.2010.10.012

70 L. R. Blackholly, H. J. Shepherd and J. R. Hiscock, *CrystEngComm*, 2016, DOI:10.1039/c6ce01493c.

6. Appendices

NMR spectra for compounds 1-3

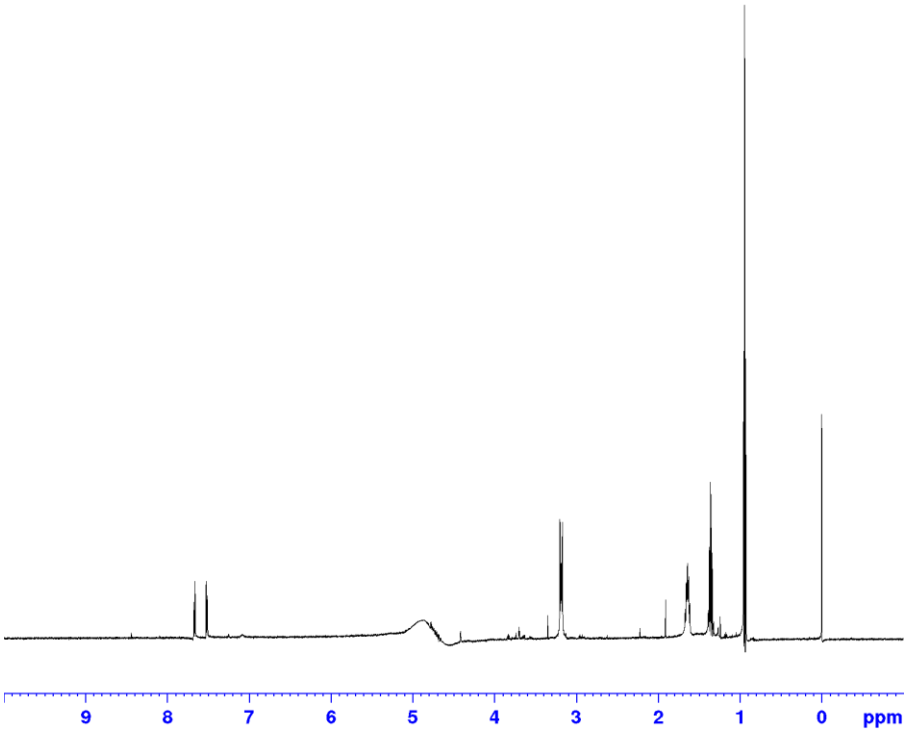

Figure 1**: NMR ^{1}H 1D of Compound **1

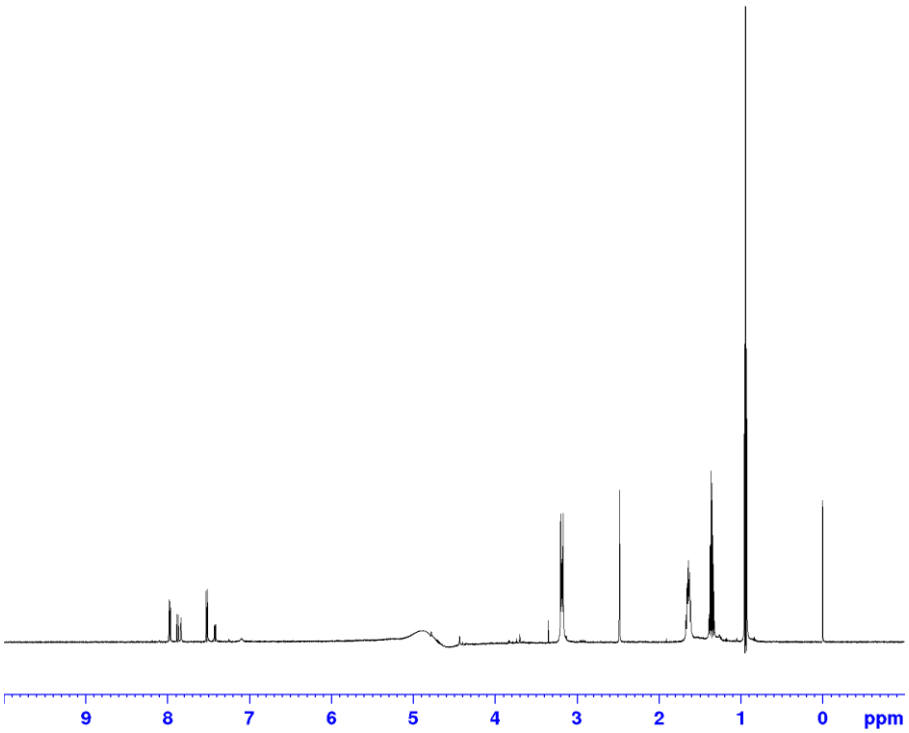

Figure 2**: NMR ^{1}H 1D of Compound **2

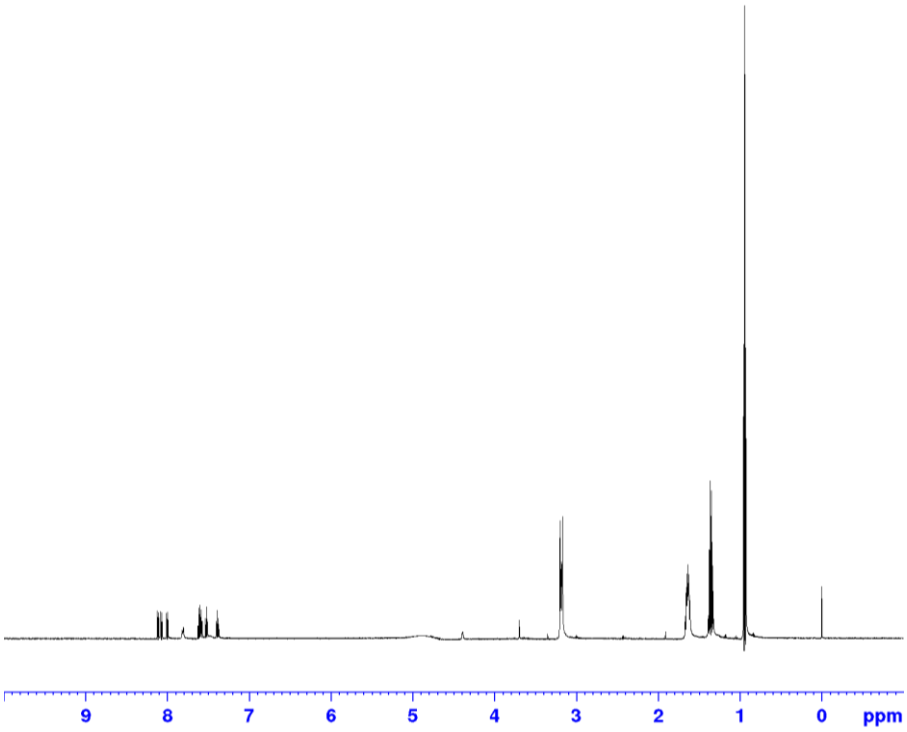

Figure 3**: NMR ^{1}H 1D of Compound **3

Table displaying concentrations used in NMR titrations

***Table 2:** Molar ratio of compounds **1-3** to SMALP*

SSA (µM)	E.coli SMALP (µM)	Molar ratio	SSA (µM)	DMPC SMALP (µM)	Molar ratio
100.0	0.0	0.000	100.0	0.0	0.000
99.7	0.2	0.002	99.5	0.2	0.002
99.3	0.4	0.004	99.0	0.4	0.004
99.0	0.6	0.006	98.6	0.6	0.006
98.7	0.8	0.008	98.1	0.8	0.008
98.3	1.0	0.010	97.6	1.0	0.010
97.5	1.5	0.015	96.5	1.5	0.016
96.8	2.0	0.021	95.4	2.0	0.021
95.2	3.0	0.032	93.2	3.0	0.032
93.7	4.0	0.043	91.1	4.0	0.044
93.4	6.0	0.064	90.7	6.0	0.066
93.1	8.0	0.086	90.3	8.0	0.089
92.8	10.0	0.108	89.9	10.0	0.111
92.1	15.0	0.163	89.0	15.0	0.169
91.4	20.0	0.219	88.0	20.0	0.227
90.7	25.0	0.276	87.1	25.0	0.287
87.4	50.0	0.572	82.7	50.0	0.605
84.3	75.0	0.890	78.8	75.0	0.952
81.4	100.0	1.229	75.2	100.0	1.330

NMR ^{1}H 1D Data Tables

Table 2: NMR ^{1}H 1D Data Table reporting each peak used to determine the change in intensity, and the corresponding molar ratio for *E.coli* [SMALPs}/[Compound **1**]

***E.coli* [SMALPs]/[Compound 1]**					
Peak Name	**Molar Ratio**	**Actual Intensity**	**ν(F1) [ppm]**	**Change in Intensity**	**Change in Intensity (%)**
1	0.000	244736.26	7.6651	0.00	100
2	0.002	241098.97	7.6654	-3637.29	99
3	0.004	243217.25	7.6654	-1519.01	99
4	0.006	242727.78	7.6652	-2008.48	99
5	0.008	234072.01	7.6652	-10664.25	96
6	0.010	196846.70	7.6649	-47889.56	80
7	0.015	217040.73	7.6652	-27695.53	89
8	0.021	211948.38	7.6652	-32787.88	87
9	0.032	204340.75	7.6650	-40395.51	83
10	0.043	229346.12	7.6654	-15390.14	94
11	0.064	214958.92	7.6654	-29777.34	88
12	0.086	214903.08	7.6656	-29833.18	88
13	0.108	214127.42	7.6654	-30608.84	87
14	0.163	208837.77	7.6648	-35898.49	85
15	0.219	223973.19	7.6649	-20763.07	92
16	0.276	195888.98	7.6653	-48847.28	80
17	0.572	209213.67	7.6650	-35522.59	85
18	0.890	202843.75	7.6648	-41892.51	83
19	1.229	201124.88	7.6645	-43611.38	82

Table 3: NMR ^{1}H 1D data table reporting each peak used to determine the change in intensity, and the corresponding molar ratio for DMPC [SMALPs}/[Compound **1**]

DMPC [SMALPs]/[Compound 1]					
Peak Name	**Molar Ratio**	**Actual Intensity**	**v(F1) [ppm]**	**Change in Intensity**	**Change in Intensity (%)**
1	0.000	237445.73	7.6664	0	100
2	0.002	254662.36	7.6654	17216.63	107
3	0.004	204817.79	7.6653	-32627.94	86
4	0.006	214667.22	7.6656	-22778.51	90
5	0.008	200555.42	7.6651	-36890.31	84
6	0.010	190162.27	7.6652	-47283.46	80
7	0.016	190693.14	7.6652	-46752.59	80
8	0.021	192061.3	7.6653	-45384.43	81
9	0.032	215845.3	7.6654	-21600.43	91
10	0.044	196390.48	7.6652	-41055.25	83
11	0.066	227421.84	7.6655	-10023.89	96
12	0.089	196359.63	7.6653	-41086.1	83
13	0.111	183757.97	7.6653	-53687.76	77
14	0.169	183014.91	7.6653	-54430.82	77
15	0.227	196913.95	7.6652	-40531.78	83
16	0.287	202091.28	7.6647	-35354.45	85
17	0.605	200134.72	7.6644	-37311.01	84
18	0.952	207774.38	7.6634	-29671.35	88
19	1.330	196581.38	7.663	-40864.35	83

***Table 4**: NMR ^{1}H 1D data table reporting each peak used to determine the change in intensity, and the corresponding molar ratio for E.coli [SMALPs}/[Compound **2**]*

E.coli **[SMALPs]/[Compound 2]**					
Peak Name	**Molar Ratio**	**Actual Intensity**	**ν(F1) [ppm]**	**Change in Intensity**	**Change in Intensity (%)**
1	0.000	251245.08	7.9684	0.00	100
2	0.002	234486.59	7.9686	-16758.49	93
3	0.004	171990.09	7.9682	-79254.99	68
4	0.006	117466.96	7.9682	-133778.12	47
5	0.008	195921.41	7.9672	-55323.67	78
6	0.010	155575.69	7.9639	-95669.39	62
7	0.015	189914.87	7.9685	-61330.21	76
8	0.021	138743.94	7.9684	-112501.14	55
9	0.032	152925.31	7.9703	-98319.77	61
10	0.043	135405.82	7.9714	-115839.26	54
11	0.064	107220.88	7.9697	-144024.20	43
12	0.086	97050.81	7.9688	-154194.27	39
13	0.108	82492.14	7.9669	-168752.94	33
14	0.163	74545.23	7.9666	-176699.85	30
15	0.219	60342.98	7.9669	-190902.10	24
16	0.276	53912.08	7.9652	-197333.00	21
17	0.572	39910.31	7.9655	-211334.77	16
18	0.890	14594.62	7.9621	-236650.46	6
19	1.229	17832.38	7.9586	-233412.70	7

Table 5: NMR ^{1}H 1D data table reporting each peak used to determine the change in intensity, and the corresponding molar ratio for DMPC [SMALPs}/[Compound **2**]

DMPC [SMALPs]/[Compound 2]					
Peak Name	**Molar Ratio**	**Actual Intensity**	**ν(F1) [ppm]**	**Change in Intensity**	**Change in Intensity (%)**
1	0.000	193787.45	7.9727	0	100
2	0.002	194069.8	7.9729	282.35	100
3	0.004	143133.77	7.9729	-50653.68	74
4	0.006	151515.98	7.9709	-42271.47	78
5	0.008	151192.83	7.9716	-42594.62	78
6	0.010	129608.33	7.9733	-64179.12	67
7	0.016	118949.76	7.9697	-74837.69	61
8	0.021	109761.05	7.9694	-84026.4	57
9	0.032	117818.23	7.9693	-75969.22	61
10	0.044	93345.38	7.9709	-100442.07	48
11	0.066	90259.34	7.9675	-103528.11	47
12	0.089	93874.86	7.965	-99912.59	48
13	0.111	102988.57	7.9616	-90798.88	53
14	0.169	87758.78	7.9617	-106028.67	45
15	0.227	76413.78	7.9599	-117373.67	39
16	0.287	70673.84	7.9591	-123113.61	36
17	0.605	64816.16	7.9593	-128971.29	33
18	0.952	59487.62	7.9592	-134299.83	31
19	1.330	62444	7.9606	-131343.45	32

Table 6: NMR ^{1}H 1D data table reporting each peak used to determine the change in intensity, and the corresponding molar ratio for *E.coli* [SMALPs}/[Compound **3**]

***E.coli* [SMALPs]/[Compound 3]**					
Peak Name	**Molar Ratio**	**Actual Intensity**	**ν(F1) [ppm]**	**Change in Intensity**	**Change in Intensity (%)**
1	0.000	224544.22	8.1372	0.00	100
2	0.002	199405.38	8.1370	-25138.84	89
3	0.004	143059.06	8.1372	-81485.16	64
4	0.006	138289.80	8.1367	-86254.42	62
5	0.008	139316.47	8.1373	-85227.75	62
6	0.010	142956.26	8.1371	-81587.96	64
7	0.015	117296.56	8.1376	-107247.66	52
8	0.021	112258.34	8.1370	-112285.88	50
9	0.032	139628.79	8.1378	-84915.43	62
10	0.043	132393.02	8.1375	-92151.20	59
11	0.064	135936.83	8.1383	-88607.39	61
12	0.086	136942.29	8.1387	-87601.93	61
13	0.108	124746.29	8.1386	-99797.93	56
14	0.163	131747.38	8.1392	-92796.84	59
15	0.219	95788.56	8.1389	-128755.66	43
16	0.276	119442.76	8.1396	-105101.46	53
17	0.572	103788.25	8.1404	-120755.97	46
18	0.890	112393.28	8.1421	-112150.94	50
19	1.229	100548.41	8.1422	-123995.81	45

Table 7: NMR ^{1}H 1D data table reporting each peak used to determine the change in intensity, and the corresponding molar ratio for DMPC [SMALPs}/[Compound **3**]

DMPC [SMALPs]/[Compound 3]					
Peak Name	**Molar Ratio**	**Actual Intensity**	**ν(F1) [ppm]**	**Change in Intensity**	**Change in Intensity (%)**
1	0.000	215118.47	8.1369	0	100
2	0.002	190006.09	8.1371	-25112.38	88
3	0.004	135703.04	8.136	-79415.43	63
4	0.006	152144.93	8.1362	-62973.54	71
5	0.008	149221.8	8.1371	-65896.67	69
6	0.010	214057.75	8.1375	-1060.72	100
7	0.016	161672.23	8.1366	-53446.24	75
8	0.021	130108.61	8.1379	-85009.86	60
9	0.032	190518.12	8.1382	-24600.35	89
10	0.044	185307.83	8.1382	-29810.64	86
11	0.066	180279.04	8.1388	-34839.43	84
12	0.089	183204.31	8.1392	-31914.16	85
13	0.111	150270.62	8.1396	-64847.85	70
14	0.169	188873.94	8.1409	-26244.53	88
15	0.227	190708.86	8.141	-24409.61	89
16	0.287	174138.92	8.1416	-40979.55	81
17	0.605	152823.69	8.1431	-62294.78	71
18	0.952	156779.75	8.1451	-58338.72	73
19	1.330	150607.62	8.1474	-64510.85	70

NMR CPMG ^{1}H Data Tables

Table 8: CPMG ^{1}H Data table reporting each peak used to determine the change in intensity, and the corresponding molar ratio for *E.coli* [SMALPs}/[Compound **1**]

***E.coli* [SMALPs]/[Compound 1]**					
Peak Name	**Molar Ratio**	**Actual Intensity**	**ν(F1) [ppm]**	**Change in Intensity**	**Change in Intensity (%)**
1	0.000	49125.72	7.6698	0.00	100
2	0.002	46798.57	7.6662	-2327.15	95
3	0.004	47838.05	7.6656	-1287.67	97
4	0.006	48164.82	7.6656	-960.90	98
5	0.008	48358.41	7.6655	-767.31	98
6	0.010	45111.85	7.6654	-4013.87	92
7	0.015	45607.79	7.6658	-3517.93	93
8	0.021	44917.25	7.6656	-4208.47	91
9	0.032	45663.75	7.6656	-3461.97	93
10	0.043	45829.32	7.6653	-3296.40	93
11	0.064	43346.40	7.6661	-5779.32	88
12	0.086	43040.00	7.6638	-6085.72	88
13	0.108	42319.02	7.6672	-6806.70	86
14	0.163	41307.73	7.6655	-7817.99	84
15	0.219	40019.81	7.6657	-9105.91	81
16	0.276	37797.88	7.6658	-11327.84	77
17	0.572	36573.70	7.6647	-12552.02	74
18	0.890	35506.10	7.6654	-13619.62	72
19	1.229	31994.81	7.6653	-17130.91	65

Table 9: CPMG ^{1}H Data table reporting each peak used to determine the change in intensity and the corresponding molar ratio for DMPC [SMALPs}/[Compound **1**]

DMPC [SMALPs]/[Compound 1]					
Peak Name	**Molar Ratio**	**Actual Intensity**	**v(F1) [ppm]**	**Change in Intensity**	**Change in Intensity (%)**
1	0.000	44679.96	7.6797	0	100
2	0.002	43407.42	7.6802	-1272.54	97
3	0.004	41681.4	7.6795	-2998.56	93
4	0.006	43376.17	7.6797	-1303.79	97
5	0.008	41991.72	7.6797	-2688.24	94
6	0.010	38147.11	7.6794	-6532.85	85
7	0.016	42243.82	7.6799	-2436.14	95
8	0.021	40493.9	7.6796	-4186.06	91
9	0.032	42922.45	7.68	-1757.51	96
10	0.044	38932.61	7.6801	-5747.35	87
11	0.066	42860.55	7.6801	-1819.41	96
12	0.089	40607.48	7.6796	-4072.48	91
13	0.111	38849	7.6799	-5830.96	87
14	0.169	38803.26	7.6795	-5876.7	87
15	0.227	38601.51	7.6794	-6078.45	86
16	0.287	36727.07	7.6792	-7952.89	82
17	0.605	36451.41	7.6788	-8228.55	82
18	0.952	33913.05	7.6781	-10766.91	76
19	1.330	32313.92	7.6776	-12366.04	72

Table 10: CPMG ^{1}H Data table reporting each peak used to determine the change in intensity and the corresponding molar ratio for *E.coli* [SMALPs}/[Compound **2**]

***E.coli* [SMALPs]/[Compound 2]**					
Peak Name	**Molar Ratio**	**Actual Intensity**	**v(F1) [ppm]**	**Change in Intensity**	**Change in Intensity (%)**
1	0.000	31482.46	7.9691	0.00	100
2	0.002	28355.16	7.9694	-3127.30	90
3	0.004	15317.93	7.9683	-16164.53	49
4	0.006	14594.74	7.9684	-16887.72	46
5	0.008	16301.66	7.9678	-15180.80	52
6	0.010	14453.92	7.9648	-17028.54	46
7	0.015	14444.40	7.9687	-17038.06	46
8	0.021	10556.44	7.9686	-20926.02	34
9	0.032	6580.84	7.9718	-24901.62	21

Table 11: CPMG ^{1}H Data table reporting each peak used to determine the change in intensity and the corresponding molar ratio for DMPC [SMALPs}/[Compound **2**]

DMPC [SMALPs]/[Compound 2]					
Peak Name	**Molar Ratio**	**Actual Intensity**	**v(F1) [ppm]**	**Change in Intensity**	**Change in Intensity (%)**
1	0.000	34764.07	7.973	0	100
2	0.002	33394.59	7.9867	-1369.48	96
3	0.004	23565.93	7.9731	-11198.14	68
4	0.006	18286.94	7.9711	-16477.13	53
5	0.008	13483.14	7.9725	-21280.93	39
6	0.010	9625.65	7.974	-25138.42	28

Table 12: CPMG 1H Data table reporting each peak used to determine the change in intensity and the corresponding molar ratio for *E.coli* [SMALPs}/[Compound **3**]

***E.coli* [SMALPs]/[Compound 3]**					
Peak Name	**Molar Ratio**	**Actual Intensity**	**ν(F1) [ppm]**	**Change in Intensity**	**Change in Intensity (%)**
1	0.000	35693	8.1372	0.00	100
2	0.002	40984.88	8.1387	5291.88	115
3	0.004	28976.04	8.1373	-6716.96	81
4	0.006	29516.59	8.1374	-6176.41	83
5	0.008	27402.12	8.1374	-8290.88	77
6	0.010	24874.99	8.1375	-10818.01	70
7	0.015	24335.59	8.1322	-11357.41	68
8	0.021	21833.54	8.1382	-13859.46	61
9	0.032	25611.99	8.1373	-10081.01	72
10	0.043	26520.96	8.1385	-9172.04	74
11	0.064	3753.56	8.444	-31939.44	11
12	0.086	22191.14	8.1386	-13501.86	62
13	0.108	21143.46	8.1381	-14549.54	59
14	0.163	19381.01	8.139	-16311.99	54
15	0.219	17861.09	8.1396	-17831.91	50
16	0.276	17190.13	8.1392	-18502.87	48
17	0.572	13046.48	8.1411	-22646.52	37
18	0.890	7271.56	8.1408	-28421.44	20
19	1.229	3533.98	8.4443	-32159.02	10

This set of data had an erroneous point, peak 11 which was excluded from the data set, as it doesn't follow the trend.

Table 13: CPMG ^{1}H Data table reporting each peak used to determine the change in intensity and the corresponding molar ratio for DMPC [SMALPs}/[Compound **3**]

DMPC [SMALPs]/[Compound 3]					
Peak Name	**Molar Ratio**	**Actual Intensity**	**v(F1) [ppm]**	**Change in Intensity**	**Change in Intensity (%)**
1	0.000	34707.62	8.1369	0	100
2	0.002	32767.27	8.1371	-1940.35	94
3	0.004	27242.74	8.1374	-7464.88	78
4	0.006	28483.56	8.1372	-6224.06	82
5	0.008	29194.3	8.1375	-5513.32	84
6	0.010	33670.99	8.1372	-1036.63	97
7	0.016	30653.31	8.1376	-4054.31	88
8	0.021	25814.88	8.1383	-8892.74	74
9	0.032	31206.2	8.138	-3501.42	90
10	0.044	29961.19	8.1381	-4746.43	86
11	0.066	29244.2	8.1391	-5463.42	84
12	0.089	29969.46	8.1391	-4738.16	86
13	0.111	25664.57	8.1394	-9043.05	74
14	0.169	26602.21	8.1403	-8105.41	77
15	0.227	25146.69	8.1409	-9560.93	72
16	0.287	24468.79	8.1416	-10238.83	70
17	0.605	19456.6	8.1431	-15251.02	56
18	0.952	17005.18	8.1457	-17702.44	49
19	1.330	13387.22	8.1478	-21320.4	39